Studies of Penetrant Permeation in Polymer Materials by Molecular Simulation(Dissertation_全文)

AUTHOR(S):

Tamai, Yoshinori

(2)

Studies of
Penetrant Permeation in Polymer Materials
by Molecular Simulation

YOSHINORI TAMAI

1995

Contents

Chapter 1

General Introduction

1.1 Background

1.1.1 Molecular Simulation Techniques

The molecular simulation techniques, such as molecular dynamics (MD) and Monte Carlo (MC) simulations, are very powerful tools in understanding molecular assemblies with a resolution of atomistic details. By using these methods, a variety of macroscopic thermodynamic quantities may be calculated directly from the simulations which incorporate atomistic microstructures. This gives these methods an advantage over other computational chemistry methods such as molecular orbital (MO) and molecular mechanics (MM), which cannot treat macroscopic quantities, or semi-empirical methods such as quantitative structure–property relationship (QSPR), which cannot reflect atomistic details.

The molecular simulation techniques have been applied mainly for the Lennard-Jones fluids and small organic liquids.[1] Dynamic properties are estimated by MD simulation. The chemical potentials can be calculated by the test particle insertion (Widom) method.[2] The phase equilibria can be simulated directly by the Gibbs ensemble method.[3] Various physico-chemical properties of liquids have been elucidated by the methods. Nowadays, the methods are applied extensively to polymer systems. In early works, MD and MM methods are applied to biological polymers: proteins and nucleic acids. Then the methods are also applied to synthetic polymer systems. For example, the structure of amorphous polymers has been investigated by MD simulation and MM calculation.[4–12] The diffusion processes of nonpolar small penetrants in

amorphous polymer matrices have been examined by MD simulation.[13–21] The Widom and the Gibbs ensemble methods have been improved to be applicable to polymer/penetrant systems.

1.1.2 Separation Membranes

It is interesting and important in both scientific and technological fields to understand the mechanism of permeation of small penetrants in polymer materials. Promoted by surging concern about environmental problems, material separation techniques by the use of functional membranes have been employed in various fields, such as energy-saving separation processes and elimination of contaminants. For more general and practical use of these membranes, it is urgent for us to elucidate the mechanism and to improve the performance of separation.

Pervaporation[22] is a method of separating the mixture of liquids by membranes. The components of the liquid mixture are supplied on the feed side of the membrane and diffuse to the permeate side of the membrane, where pressure is diminished, leaving the membrane as vapor. Poly(dimethylsiloxane) (PDMS) is used for the membrane which separates ethanol from the aqueous solution by pervaporation. The separation process is explained by the sorption–diffusion model.

The sorption–diffusion model describes permeation of small molecules in a nonporous polymer membrane. Sorption of small molecules on the surface of a membrane causes a concentration gradient in the membrane, and the gradient causes diffusion of the molecules. The permeation rate P of small penetrants depends on solubility and diffusivity and is expressed by

$$P = DS \tag{1.1}$$

where D is the diffusion coefficient and S is the solubility of penetrants. When considering the separation of the mixture of two components, the separation

factor of the component 1 is expressed by

$$\alpha_1 = \frac{P_1}{P_2} \tag{1.2}$$

where P_1 and P_2 are permeation rates of components 1 and 2, respectively, which are calculated from the diffusion coefficients and the solubilities of components 1 and 2. It is useful for the design of functional separation membranes to predict the solubility and diffusion coefficient using a molecular simulation technique. Diffusion coefficients of small penetrant molecules in an amorphous polymer matrix can be calculated by MD simulation. Solubilities can be calculated by the test particle insertion method.

The characteristic of the penetrant permeation is governed by interactions between polymers and penetrants and their complicated cooperative motions, which should be investigated from a microscopic view point by using the molecular simulation techniques. The hydrogel, which is made of hydrophilic polymer and water, is one of the suitable models to investigate interaction between polymers and small molecules. Properties of hydrophilic polymer membranes depend seriously on the degree of the moisture sorption. The phenomena such as the moisture permeation into membranes, the sorption of water in hydrogels, the wetting in interfaces, etc., have a close relation to permeation characteristic of penetrants into functional membranes. Investigation on the mixture of polymers and water is also helpful to understanding mechanism of the plasticization, which varies capabilities of separation.

The hydrogels are used for various functional materials. The hydrogels which have the lower critical solution temperature (LCST) swell at low temperature and are transformed into condensed state by the volume phase transition at high temperature. These hydrogels are supposed to be used for intelligent materials which respond to temperature. The interaction between water and polymers seems to play an essential role in this transition. Water molecules in the hydrogels have different properties from those of pure water since those are constrained by polymers. It is very interesting to study some characteristics

of water molecules coexisting with hydrophilic polymers, because it has some relation to the folding of proteins and various biological phenomena.

Water has anomalous physico-chemical properties due to three-dimensional hydrogen-bond networks. These days, the physico-chemical properties of water are elucidated by many molecular simulation studies using MD or MC method.[23] It has been well recognized that hydrogen-bonds play a significant role in those anomalous static and dynamic properties of water. Various attempts are also made to explore the effects of hydrogen-bond networks on mobility and various properties of water and aqueous solutions.[24] An application of those methods to hydrogel models are most welcome to account for a role of the gels on water molecules.

1.2 Outline

A main purpose of the present study is understanding the mechanism of permeation of small molecules (penetrants) in various polymer materials (membranes). The interplay between polymers and penetrants plays an essential role in the permeation of penetrants in membranes. Thus, it is important in both scientific and technological fields to investigate this interplay from a microscopic view point. That may be successfully carried out by using the molecular simulation techniques mentioned above.

In Part I of this thesis, the permeation of penetrants in hydrophobic polymer membranes is simulated. MD simulations have been performed for methane, water, and ethanol in PDMS and polyethylene (PE). In Chapter 2, the structures of amorphous PDMS and PE together with liquid water and ethanol are generated. The distribution and structure of the free volume are analyzed. In Chapter 3, the diffusion processes of the penetrants in the polymers and the liquids are investigated. In Chapter 4, the solubilities are evaluated by the test particle insertion method. The permeation rates are calculated from the diffusion coefficients and the solubilities.

In Part II of this thesis, the permeation of penetrants (water) in hydrophilic polymer membranes (hydrogels) is simulated. MD simulations have been performed for the hydrogel models of poly(vinyl alcohol) (PVA), poly(vinyl methylether) (PVME), and poly(N-isopropyl acrylamide) (PNiPAM). Investigations are made on the interaction between water and polymers, which has close relation to the penetrant permeation phenomena. Simulations are performed for the hydrogel models with various water contents under several temperature conditions. In Chapter 5, analyses are made for the distribution and structure of hydrogen-bond networks. In Chapter 6, some dynamical properties are also evaluated and analyzed. These properties are expected to depend significantly on the surrounding polymer matrices.

1.3 Simulation Program

In order to perform the simulations described above, we coded a general program package PAMPS (Molecular Simulation Programs for Analysis of Mixtures of Polymers and Small Molecules), which can perform molecular simulation for the mixtures of polymers and/or small molecules. The programs are mainly coded by FORTRAN 77 (approximately 40 000 lines) and are executable on CRAY Y-MP (UNICOS), NEC SX-3 (SUPER-UX), HP-9000 700 series (HP-UX), Sun SPARK (SUN-OS), IBM POWER station (AIX), and may be executable on other UNIX machines. Both scalar and vectorized versions are available.

The program can perform molecular simulations based on MD and MC methods, including the test particle insertion method. The force fields AMBER, OPLS, and CHARMm are incorporated (see Appendix A). The long-range Coulomb interactions are calculated by the Ewald sum. For saving computer time, the switching function is also available to calculate the Coulomb potentials. The calculation method of the long-range forces is described in Appendix B. Amorphous polymer structures are generated by the modified self-avoiding random walk (see Appendix C). The structures are energy minimized (quenched) by the steepest descent method. MD simulations are performed

under constant NVE conditions, and also under constant NPT (NVT, NPH) conditions using the Nosé–Andersen method. Bond lengths and angles can be constrained by the SHAKE algorithm, or subjected to harmonic potentials. The equations of motion are solved using the Verlet algorithm.[26] The Verlet neighbor list[27] is used for saving computer time. Techniques for perform MD simulation by the NPT ensemble combined with the SHAKE algorithm are described in Appendix D. The excess chemical potential is calculated by the Widom[2] and the Shing-Gubbins[28, 29] methods. Efficiency of particle insertion is raised by the excluded volume map sampling (EVMS).[30] Insertion trials of a chain molecule are also available by the continuum configurational bias (CCB) method.[31] The analyses described in Appendix E can be made.

Using this program package, all calculations were performed on NEC SX-3 and CRAY Y-MP2E supercomputers and HP-9000 700-series workstations. Generous amounts of computer time were provided by the Supercomputer Laboratory, Institute for Chemical Research, Kyoto University. Computer time was provided also by Computer Center, Institute for Molecular Science.

Part I

Permeation into Hydrophobic Membranes

Chapter 2

Structure of Amorphous Polymers

2.1 Introduction

Theodorou and Suter[4, 5] made the first attempt to investigate microscopic structures of amorphous polymers by molecular simulation. They investigated the detailed molecular structure of a vinyl polymer glass: atactic polypropylene (a-PP) at −40 °C. An initial structure is generated by using a modified Markov process, based on the rotational isomeric state (RIS) theory[32] and incorporating long-range interactions. This structure is then "relaxed" by potential energy minimization. They analyzed pair distribution functions and bond direction correlation functions. The elastic constants of the amorphous glassy polymer are also predicted by small-strain deformation of the structures.

Following them, several groups have investigated structures and properties of amorphous polymers. Mansfield and Theodorou[6, 7] studied surface of glassy a-PP by MM and MD simulations. Hutnik et al.[8, 9, 10] simulated polycarbonate of 4,4'-isopropylidenediphenol. Fan and Hsu[11] simulated aromatic polysulfone system and examined some mechanical and thermal properties.

The diffusion coefficient is dependent on the free volume and its size distribution. Shah et al.[33] calculated the available free volume distribution for penetrants in polymers using a Monte Carlo integration method where they measured the diameter of the largest hard sphere which could be located at a randomly chosen point in the polymers. Arizzi et al.[34] divided the structures of a-PP and PC into tetrahedral interstices using Delaunay tessellation and calculated the fraction of the interstices which are accessible for small penetrants. They also analyzed the connectivity of the interstices. Greenfield

and Theodorou[35] reported a similar analysis for a-PP. Misra and Mattice[36] divided the unit cell of polybutadiene into small cubes and calculated the accessible volume fraction for small penetrants and also analyzed the cluster of the accessible cubes.

In this chapter, amorphous structures of PDMS and PE are generated. The free volume of the polymers are analyzed and compared with those of liquids.

2.2 Model and Simulation Details

2.2.1 Model and Potential Functions

PDMS and PE samples are modeled as shown in Figure 2.1. There are no cross-links and branches. Simulations are carried out for the systems containing five polymer chains in cubic periodic boxes. The degree of polymerization x of each chain is 30 for PDMS and 60 for PE. The simulations for pure liquid water and ethanol are also carried out for the systems containing 216 and 128 molecules, respectively, in cubic periodic boxes. The experimental densities at 300 K are used, i.e., 0.95, 0.855, 0.9965, and 0.7851 g/cm^3 for PDMS,[15] PE,[20, 38] water,[37] and ethanol (25 °C),[79] respectively. PE is a semicrystalline polymer, and the density is varied with crystallinity. Since diffusion of small penetrants takes place only in an amorphous region, the density of the amorphous fraction is used for PE in the present simulation. The density of PDMS varies with the degree of polymerization and cross-link. The same density as the study of Sok et al. is used to compare the results.

The AMBER/OPLS is used for PE, and the OPLS for ethanol. The GROMOS force field is used for PDMS, and the SPC/E for water. All CH_4, CH_3–, and –CH_2– groups are treated as united atoms. Potential functions used in the simulations are summarized in Appendix A.

Because the force constant of the bond angle Si–O–Si of PDMS is small and the equilibrium bond angle is large (144°), the probability that the bond

PDMS PE

Figure 2.1. Structures of polydimethylsiloxane (PDMS) and polyethylene (PE).

angle goes across $\theta = 180°$ cannot be neglected at high temperature. Since the derivative of the potential functions with respect to the atom positions is not continuous at $\theta = 180°$, an energy jump occurs when the bond angle goes across $\theta = 180°$. To circumvent this energy jump, we add the auxiliary term

$$\begin{aligned} V(\theta) &= V_0(\theta) & \theta \le \theta_s \\ &= V_0(\theta) + k_s(\theta - \theta_s)^2 & \theta > \theta_s \end{aligned} \tag{2.1}$$

where $k_s = 1.0\times\ 10^4$ kJ/mol and $\theta_s = 165°$. $V_0(\theta)$ is the original potential function expressed as eq A.2. This term prevents the energy jump and does not change the bond angle distribution at 300 K.

2.2.2 Simulation of Amorphous PDMS

Using the modified self-avoiding random walk, five polymer chains are packed into a unit cell under the periodic boundary condition at density of 0.5 g/cm^3. Detailed description of the method is available in Appendix C. In this stage, nonbonded potentials are modeled by the soft core type repulsive potentials. The 1,4-interaction energy of a main chain is described by the rotational isomeric states (RIS) model.[32] In this study, we use the RIS parameters of both Bahar, Zuniga, Dodge, and Mattice (BZDM)[40, 41] and Flory, Crescenzi, and Mark (FCM).[39] The results from both parameters are compared. After the packing of chains is completed, excess overlaps of atoms are eliminated by 1000 steps of the steepest-descent energy minimization using the potential without the Coulombic term and by subsequent 1000 steps of energy mini-

mization with the full potential. Then, MD simulation is performed for a full potential system. The volume of the unit cell is decreased by a small amount at every time step. After reaching the experimental density, the usual MD simulation is performed, where the box length is 27.24 Å.

The equations of motion are solved using the Verlet algorithm[26] with a time step of 5 fs under the constant NVE condition. The bond lengths are constrained to the equilibrium bond lengths by the SHAKE algorithm. The Lennard-Jones terms of the potential are cut off at 10 Å. Long-range Coulombic interactions are handled by the Ewald sum method (see Appendix B). The Verlet neighbor list[27] is used with automatic updating of the list. Temperature scalings are imposed every 5 ps to prevent creep of temperature in long time simulation. The system is stable during the whole simulation step, and the average value of the scaling factors of velocities is nearly unity. MD simulation is performed for 625 ps at 300 K, for 150 ps at 1000 K to relax the structure, and then for 625 ps at 300 K. The trajectory of the last 500 ps is used for analysis of the amorphous structure.

2.2.3 Simulation of Amorphous PE

The amorphous structure of PE is generated by the same method as given above. The description of the 1,4-interaction energy of a main chain is slightly different. The soft core type repulsive potentials are used instead of $V_{\mathrm{RIS}}[\mathrm{state}(\phi)]$ in eq C.6. After 1000 steps of energy minimization, MD simulation is performed with gradual compression of the unit cell until the experimental density is achieved. The final box length is 25.46 Å. MD simulations are performed for 250 ps at 300 K, for 150 ps at 1000 K, and then for 1100 ps at 300 K. The trajectory of the last 500 ps is used for analysis of the amorphous structure.

2.2.4 Simulation of Pure Liquids

For the simulations of pure liquid water and ethanol, 216 and 128 molecules, respectively, are confined in periodic boxes at the experimental densities by applying the first step of the modified self-avoiding random walk. The box lengths are 18.65 and 23.19 Å for water and ethanol, respectively. After 2000 steps of energy minimization, MD simulations are performed under the constant NVT condition. The NVT method by Nosé is utilized combined with the SHAKE algorithm by using the iterative method of Ferrario and Ryckaert, as described in Appendix D. The inertial parameter for the extra variable, W_s in Appendix D, is 7000 a.m.u.Å^2, which gives a frequency of approximately 1 ps for the fluctuation of the extra variable. This time scale is the same as that in the study of Palmer and Garrett,[42] where several dynamical properties were discussed. A time step of 0.5 fs is used. The Lennard-Jones terms are cut off at 9 and 10 Å for water and ethanol, respectively. The Ewald sum method and the Verlet neighbor list are used. After 150 ps of MD runs to equilibrate the systems, a trajectory of 50 ps is sampled for water and of 100 ps for ethanol. Sampling times and time steps for the simulations are summarized in Table 2.1.

Table 2.1. Sampling Times and Time Steps for MD Simulations

sample	sampling(ps)	time step(fs)
PDMS	500	5
PE	500	5
water	50	0.5
ethanol	100	0.5

2.2.5 Insertion Probabilities

We calculate the insertion probability $P(R)$, which is defined as the probability that a hard-sphere solute of radius R could be located at an arbitrary point in the matrix without overlap with the van der Waals volume of any matrix molecule.[43] $P(R)$ is related to the free volume fraction and its distribution. We also calculate its derivative

$$P_{\mathrm{m}}(R) = -\frac{\mathrm{d}P(R)}{\mathrm{d}R} \tag{2.2}$$

which is the probability that the largest hard sphere solute that could be inserted at an arbitrary point would have a radius within $\mathrm{d}R$ of R.

Each atom of the matrix is modeled as a hard sphere of radius $\sigma/2$, where σ means the Lennard-Jones size parameter. The histogram is constructed with regard to the minimum distances from each grid point of $100 \times 100 \times 100$ on the unit cell to the surfaces of the hard sphere of the matrix. This histogram leads to $P_{\mathrm{m}}(R)$ by normalization, and $P_{\mathrm{m}}(R)$ is integrated to

$$P(R) = \int_R^\infty P_{\mathrm{m}}(R')\mathrm{d}R' \tag{2.3}$$

Time dependence and time averages of $P(R)$ and $P_{\mathrm{m}}(R)$ are calculated over the 250–1000 coordinates of trajectories.

2.2.6 Cluster Analysis of the Free Volume

Arizzi et al.,[34] Greenfield and Theodorou,[35] and Misra and Mattice[36] made a cluster analysis of the free volume in polymers. We use a method similar to that of Misra and Mattice. The unit cell is divided into $100 \times 100 \times 100$ grid points on which a probe atom is settled. We select the grid points (denoted by t) which satisfy the equation for all host atoms (denoted by i)

$$|\mathbf{r}_t - \mathbf{r}_i| \geq \frac{\sigma_t + \sigma_i}{2} \tag{2.4}$$

where $\mathbf{r}_t$ is the position of the test atom on the grid point, $\mathbf{r}_i$ is the position of the ith host atom, and σ_t and σ_i are the Lennard-Jones size parameters of the

test atom t and the ith host atom. With this procedure, we can determine the grid points on which the probe atom can be settled without severe overlaps with the host atoms. The cluster analysis is performed for the accessible cubes whose centers are on the accessible grid points and whose edge lengths are equal to $^1/_{100}$th of the unit cell length. Assuming that the two accessible cubes which share a surface belong to the same cluster, the clusters of accessible cubes are constructed.

The cluster shape is also analyzed. Using the coordinates of the grid points which belong to the same cluster, we calculate a radius of gyration matrix $\mathbf{S}$. The elements of $\mathbf{S}$ are

$$\begin{aligned} S_{xx} &= \sum_{i=1}^{N_{\mathrm{g}}} x_i x_i \\ S_{xy} &= \sum_{i=1}^{N_{\mathrm{g}}} x_i y_i \\ &\vdots \end{aligned} \tag{2.5}$$

where N_{g} is the number of grid points in the cluster and (x_i, y_i, z_i) are the coordinates of the grid point relative to the center of the cluster. The eigenvalues of $\mathbf{S}$ are determined such that

$$X^2 \geq Y^2 \geq Z^2 \tag{2.6}$$

The squared radius of gyration ${s_j}^2$ and asphericity $(b/s^2)_j$ of cluster j are calculated from the eigenvalues:

$${s_j}^2 = X^2 + Y^2 + Z^2 \tag{2.7}$$

$$(b/s^2)_j = \frac{X^2 - \frac{1}{2}(Y^2 + Z^2)}{X^2 + Y^2 + Z^2} \tag{2.8}$$

For clusters which contain only one accessible grid point, we define ${s_j}^2 = 0$ and $(b/s^2)_j = 0$. For each system, these values are calculated from 100

configurations, averaged as

$$\langle A \rangle = \frac{\sum_{i=1}^{N_c} V_i A_i}{\sum_{i=1}^{N_c} V_i} \tag{2.9}$$

where A_i is an arbitrary quantity and V_i is the volume of the ith cluster. N_c is the total number of clusters which are contained in all the coordinates used for the calculation.

2.3 Results and Discussion

2.3.1 Structure of Amorphous PDMS

We generated two different initial structures using different RIS parameters: the BZDM and the FCM. These initial structures give different profiles of the insertion probability $P(R)$ and the dihedral angle distribution. The initial structure from the FCM has a broader distribution of $P(R)$ and a higher trans population than that from the BZDM. Since the distribution of $P(R)$ has much influence on the diffusivity and solubility of a small penetrant in a polymer, we checked whether the influence of the initial structures on the distributions of $P(R)$ would remain or not.

During the first 625 ps of MD simulation at 300 K, the influence on the insertion probability and the dihedral angle distribution remained significant. We performed 150 ps of MD runs at 1000 K to relax the structure. Figure 2.2 shows the time dependence of the dihedral angle distribution of Si–O–Si–O during 150 ps of MD runs at 1000 K. Only the time dependence of the initial 50 ps is shown. Figure 2.2a shows the time dependence of the dihedral angle distribution with the BZDM parameters and Figure 2.2b those with the FCM. The dihedral angle distributions decay to the equilibrium values during 20 ps of MD runs at 1000 K. Both structures have the same trans population (~0.4) which are averaged over the last 100 ps of trajectories.

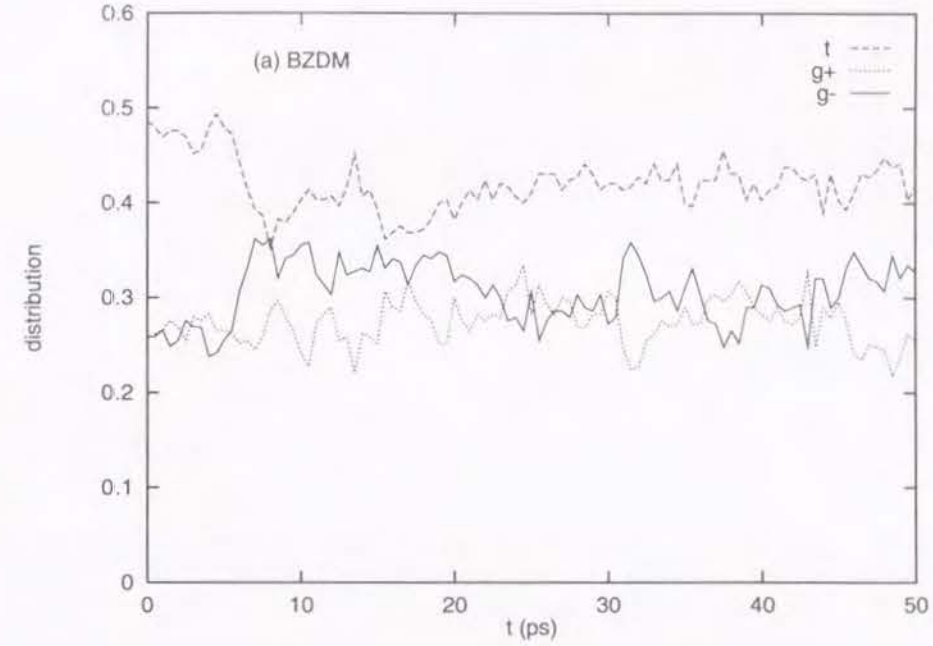

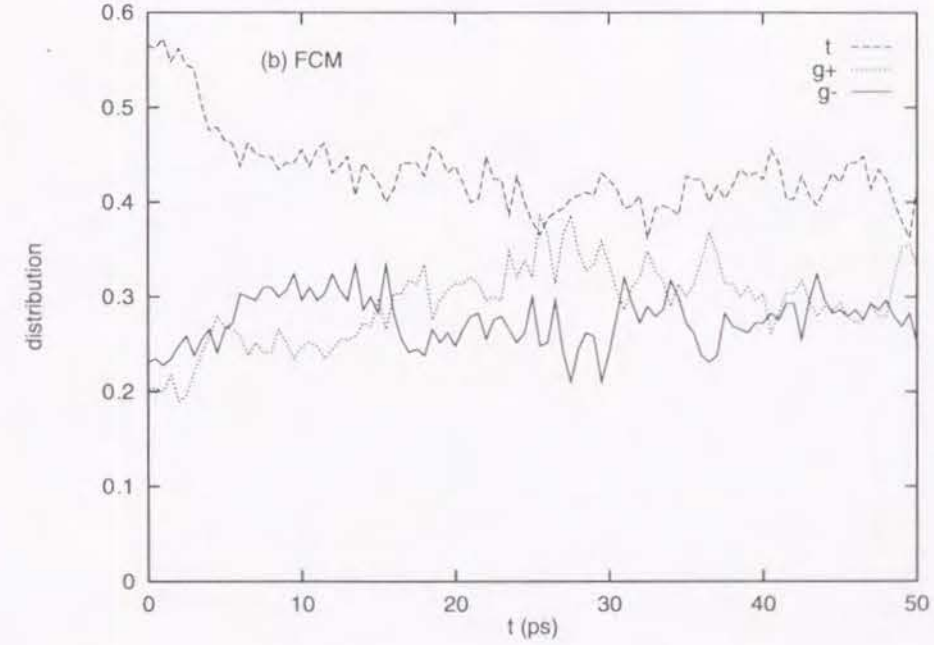

Figure 2.2. Time dependence of the dihedral angle distribution of Si–O–Si–O of PDMS at 1000 K. The initial structures were generated using (a) the BZDM RIS parameters and (b) the FCM.

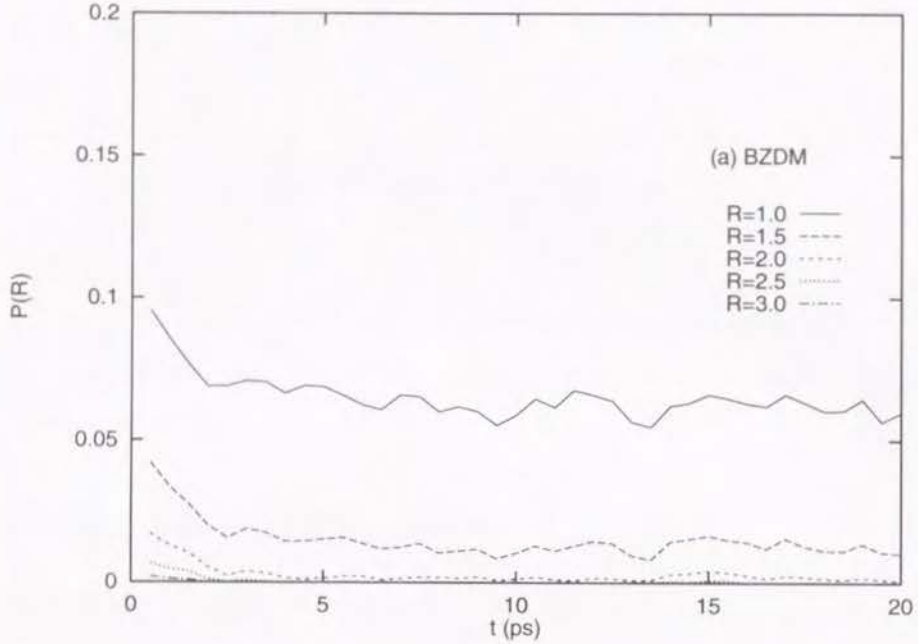

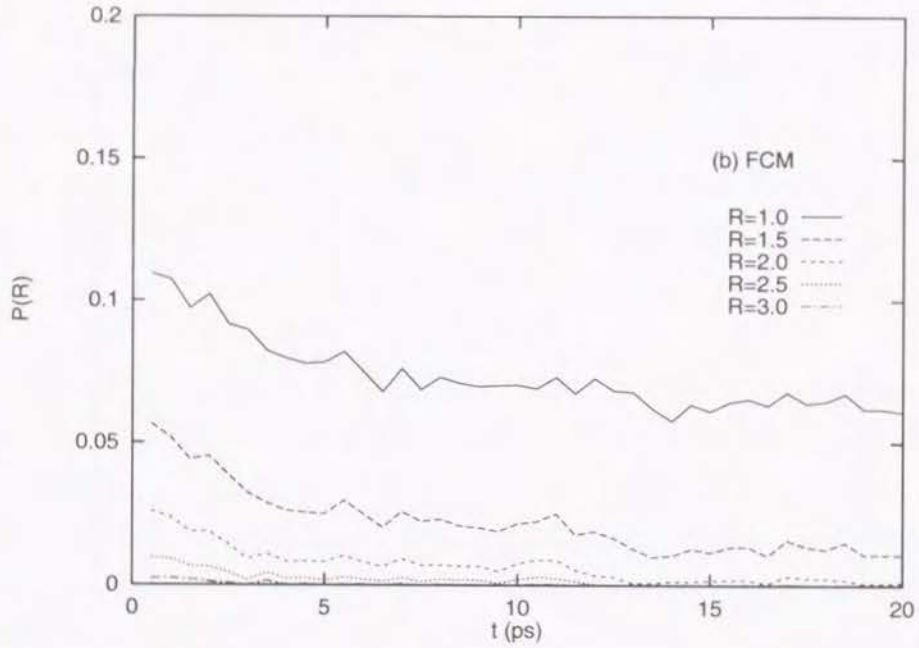

Figure 2.3. Time dependence of insertion probability $P(R)$ of PDMS for five values of hard-sphere radius R at 1000 K. The initial structures were generated using (a) the BZDM RIS parameters and (b) the FCM.

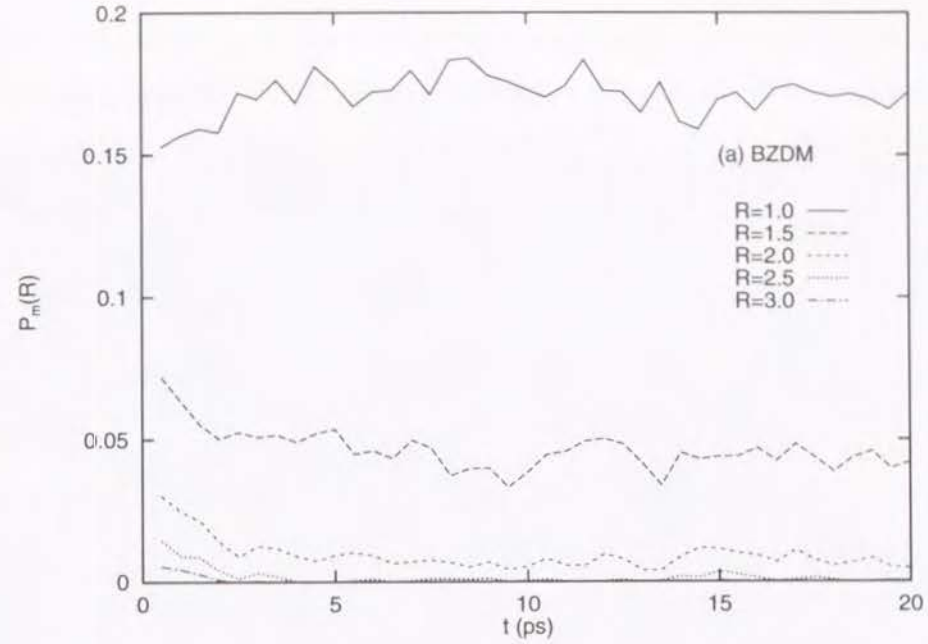

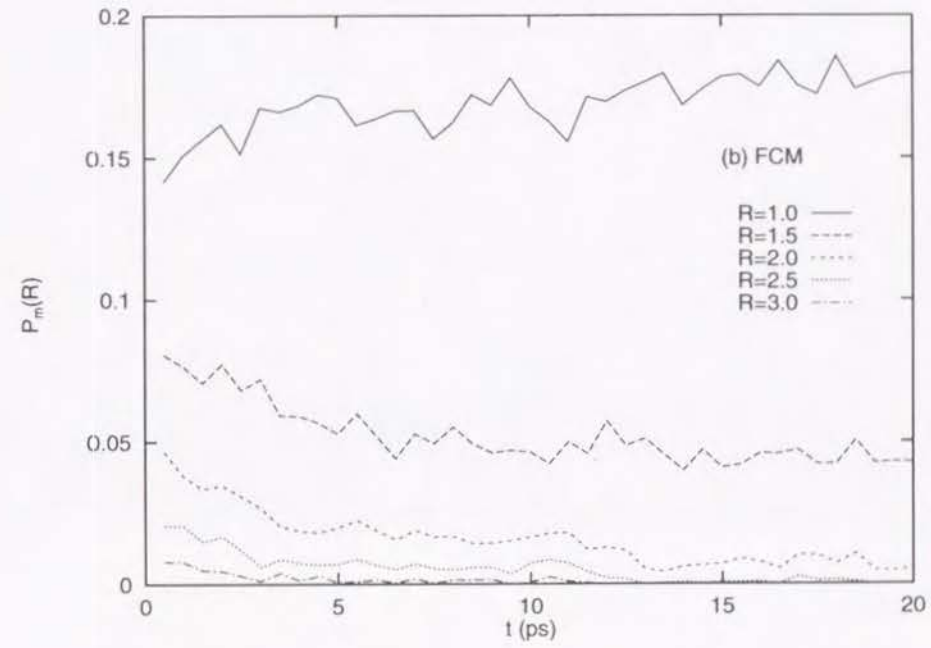

Figure 2.4. Time dependence of derivative insertion probability $P_{\mathrm{m}}(R)$ of PDMS for five values of hard sphere radius R at 1000 K. The initial structures were generated using (a) the BZDM RIS parameters and (b) the FCM.

Figure 2.3 shows the time dependence of the insertion probability $P(R)$ for some values of R during 150 ps of MD runs at 1000 K. Figure 2.3a shows that of the BZDM, and Figure 2.3b that of the FCM. Although the total free volumes, $P(0)$, of the BZDM and that of the FCM are not different from each other and do not vary with time, the distributions of $P(R)$ are different from each other and vary with time. The free volume distributions, $P(R)$, converged almost completely to the equilibrium values during 20 ps of MD runs at 1000 K. The insertion probabilities averaged over the last 100 ps of trajectories show similar distributions irrespective of the initial structures. Figure 2.4 shows a plot of $P_{\mathrm{m}}(R)$. $P_{\mathrm{m}}(R)$ of large R decrease with time, and $P_m(R)$ of small R increase with time. This means that large cavities break into small cavities with relaxation of chains. These values come close to equilibrium values during 20 ps.

Because the influence of initial structures on the free volume distribution could be eliminated by the high-temperature MD runs, we use only the structure from the BZDM for the following simulation. We performed 625 ps of MD simulation at 300 K and used the last 500 ps of trajectory for analysis of the amorphous polymer structure. A final structure of amorphous PDMS is shown in Figure 2.5. Only one of five polymer chains in the unit cell is colored by the CPK model. The obtained polymer structure has no long-range order as is evident from the radial distribution function. The dihedral angle distribution was (0.438, 0.275, 0.287) for (t, g^+, g^-), which agreed with the value (0.412, 0.289, 0.299) calculated from the MD trajectory of the oligomer of eight units in vacuum by Bahar et al.[40] The mean-square radius of gyration was 116 Å^2.

2.3.2 Structure of Amorphous PE

After the first 250 ps of MD simulation at 300 K, the trans population of the main chains is approximately 0.7. We examined time dependence of the dihedral angle distribution and the insertion probability at 1000 K. The trans population of dihedral angles relaxed to equilibrium value (0.56) during

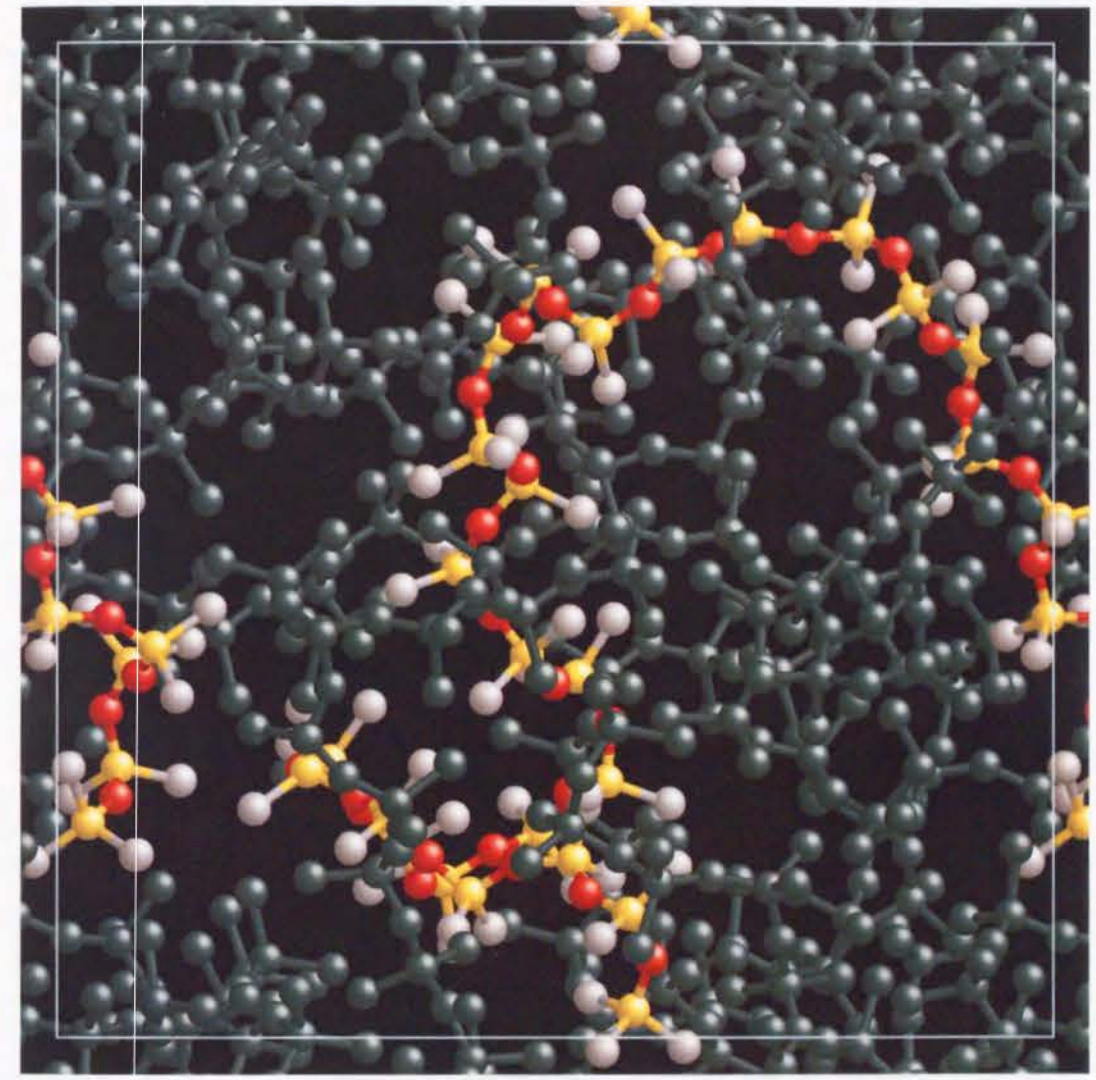

Figure 2.5. Snap shot of an amorphous structure of PDMS. Only one of five polymer chains in the unit cell is colored by the CPK model: (yellow) silicon, (red) oxygen, (light gray) united atom carbon. The unit cell is drawn by white lines.

3 ps, which is shorter than the time scale of relaxation of the dihedral angle distribution of PDMS. On the contrary, the insertion probability did not vary with time. For PDMS, the initial structure had much influence on $P(R)$. For PE, however, the initial structure had only a little influence on $P(R)$. PDMS has large side groups, $-CH_3$, attached to the main chain, which prevent the main chains from contact. Because bond angles are kept constant in the packing of the chains by the modified self-avoiding random walk, the side group effect is more severe, which leads to the broad distribution of the insertion probability. The rearrangement of the main chains at 1000 K relaxes the free volume distribution. In the case of PE, the rearrangement of the main chains has only a little effect on the insertion probability because PE has no side group.

After 150 ps of the MD run at 1000 K, 1100 ps of MD simulation was performed. The trans population of the main chains relaxed to the equilibrium value (0.71) during 500 ps and fluctuated around this value during the last 600 ps of the MD runs. The dihedral angle distribution calculated from the last 500 ps of trajectory was (0.714, 0.143, 0.143) for (t, g^+, g^-). The mean-square radius of gyration was 334 Å^2.

2.3.3 Insertion Probabilities

Figure 2.6 shows $P(R)$ and $P_m(R)$ for PDMS, PE, liquid water, and liquid ethanol at 300 K. The free volume fractions, $P(0)$, of PDMS, PE, water, and ethanol were 0.4817, 0.3721, 0.4665, and 0.4425, respectively. The free volume fraction of PDMS is large. PDMS shows a broader distribution of $P(R)$ and $P_m(R)$ compared with the others. The reason for this is that PDMS has large methyl groups attached to a main chain, which keep neighbor chains apart. Table 2.2 shows the accessible volume fraction of the penetrant in the polymers and liquids, which is equal to $P(R)$ for the penetrant of radius R. The van der Waals radii, $\sigma/2$, were used for the radii of water and methane, and the kinetic radius,[44] 2.604 Å, was used for the radius of ethanol. The penetrants

Table 2.2. Accessible Volume Fraction of Small Penetrants in Polymers and Liquids at 300 K

penetrant	radius(Å)	$f_v \times 10^4$ [a]			
		in PDMS	in PE	in water	in ethanol
water	1.583	174.89	2.74	1.21	5.84
methane	1.865	77.85	0.22	0.09	0.81
ethanol	2.604	4.16	0.00	0.00	0.00

[a]The accessible volume fraction, which is equal to the insertion probability $P(R)$ for a penetrant of radius R.

have a larger accessible volume fraction in PDMS than in PE. The broader free volume distribution will lead to a larger diffusion coefficient and larger solubility of a small penetrant in PDMS.

In spite of restriction by a polymer matrix, experimental diffusion coefficients of methane and water in PDMS are the same order ($\sim 10^{-5}$ cm^2/s) as those of liquid water and ordinary organic liquids. One of the reasons for this is that PDMS has a large free volume fraction and a broad free volume distribution.

2.3.4 Cluster Analysis of the Free Volume

Figure 2.6 shows the broader distribution of the insertion probability $P(R)$ of hard sphere atoms of radius R in PDMS. Therefore, a large solubility is expected even for a relatively large molecule in PDMS.

To obtain further information about the free volume, we performed a cluster analysis of the free volume using a water molecule (radius 1.5828 Å) as a probe. Parts a and b of Figure 2.7 show the accessible volume clusters in the instantaneous configuration of PDMS and of PE, respectively. The figures show the projection of the unit cells onto the x–y plane. The cell lengths are

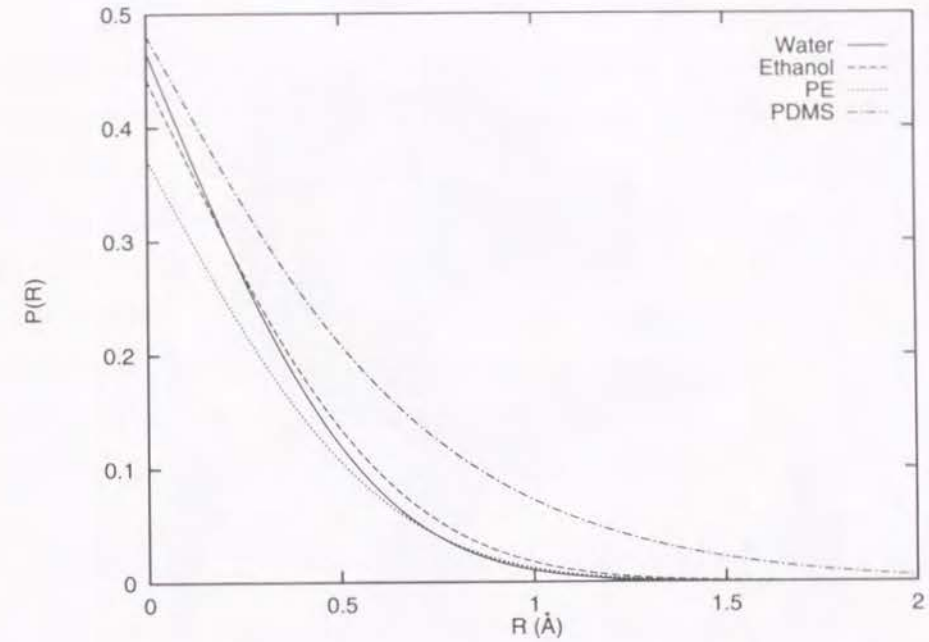

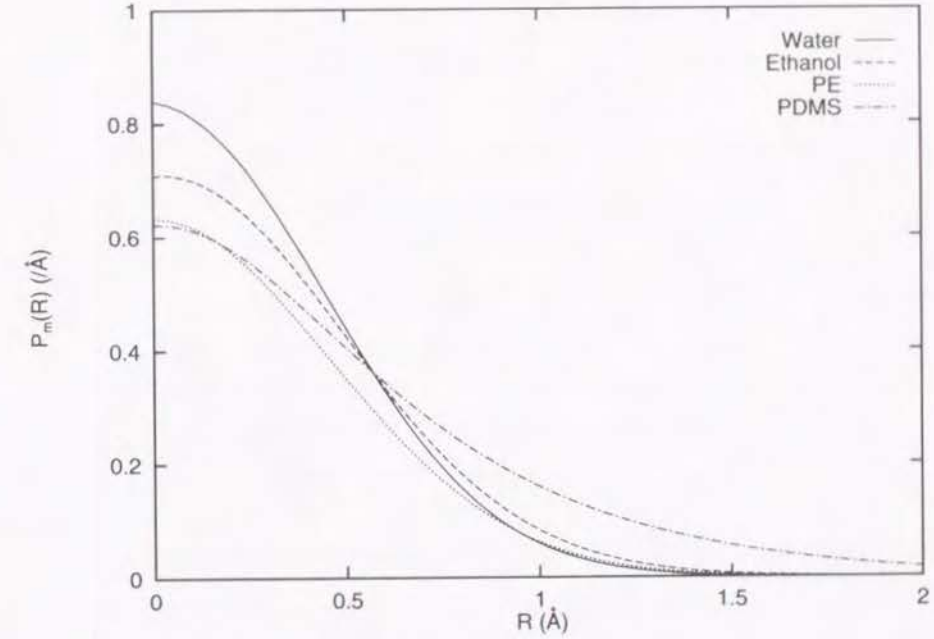

Figure 2.6. Insertion probabilities $P(R)$ of PDMS, PE, water, and ethanol at 300 K, and the derivatives $P_m(R) = -dP(R)/dR$.

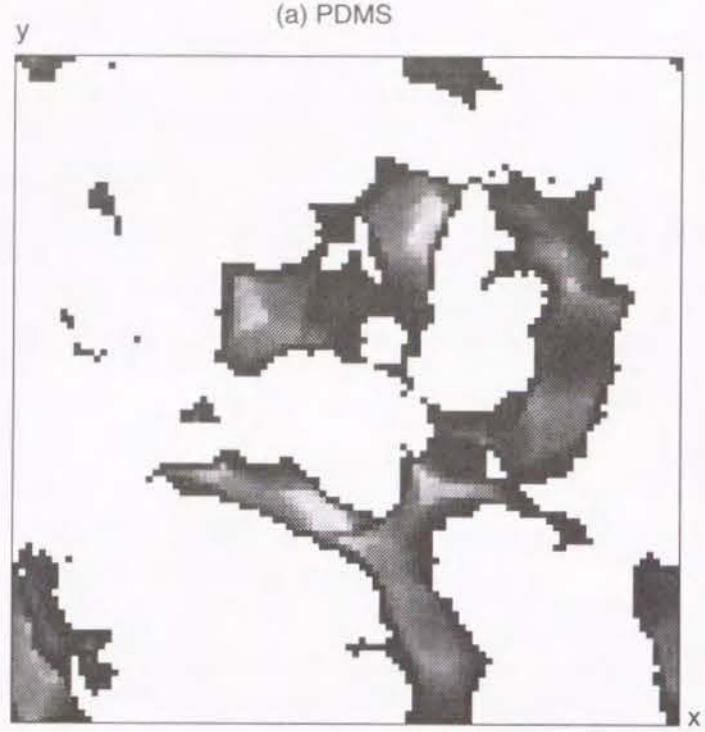

Figure 2.7. The x–y projections of accessible clusters (a) in PDMS and (b) in PE, using a water molecule as a probe.

27.24 and 25.46 Å for PDMS and PE, respectively. The white parts in the background indicate the regions in which the overlaps between water and the polymers are severe. The accessible clusters are expressed by gray-scale. The brighter the grid point in the cluster is, the more accessible cubes exist in the depth direction. Therefore, the central region of the large cluster is white. The free volume clusters in PDMS are larger than those in PE. Note that the figures are projections of the clusters onto the planes. The cluster looks larger than a real cluster. The channel through which a small penetrant permeates is narrow. The free volume fractions with a water molecule as a probe were approximately 1.8% for PDMS and 0.05% for PE.

Table 2.3. Cluster Analysis of Accessible Cubes for Water

matrix	$f_v \times 10^4$	$\langle V_c \rangle$ (Å^3)	$\langle s^2 \rangle^{1/2}$ (Å)	$\langle b/s^2 \rangle$
Accessible Clusters in Polymers				
PDMS	176.7	166.67	6.15	0.567
PE	5.0	6.54	1.32	0.542
Accessible Clusters in Liquids				
0 wt %[a]	0.7	0.65	0.58	0.552
50 wt %[a]	7.0	11.48	1.97	0.570
100 wt %[a]	10.4	8.18	1.37	0.520

[a] Concentration of the aqueous ethanol solution.

Table 2.3 lists the free volume fraction f_v, the average volume of the clusters $\langle V_c \rangle$, the root mean-square radius of gyration $\langle s^2 \rangle^{1/2}$, and the asphericity $\langle b/s^2 \rangle$. The value f_v is an arithmetic mean over 100 coordinates, and the other values are the averages weighted by the volume of the clusters. The value of f_v is larger in PDMS than in the other systems. The values of $\langle V_c \rangle$ and $\langle s^2 \rangle^{1/2}$ are also large in PDMS. The radius of gyration of clusters in PDMS, 6.15 Å,

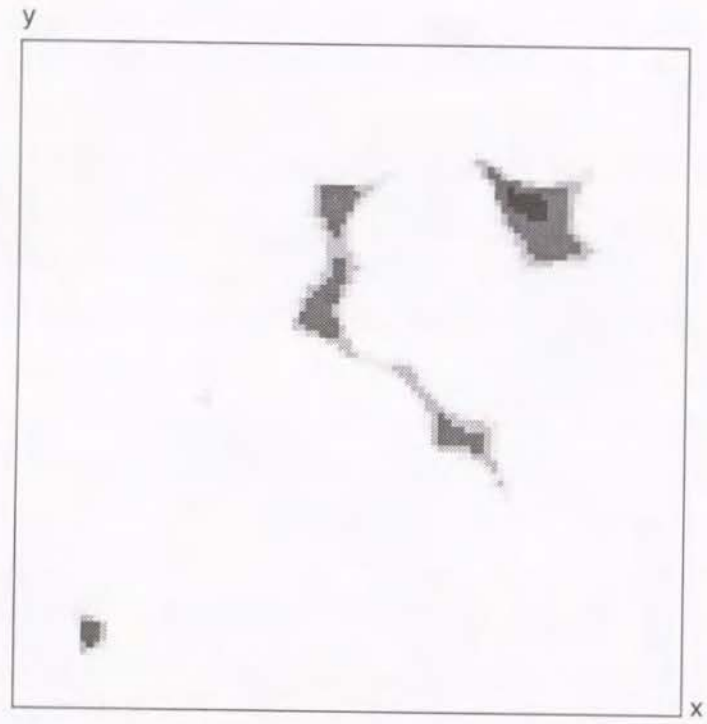

Figure 2.8. Energy map for a methane molecule in PDMS on an arbitrarily chosen plane parallel to the x–y plane. The energies are divided into five regions between $U =$ −18, −8, 0, and 10 kJ/mol; the lower energy region is painted darker.

is sufficiently large compared with the kinetic radius of ethanol, 2.604 Å.[44] This does not mean that a cavity with a radius of 6 Å exists in the polymer matrix but means that cavities which are connected by channels are spread over an area with a radius of 6 Å. This structure of the free volume in PDMS leads to the large diffusion coefficients of small penetrants in PDMS, and the fact that larger molecules are soluble in PDMS. For the asphericity, no marked difference is found among the systems.

2.3.5 Energy Map of Penetrants in Polymers

A three-dimensional energy map was generated for the penetrant molecules in the polymers. Considering 100 × 100 × 100 grid points in the unit cell of PDMS, all the grid points were classified by the interaction energy U

between a methane molecule on the grid point and the host matrix. Figure 2.8 shows the energy map for a methane molecule in PDMS on an arbitrarily chosen plane parallel to x–y. The energies are divided into five classes separated at $U = -18$, -8, 0, and 10 kJ/mol. The darkest region in the figure shows the most stable region: $U < -18$ kJ/mol. The white region shows the unstable region: $U > 10$ kJ/mol. The middle energy regions are painted by gray-scale. The low-energy regions look like islands surrounded by higher energy regions. The dark regions of the figure correspond to the channels through which a methane molecule can permeate with low energy.

2.4 Conclusion

The structures of amorphous PDMS and PE were obtained by MD simulations. The initial structures were obtained by modified self-avoiding random walk. The free volume of the amorphous polymers are calculated and the cluster analysis of the free volume were performed. In PDMS, the free volume is large and its distribution is broad; the free volume clusters are connected by channels. A small penetrant in PDMS is expected to have large diffusion coefficient and large solubility, even for a large penetrant molecule such as ethanol.

Chapter 3

Diffusion of Small Penetrants in Polymers

3.1 Introduction

The diffusion coefficients of small penetrant molecules in amorphous polymer matrices have been calculated from MD simulations.[13–21] All these calculations were performed for nonpolar small molecules: helium, methane, oxygen, etc. In early works the calculated diffusion coefficients of small penetrants in polyethylene (PE), polyisobutylene (PIB), and atactic polypropylene (a-PP) were 10–100 times higher than the experimental values. Müller-Plathe et al.[17] attributed those deviations to the united atom approximation. They calculated the diffusion coefficients of oxygen in PIB using the all-atom force field with explicit hydrogen atoms and obtained the value which is close to the experimental value. Pant and Boyd[20, 21] calculated the diffusion coefficients of methane in PE and PIB using the anisotropic united atom (AUA) potential, in which off-center Lennard-Jones potentials were used for the nonbonded interactions, and they obtained values close to the experimental ones. On the other hand, Sok et al.[15] obtained a value of the diffusion coefficient of methane in PDMS close to the experimental one, in spite of the united atom approximation. The discrepancy between experimental and calculated diffusion coefficients by use of the united atom approximation depends largely on the size of the penetrants, as discussed by Müller-Plathe; the larger the penetrant is, the smaller the discrepancy is.

For a simple liquid, the diffusion coefficient can be calculated by relatively short time runs of MD simulation. For a small molecule in a polymer matrix, however, very long time runs of MD simulation are required. Müller-Plathe

et al.[18] performed several nanoseconds of MD simulation for He and O_2 in PIB. The diffusion of He and O_2 through the polymer matrix exhibits anomalous (non-Einstein) behavior for time scales of at least 0.1 and 6 ns for He and O_2, respectively. Gusev et al.[45, 46] calculated the diffusion coefficients of light gases in rubbery PIB and glassy Bisphenol A polycarbonate (PC) by the new transition-state theory which takes atomistic microstructures into consideration using the information on the mobility of the host matrix, which was calculated from short-time-scale MD runs. Because the mobility of the polymer chains is very low in the glassy state, the diffusion coefficients of Ar, O_2, and N_2 in PC are very small; it takes a very long time scale ($\sim$1 μs) to exhibit the normal diffusion behavior.

In this chapter, MD simulations are performed for very long periods: 2–5 ns. We calculate the diffusion coefficients of methane, water, and ethanol in PDMS by the MD simulation in order to examine a permeative mechanism of small molecules in the PDMS membrane. These systems are quite different from the previous works, because we consider larger penetrants and penetrants which can form hydrogen bonds. For comparison, we calculate diffusion coefficients of methane, water, and ethanol in PE and those of pure liquid water and ethanol.

3.2 Model and Simulation Details

3.2.1 Model and Potential Functions

PDMS and PE samples are modeled as described in Chapter 2. All calculations are performed on CRAY Y-MP2E supercomputer using the molecular simulation program PAMPS which we coded. The AMBER/OPLS force field is used except for PDMS and water. The GROMOS force field is used for PDMS, and the SPC/E for water. All CH_4, CH_3– and –CH_2– groups are treated as united atoms. A detailed description of the potential functions is given in Appendix A.

3.2.2 MD Simulation

Using the modified self-avoiding random walk (see Appendix C), one or five penetrant molecules are inserted into the polymer structures which were obtained in Chapter 2. The Lennard-Jones potentials are used for nonbonded interaction at this stage. For the system which contains five penetrant molecules, the initial positions of five penetrants are determined so that an arbitrarily chosen penetrant is separated from any other penetrants by at least 10 Å to disperse the penetrant molecules in the unit cell. MD simulations are performed with writing out coordinates of atoms on the files. The sampling time is 500 ps for short time runs and 2000 or 5000 ps for long time runs. A time step of 1 fs is used for short time runs. For long time runs, a time step of 5 fs is used for the methane/polymer system, and a time step of 2 fs is used for the water/polymer and ethanol/polymer systems. The time step of 2 fs for water is rather long compared with the simulation of liquid water and ethanol. Since we are interested mainly in translational motion and long time behavior in the present simulation, we use these time steps. The MD methods are the same as those used in Chapter 2. The simulated systems and conditions are summarized in Table 3.1.

3.2.3 Diffusion Coefficient

Diffusion coefficients are calculated from the least-squares fits of the mean-square displacements of the centers of mass of the penetrant molecules averaged over all possible time origins as

$$D = \lim_{t\to\infty} \frac{1}{6t} \langle [\mathbf{R}(t) - \mathbf{R}(0)]^2 \rangle \tag{3.1}$$

where $\mathbf{R}(t)$ is a position of the center of mass of a penetrant at time t and $\langle\ \rangle$ means an ensemble average.

To study the effect of aggregation of penetrants, similar simulations are performed for the systems which contain five penetrant molecules of water and

Table 3.1. Sampling Times and Time Steps for MD Simulations

matrix	penetrant	sampling(ps)	time step(fs)
Penetrants in PDMS (Long Time Runs)			
PDMS	methane×5	5000	5
PDMS	water×1	2000	2
PDMS	water×5	2000	2
PDMS	ethanol×1	2000	2
PDMS	ethanol×5	2000	2
Penetrants in PDMS (Short Time Runs)			
PDMS	water×5	500	1
PDMS	ethanol×5	500	1
Penetrants in PE			
PE	methane×5	5000	5
PE	water×1	2000	2
PE	ethanol×1	2000	2

ethanol. For pure liquid water and ethanol, diffusion coefficients are calculated from the MSD using the trajectories obtained in Chapter 2.

3.3 Results and Discussion

3.3.1 Displacement of Small Penetrants

Figure 3.1a shows displacements of the penetrant molecules from the initial positions in PDMS and Figure 3.1b those in PE. The displacements were smoothed over 5 ps in order to reduce the noise level. The displacement of methane is a representative one of the five molecules. The mobility of water

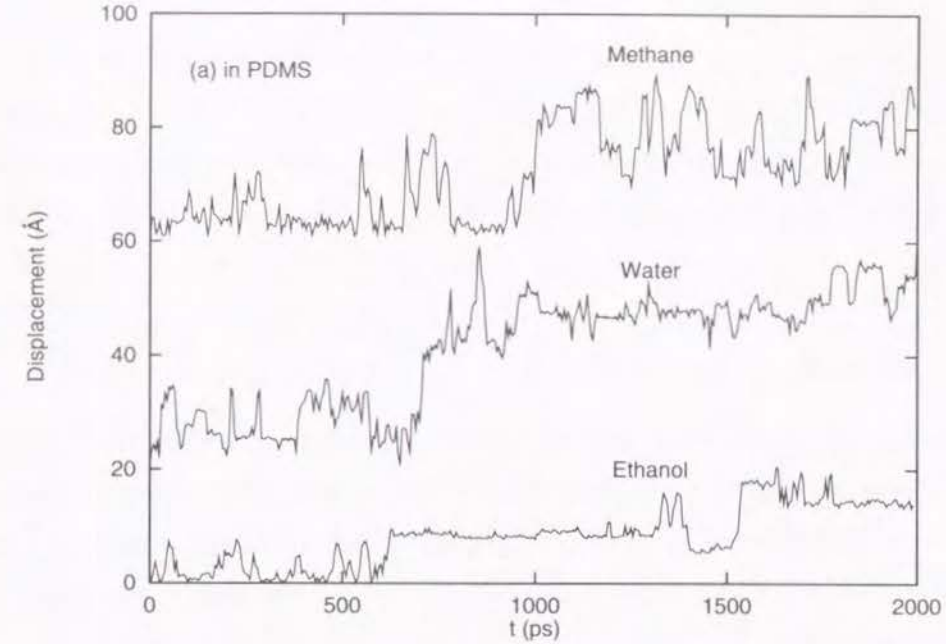

Figure 3.1. Time dependence of displacements from the initial positions of methane, water, and ethanol (a) in PDMS and (b) in PE at 300 K. The noise in the original data is smoothed by displaying 5 ps rolling averages. The data for methane and water are offset by 60 and 20 Å, respectively.

is on the same order as methane, and the mobility of ethanol is lower. Both successive small jumps and large jumps are observed. The small penetrants in PDMS have longer jump distances and make more frequent jumps than those in PE. Large vibrational motions of longer time scales are also notable in PDMS.

3.3.2 Diffusion of Methane

We calculated the mean-square displacements from the 5000 ps of trajectories of five methane molecules in PDMS and in PE. The concentrations of methane in PDMS and PE are 0.69 and 0.94 g of solvent/100 g of polymer, respectively. Neither appreciable aggregation nor phase separation was observed in both systems.

Figure 3.2 shows the mean-square displacements as a doubly logarithmic plot. The results of pure liquid water and ethanol are also plotted. In short time regions, the mean-square displacements follow a power law of t^2. In long time regions, the mean-square displacements are linear in time, where Einstein's equation (eq 3.1) is applicable. At intermediate regions, anomalous diffusion is observed and the mean-square displacements look like they obey a power law of $t^{0.5}$. The normal diffusion regions of methane in polymers begin at rather long time regions (~1000 ps for PDMS and ~300 ps for PE) compared with pure liquid water (~5 ps) and ethanol (~40 ps), and the anomalous diffusion regions are also longer. Müller-Plathe et al.[18] showed a similar plot for diffusion of helium in polyisobutylene (PIB), where the normal diffusion region begins about 100 ps. This is the same order as our system of methane in PE. The system of methane in PDMS requires a longer time simulation to obtain the normal diffusion region. It seems that the more complex the system becomes, the longer the anomalous diffusion region extends. If a diffusion coefficient is calculated from a short time scale simulation for a polymer/penetrant system, it will be overestimated.

Figure 3.3 shows the mean-square displacements. The straight lines show

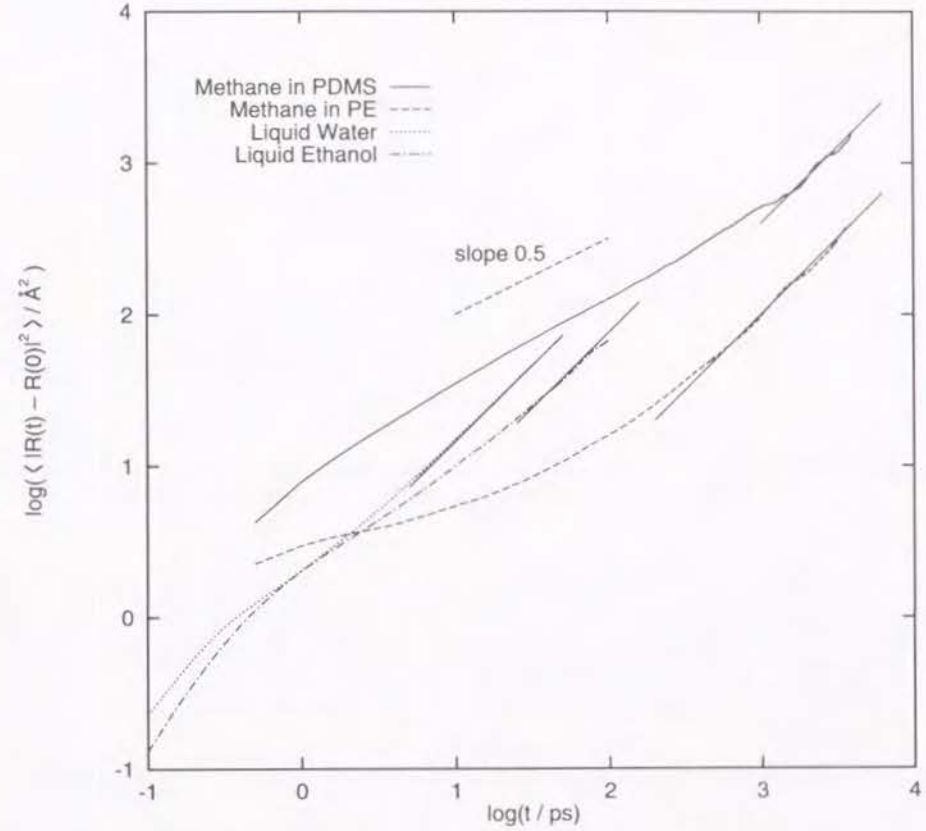

Figure 3.2. Doubly logarithmic plot of mean-square displacements of methane in PDMS and in PE, pure water, and pure ethanol at 300 K. The straight lines along the data, whose slope is unity, indicate the normal diffusion region.

the least-squares fits with the fitting ranges of the normal diffusion regions for each system. The calculated values of the diffusion coefficient D in PDMS and PE are 0.57×10^{-5} and 0.16×10^{-5} cm^2/s, respectively. The value in PDMS is rather small compared with the value 2.1 ($\pm$0.8) $\times 10^{-5}$ cm^2/s calculated by Sok et al. about the same system. They calculated the diffusion coefficient from 250 ps of trajectories of two separate runs, which are rather short compared with our calculation. We divided the 5000 ps of trajectory into

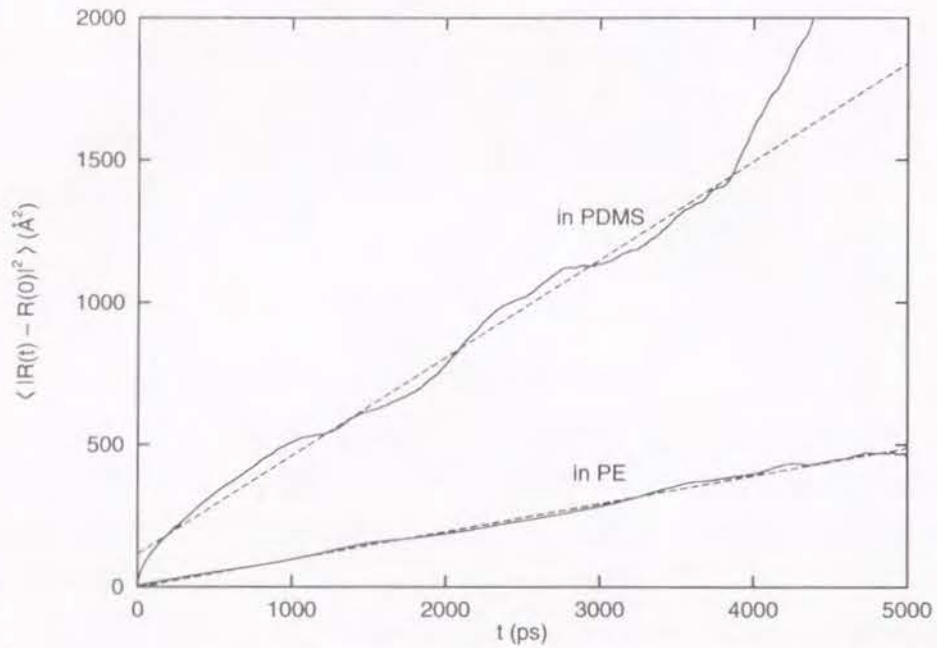

Figure 3.3. Mean-square displacements of methane in PDMS and PE at 300 K calculated from 5000 ps of trajectories. The straight lines show the least-squares fits with the fitting range of the normal diffusion region.

20 subsets of 250 ps and calculated the diffusion coefficients from the mean-square displacements of each subset with the fitting range from 10 to 100 ps. This is a situation similar to that of Sok et al. The calculated diffusion coefficient was 1.6 ($\pm$0.6) $\times$ 10^{-5} cm^2/s, which agreed with the result of Sok et al. This value is also the same as the value calculated from the full trajectory with the fitting range of 10–100 ps and was overestimated by about 3 times as large as the value obtained from the normal diffusion region.

Table 3.2 lists the calculated and experimental diffusion coefficients at 300 K. The diffusion coefficients of liquid water and ethanol are calculated from the trajectories of 50 and 100 ps, respectively. Agreement between the experimental and calculated diffusion coefficients of pure liquid water and ethanol is fairly good. A MD simulation of approximately 100 ps is sufficient to obtain the diffusion coefficients with high precision for the pure liquid systems.

Table 3.2. Calculated and Experimental Diffusion Coefficients

penetrant	matrix	$D \times 10^5$ (cm^2/s)		
		free[a]	aggregate[b]	experiment
methane	PDMS	0.57	—	2.06[c]
water	PDMS	1.53	0.025	1.45[d]
ethanol	PDMS	0.20	0.005	0.45[d]
methane	PE	0.16	—	0.045[e]
water	PE	0.78	—	—
ethanol	PE	0.07	—	—
water	water	2.38	—	2.14[f]
ethanol	ethanol	1.11	—	1.01[g]

[a]The calculated diffusion coefficients of non-aggregated molecules. [b]The calculated diffusion coefficients of aggregated molecules. The aggregation numbers of water and ethanol in PDMS are 5 and 3, respectively. [c]From measurements on PDMS with 4.9 vol % of a silica filler from ref 48. [d]From the transient permeation experiments at 298 K from ref 47. [e]The average value of diffusion coefficients in ref 20, which are corrected for crystallinity. [f]From ref 49 (298 K). [g]From ref 50 (298 K).

On the other hand, the calculated diffusion coefficient of methane in PDMS is approximately one-fourth of the experimental value and that of methane in PE is approximately 4 times larger than the experimental value which is corrected for crystallinity. We could not expect a completely quantitative agreement for the polymer/penetrant systems even if we use very long time trajectories. Our calculated values, however, agree well with the experiments, considering the fact that different experiments often disagree by a factor of 3 or so for polymer/penetrant systems. The united atom approximation raises the calculated diffusion coefficients of penetrants in polymers, as pointed out

by Müller-Plathe et al.[17] for PIB and by Pant and Boyd[20, 21] for PE and PIB; our calculated result for methane in PE is also overestimated. However, the size of the penetrants which we are interested in is large, and the united atom approximation is justified as pointed out by Müller-Plathe et al.[17] Moreover, the discrepancy in our study is the same order as that in PDMS. We expect that the present simulation of the small penetrants in PE and PDMS serves at least as a qualitative comparison for the understanding of the role of polymer–penetrant interaction on the diffusivity.

The diffusion coefficient in PE is about one-fourth that in PDMS. This is a reflection of the narrower distribution of $P(R)$ and $P_{\mathrm{m}}(R)$ in PE than in PDMS.

3.3.3 Diffusion of Water and Ethanol in Polymers

Because water and ethanol tend to form hydrogen bonds in their pure liquids, they may aggregate in a polymer matrix. We performed MD simulation for the systems which contained only one penetrant molecule in the polymer matrix, in order to calculate the diffusion coefficients which were not influenced by aggregation. The concentrations of water and ethanol in PDMS are 0.16 and 0.40 g of solvent/100 g of polymer, respectively, and those in PE are 0.21 and 0.54 g of solvent/100 g of polymer, respectively. MD simulations were performed for 2000 ps.

Figure 3.4a shows the mean-square displacements of water in PDMS and in PE, and Figure 3.4b shows those of ethanol. Straight lines show the least-squares fits with a fitting range of 50–500 ps. Although the mean-square displacements look linear in time, this time scale is supposed to be within the anomalous diffusion region by contrast with the diffusion of methane in polymers (see Figure 3.2). Therefore, the diffusion coefficients will probably be overestimated. The calculated values of diffusion coefficients of water in PDMS and in PE are 1.53×10^{-5} and 0.78×10^{-5} cm^2/s, respectively, and those of ethanol are 0.20×10^{-5} and 0.07×10^{-5} cm^2/s, respectively. The diffusion

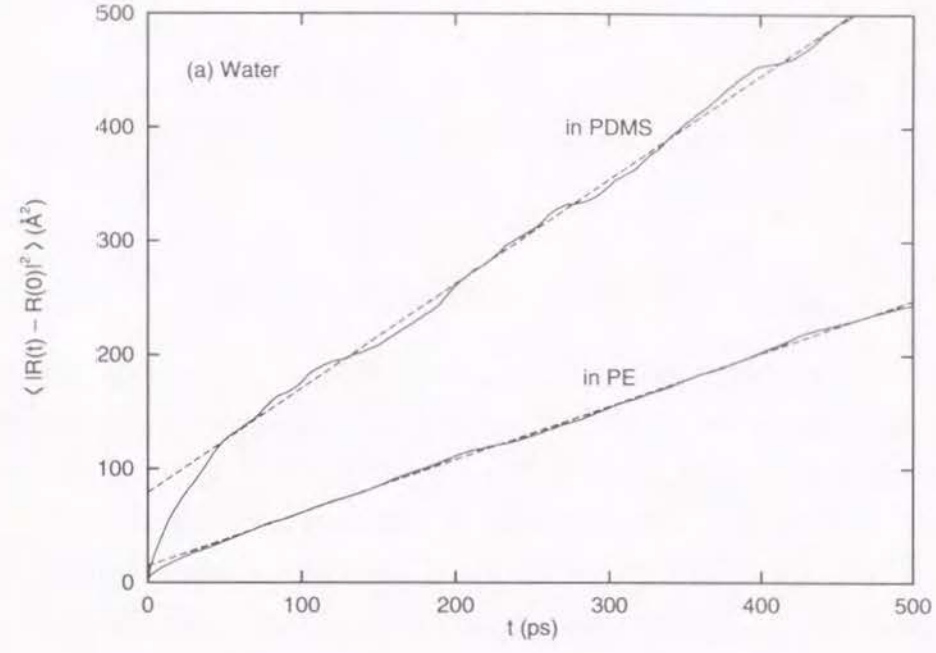

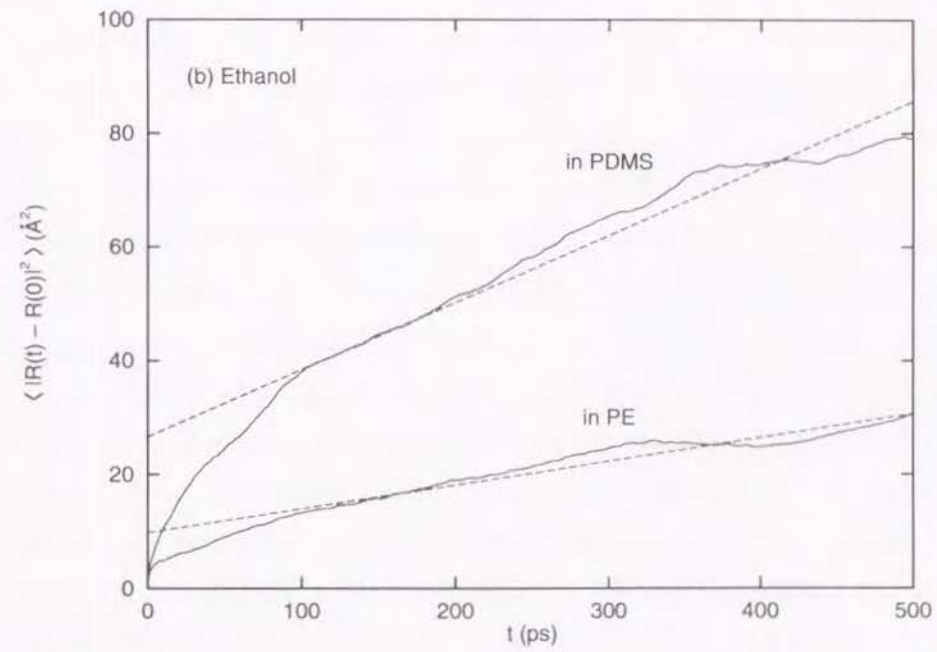

Figure 3.4. Mean-square displacements of (a) water and (b) ethanol in PDMS and PE at 300 K. Each system contains only one penetrant molecule in the polymers. The straight lines show the least-squares fits with a fitting range of 50–500 ps.

coefficients in PDMS are 2–3 times larger than in PE. This is the reflection of the broader distribution of $P(R)$ and $P_{\mathrm{m}}(R)$ in PDMS than those in PE. The diffusion coefficients of ethanol are approximately 1 order of magnitude smaller than those of water.

3.3.4 Aggregation of Water and Ethanol in PDMS

In order to analyze aggregative behavior of water and ethanol, we performed two separate runs of MD simulation for the system which contained five penetrant molecules in PDMS. The concentrations of water and ethanol in PDMS are 0.78 and 1.99 g of solvent/100 g of polymer, respectively. The sampling time of long time runs (run 1) was 2000 ps and that of short time runs (run 2) 500 ps. We calculated the time dependence of the distances between the centers of mass of the penetrant molecules to confirm the degree of aggregation. Figure 3.5 shows the time dependence of the representative pair distances of methane, water, and ethanol in PDMS for run 1. For methane, the last 2000 ps of trajectory was used. Methane is not aggregative, as is expected from its liquid properties. Once two molecules approach close together, then they dissociate again. Methane molecules were dispersed uniformly and did not aggregate in the polymer. On the other hand, the molecules of water and ethanol interact so strongly with each other that they form aggregates. Once forming the aggregates, they did not dissociate to the single molecules.

Table 3.3 shows the index number of molecules which form aggregates and the time t_{a} when the aggregates are formed. Water molecules were dimerized in PDMS, and the aggregates grow further to the larger aggregates of four or five molecules. Ethanol molecules also form aggregates of two or three molecules. Between runs 1 and 2, the qualitatively same aggregative profiles are reproduced. Pure water aggregates more strongly than pure ethanol, as conjectured by the respective boiling points or the heats of vaporization. This effect is carried over to the polymer/penetrant system, since the OPLS and SPC/E force field parameters are adjusted to reproduce the experimental heats

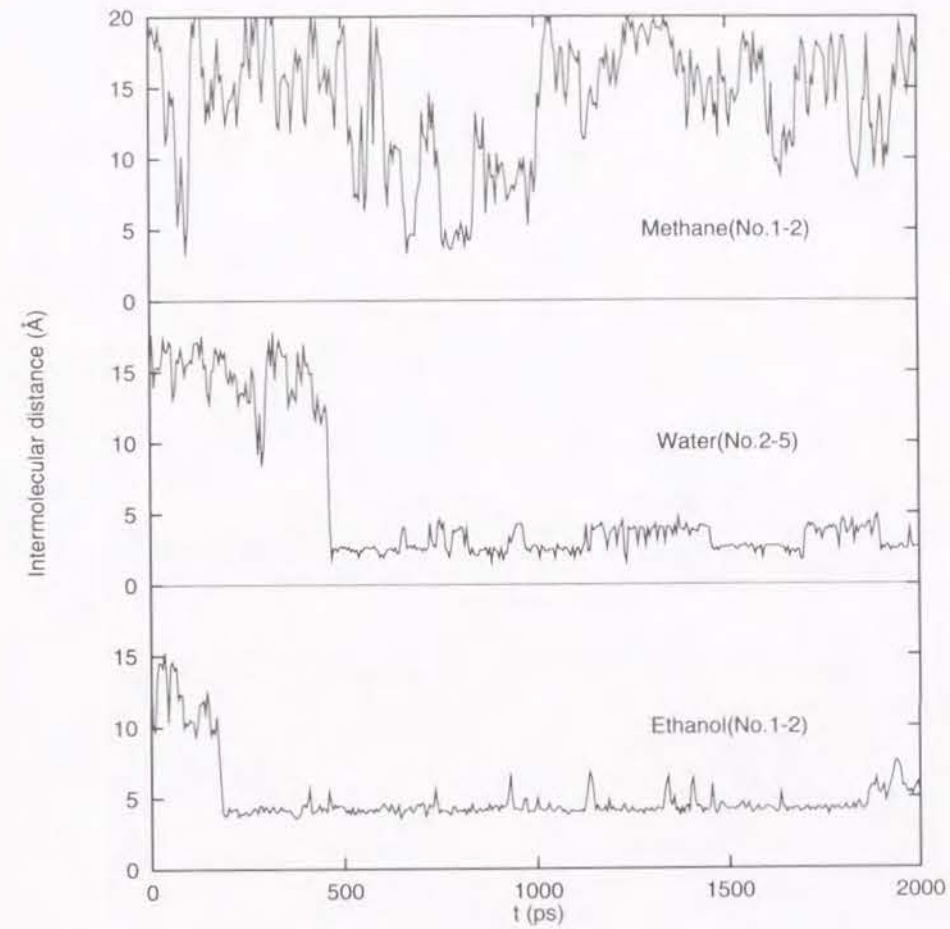

Figure 3.5. Time dependence of the intermolecular distances of the representative pairs of methane, water, and ethanol in PDMS. The index numbers of the molecules are given in parentheses. The noise in the original data is smoothed by displaying 5-ps rolling averages.

of vaporization. On the other hand, ethanol interacts more favorably with the hydrophobic polymer than water. In the PDMS membrane, the aggregate of water is thermodynamically more stable than that of ethanol. Moreover, water has a larger diffusivity than ethanol. Therefore, water has the higher probability which two molecules encounter in PDMS and forms more aggregates than ethanol.

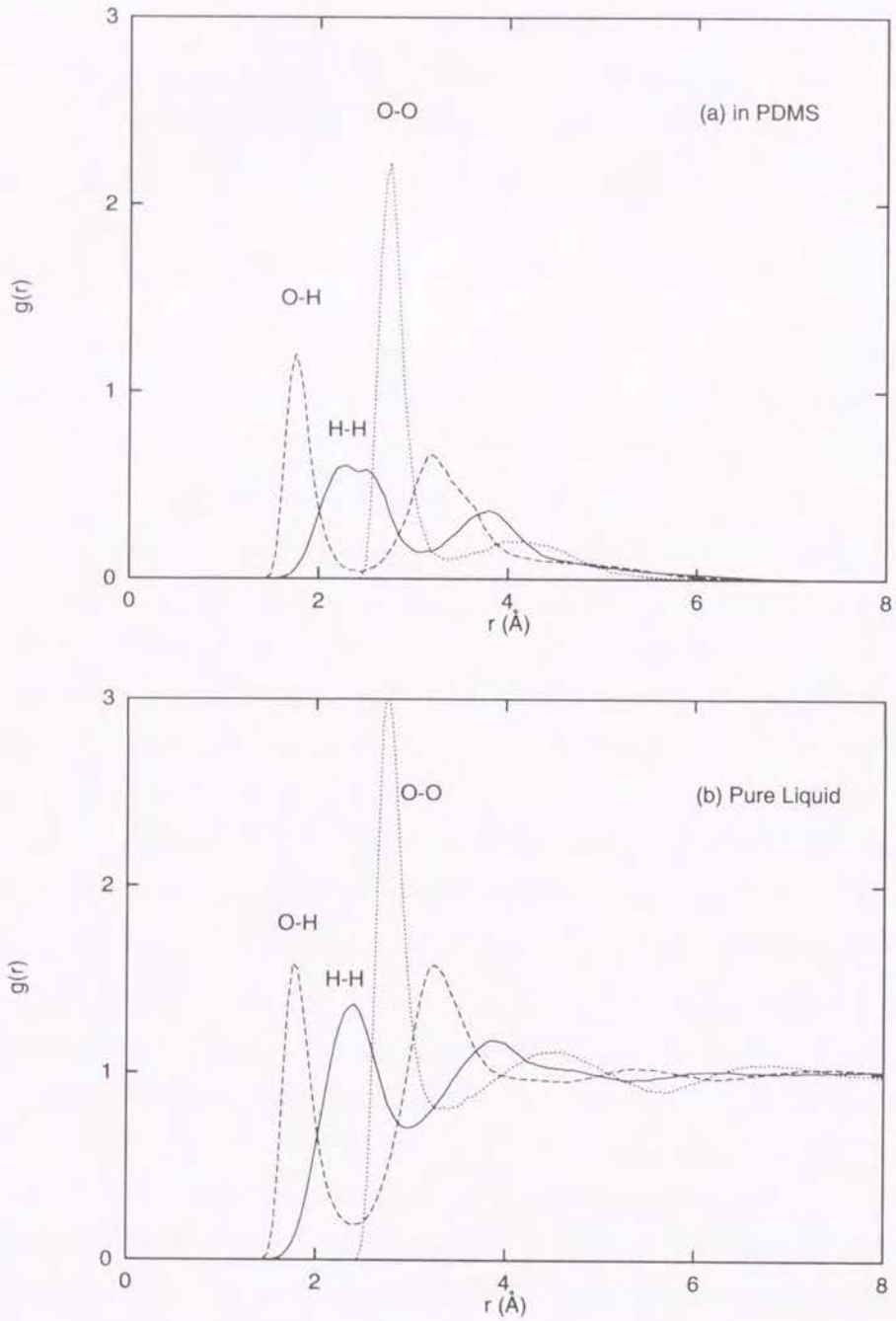

Figure 3.6. Radial distribution functions $g(r)$ of water at 300 K (a) in PDMS and (b) in liquid water. The $g(r)$ in PDMS is normalized by the number density in liquid water.

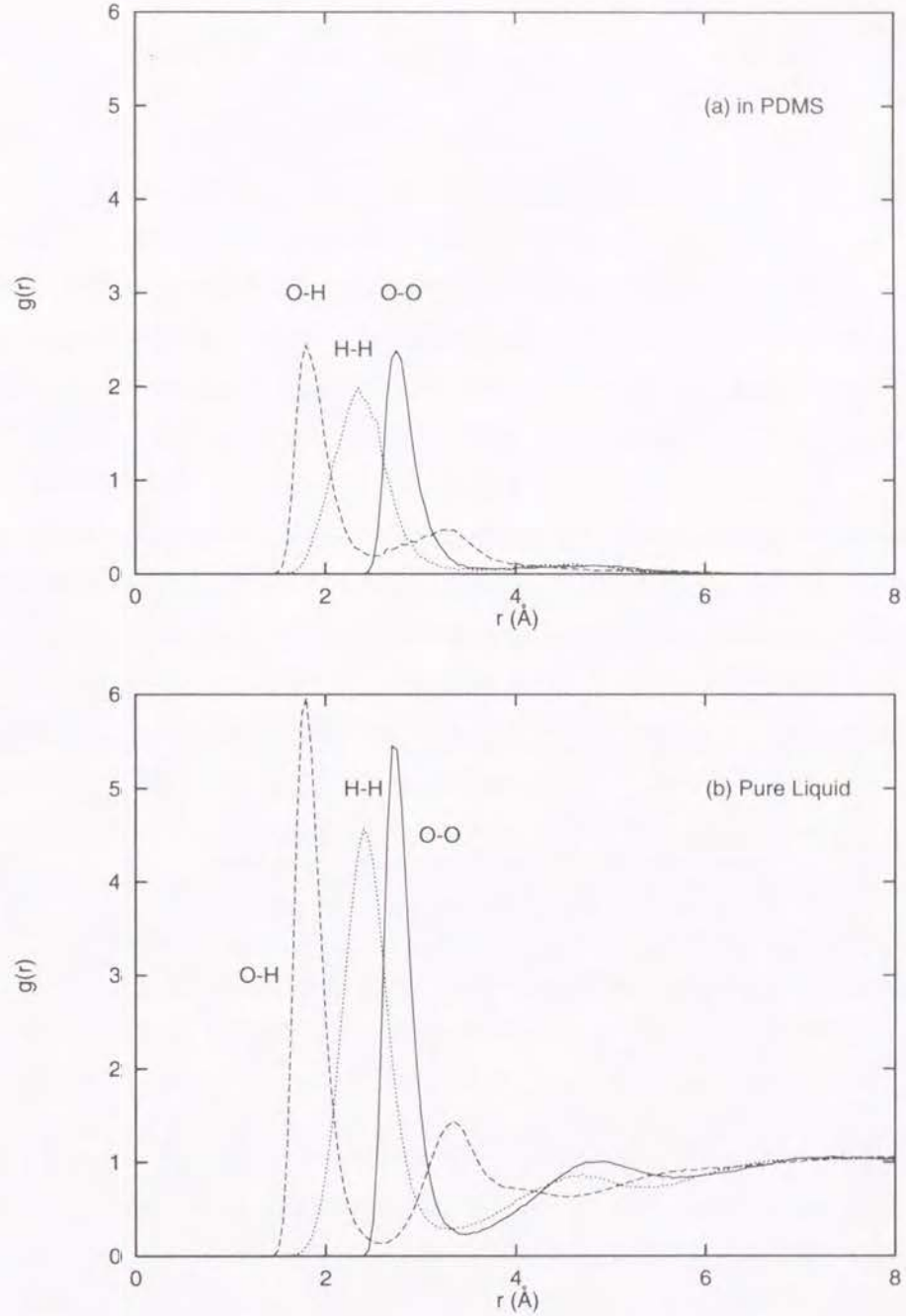

Figure 3.7. Radial distribution functions $g(r)$ of ethanol at 300 K (a) in PDMS and (b) in liquid ethanol. The $g(r)$ in PDMS is normalized by the number density in liquid ethanol.

Table 3.3. Aggregation of Penetrants in PDMS

run number[a]	penetrant[b]	t_a(ps)[c]
	Aggregation of Water	
1	1–5	8
	3–4	40
	1–3–4–5	62
	1–2–3–4–5	469
2	4–5	10
	1–4–5	89
	1–3–4–5	478
	Aggregation of Ethanol	
1	2–3	6
	1–2–3	180
2	3–4	3
	1–5	273

[a]The sampling time of run 1 is 2000 ps (long time runs) and that of run 2 is 500 ps (short time runs). [b]Index number of aggregated penetrant molecules. [c]The time in which the aggregate was formed.

We calculated radial distribution functions of small penetrants in PDMS and in the pure liquids. The radial distribution function of methane shows no significant peak. On the other hand, the radial distribution functions of water and ethanol have some significant peaks due to the aggregation. Figures 3.6 and 3.7 show the results of water and ethanol, respectively. Part a of each figure shows the results in PDMS and part b of each figure those in the pure liquids. The radial distribution functions in PDMS are normalized by the number densities of the pure liquids. The first and second peaks of the radial

distribution functions in PDMS appeared at the exact same radial distances as those in the pure liquids. The hydrogen-bonded structures of the aggregates are supposed to be similar to the those in the pure liquids.

We made the animations of aggregates of water and ethanol in PDMS. Figure 3.8 shows the snapshots. We found that the aggregate of the five water molecules formed a cyclic structure (a), instead of linearly bonded molecules. For the aggregate of the three ethanol molecules, the hydroxyl groups face each other by strong hydrogen bonds, and ethyl groups of ethanol dangled around the center. The structure of the center exchanged between a cyclic one (b) and a linear one (c).

Diffusion coefficients will be affected by the degree of aggregation. We calculated the diffusion coefficients from the trajectories of aggregated penetrant molecules in the long time runs. The aggregation numbers are 5 and 3, the sampling times were 1500 and 1850 ps, and the calculated diffusion coefficients were 2.5×10^{-7} and 0.5×10^{-7} cm^2/s for water and ethanol, respectively. The results are listed in Table 3.2. The diffusion coefficients were decreased to about one-fiftieth by aggregation. The values are very small. We examined the trajectories and displacements from initial positions of the aggregated penetrant molecules in PDMS. The cooperative jump motions of small molecules in the cluster are found in the plots. The motions of the molecules in the aggregate are not the translational diffusion of the whole cluster but the exchange of the penetrant molecules within the same cluster. The diffusion coefficients of the aggregated molecules are virtually zero compared with that of the free molecules.

3.3.5 Comparison with Experiment

Table 3.2 lists the calculated and experimental diffusion coefficients at 300 K. The aggregation numbers of water and ethanol in PDMS are 5 and 3, respectively. The experimental diffusion coefficients D of water and ethanol in PDMS were determined by Okamoto et al.[47] from the transient perme-

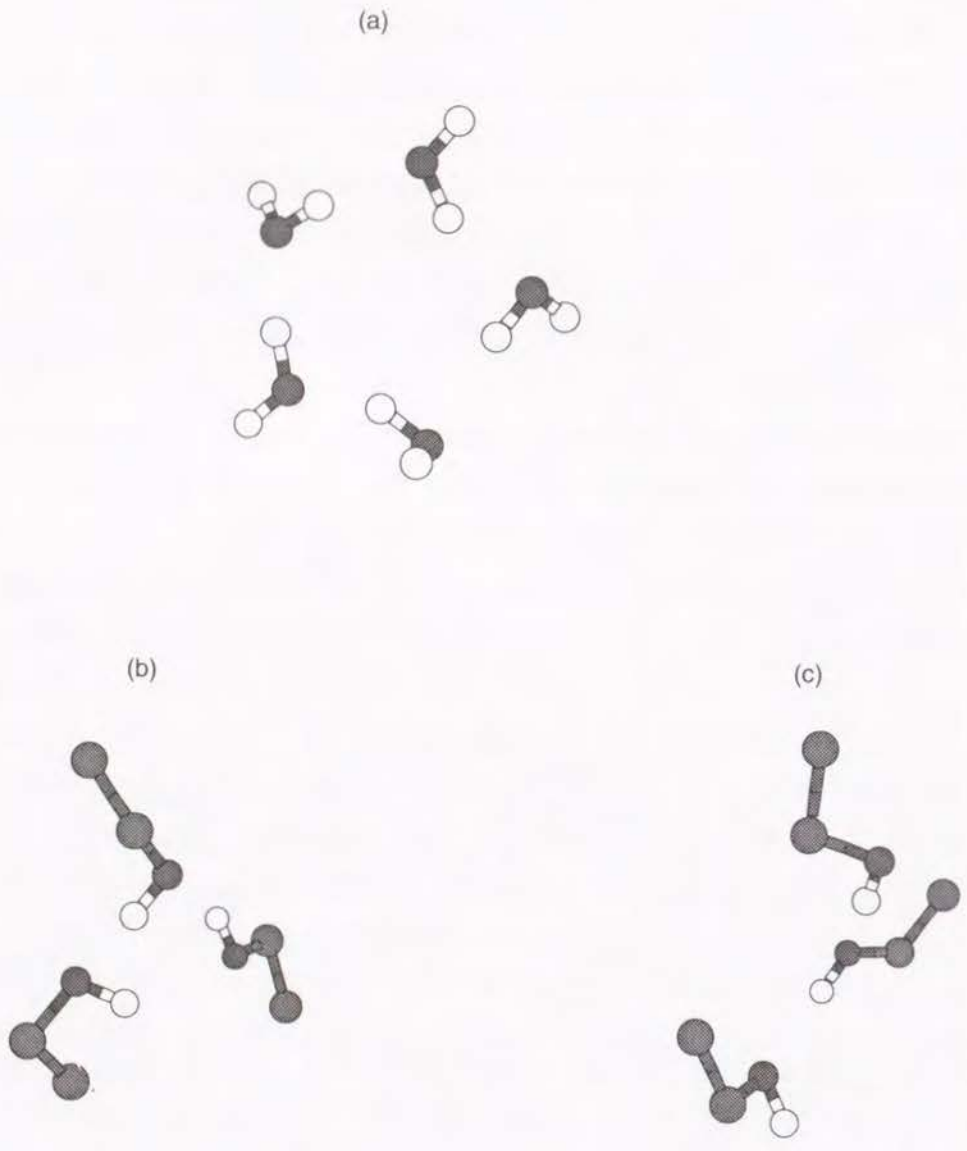

Figure 3.8. Snapshots of aggregated molecules in PDMS: (a) water, (b) cyclic ethanol molecules, and (c) linear ethanol molecules. Open circles indicate hydrogen atoms.

ation experiments for pure components and also for 10 and 30 wt % ethanol solutions. These values agreed with the concentration averaged diffusion coefficients $\bar{D}$ which Okamoto et al. determined from sorption and pervaporation experiments for water/ethanol mixtures in PDMS. The membrane used in the experiment is press-cured pure PDMS, whose density is 0.974 g/cm^3, and is slightly higher than our system. The higher density and the press cure reduce the diffusion coefficients. Our calculated values of diffusion coefficients are supposed to be determined from the anomalous diffusion region, which leads to overestimated diffusion coefficients. Although the condition is slightly different between our calculation and their experiment, we can conclude that the experimental diffusion coefficients are greater than our calculated values of aggregated molecules; the experimental values are closer to the calculated diffusion coefficients of non-aggregated molecules. Taking account of different conditions, the experimental values are slightly larger than the calculated values of non-aggregated molecules.

In the pervaporation experiments, the concentration of the penetrants decreases monotonically from the feed side of the membrane to the permeate side. The aggregation is supposed to have some effect on the diffusion process in the feed side of the membrane but only a little effect on the diffusion in the permeate side or middle of the membrane. Okamoto et al.[47] determined the solubilities of the various concentrations of aqueous solutions of ethanol in PDMS membranes by sorption experiments. Only a small amount of water is dissolved in the PDMS membrane, and there is no experimental value about solubility of pure water. The extrapolated value to the zero concentration is much lower than 0.1 g of solvent/100 g of polymer, which is lower than the concentration of water (0.78) in our system of five water molecules in PDMS. On the other hand, the solubility of pure ethanol in PDMS is 7.45 g of solvent/100 g of polymer, which is higher than the concentration of our system (1.99). Therefore, the effect of aggregation is important for pure ethanol, especially on the feed side of the membrane. At this concentration, the effect

of relaxation of the PDMS chains by ethanol is also important. Although the former effect decreases the diffusion coefficient, the latter effect increases it. At the intermediate concentration (~50 wt %) of the aqueous solution of ethanol, which is the usual case for pervaporation using a PDMS membrane, the experimental solubility of ethanol is about 0.5 g of solvent/100 g of polymer, which is lower than the concentration of our system. This order of solubility, however, does not assure that the aggregation of penetrants is not formed.

It is generally known that clustering of water molecules in polymers is allowed in usual experiments. The solubility of pure water in PDMS is very low. When polymer chains are relaxed by ethanol molecules, however, water molecules are soluble in some regions of the membrane; the regions where clusters of water are formed and grow. The diffusion coefficient of aggregated penetrants is virtually zero, as shown in our simulation. The fact that the experimental diffusion coefficient is so much closer to the value for free molecules is explained as follows. The penetrants form clusters in suitable holes in the polymer, where they are immobilized. Once all the holes are filled, any additional penetrant can be regarded as free, and only free penetrants contribute appreciably to the overall transport.

This aspect agreed with the experiments of Okamoto et al.[47] In their experiments, the concentration-averaged diffusion coefficients $\bar{D}$ for each component, which are determined from pervaporation, were independent of the feed composition. The values of D for each component, which are determined from the transient permeation experiments for the vapor of pure components, were in fairly good agreement with the values of $\bar{D}$. Moreover, the values of D for water and ethanol, which are determined from the transient permeation experiments for 10 and 30 wt % ethanol solutions, were the same as the values for pure components. The experimental results led to the conclusion that water and ethanol molecules permeate separately in the membrane as isolated molecules.[47] Our calculated result supports this view.

Our calculated values for non-aggregated penetrant molecules are in good

agreement with the experimental values. Taking the difference of the conditions between the simulation and the experiment into consideration, the calculated values tend to be lower than the experiments. The average pressure, which is calculated on an atomic basis for the system of a ethanol molecule in PDMS, is negative several tens MPa. The negative pressure leads to an over-estimate of the diffusion coefficients for very small penetrants. For comparatively large penetrant molecules and clusters, however, the restriction of constant volume and constant shape of the unit cell, which was used in our simulation, may reduce the diffusivity by suppressing the motion of large free holes. For the system of ethanol in PDMS, the relaxation effect of polymer chains by ethanol molecules, which is observed in the experiment, raises the diffusivity. This effect may not be sufficiently included in this simulation.

3.4 Conclusion

The larger free volume and broader free volume distribution of PDMS result in the 3 times higher diffusion coefficients of methane, water, and ethanol in PDMS than in amorphous PE. Although there are some difficulties in obtaining quantitative agreement, the calculated diffusion coefficients of the non-aggregated penetrant molecules agree reasonably with the experiments. Since water and ethanol have aggregative nature, they form aggregates in PDMS on our MD simulations for the systems which contain more than a single penetrant in the unit cell. The hydrogen-bonded structures of the aggregates are similar to those in the pure liquids. The calculated diffusion coefficients of aggregated molecules in PDMS are virtually zero, and those of free molecules are close to the experiments. This implies that the overall transport is ascribed to diffusion of free penetrants.

In this chapter, the diffusional motion of small penetrants was detected by the mean-square displacement and by the displacement of penetrants and was linked to the static property of polymers, the insertion probability. The mechanism of the diffusion process was, however, not fully elucidated. The diffusion

of small penetrants is connected with the dynamics of polymer chains. Cooperative motion is very important especially for the system of large penetrants which have internal degrees of freedom, or polar penetrants in polymers. The mechanism of diffusion will be treated in an upcoming paper.

Ethanol has a smaller diffusion coefficient than water in PDMS but has a larger permeation rate. The reason for this is that ethanol has a larger solubility than water. It is necessary to examine solubility in terms of various components such as free volume and the interaction potential for comprehension of the permeation phenomena of small penetrants in the membranes. The solubility of small molecules in polymers are analyzed in Chapter 4.

Chapter 4

Solubility of Small Penetrants in Polymers

4.1 Introduction

In the previous chapter, we have studied the diffusion process of methane, water, and ethanol in PDMS and in PE by MD simulations and obtained diffusion coefficients which agree reasonably with those from experiments. In this chapter, we consider the solubilities of small penetrants by molecular simulation techniques.

On the surface of membranes, the polymer/penetrant system is in equilibrium with the gas phase (in the case of gas separation) or the liquid phase (in the case of liquid separation such as pervaporation). The solubility of a small penetrant depends on the difference in chemical potentials between two phases. Excess chemical potentials can be calculated by the Widom test particle insertion method.[2] Alternatively, the phase equilibrium can be simulated directly by the Gibbs ensemble method.[3] These methods have been applied mainly to Lennard-Jones fluids. Nowadays, the Widom method is applicable also to polymer/penetrant systems. Müller-Plathe[51] calculated the excess chemical potentials of helium, hydrogen, nitrogen, oxygen, and methane in amorphous atactic polypropylene (a-PP). Sok et al.[15] calculated those of methane in PDMS, and Müller-Plathe et al.[19] those of methane, hydrogen, and oxygen in polyisobutylene (PIB). In those studies, the excess chemical potentials are overestimated compared with experimental data. The excess chemical potential of small molecules in PIB which Gusev and Suter[46] calculated by the mean-field method was also overestimated. Müller-Plathe et al.[19] commented that these deviations could not be accounted for by incomplete-

ness of the potential functions. They pointed out that the deviations could be caused by the non-uniformity of the amorphous polymer structure in the simulation; a small number of large holes exist in the starting structure and do not relax during the simulation time.

Thus far studies for polymer/penetrant systems have treated the excess chemical potential of small nonpolar molecules (mono-atomic or di-atomic). In this study, we consider polar molecules (water and ethanol) and a molecule which has internal degrees of freedom (ethanol). In these cases, it is difficult to obtain the excess chemical potentials with a certain precision. The Widom method needs to be combined with methods which raise the sampling efficiency. The excluded volume map sampling (EVMS) method,[30] in which no trial insertion is attempted in the region in which matrix atoms exist, has been generally used to increase the efficiency of sampling. For large molecules, we can raise the efficiency by biasing the orientation and the dihedral angles of a test molecule. Cracknell et al.[52] simulated the liquid–vapor equilibrium of water by the grand canonical ensemble Monte Carlo (MC) method and by the Gibbs ensemble method. The rotational insertion bias (RIB) method which biases the orientation of a trial insertion was used in their study. It was shown that the acceptance rate was increased by a factor of two. Using the continuum configurational bias (CCB) method, which biases the dihedral angles of an inserted molecule, de Pablo et al.[31] calculated the chemical potentials of linear hydrocarbons of carbon numbers up to 15 by the Widom method. Laso et al.[53] applied the method to the Gibbs ensemble simulation and examined phase equilibria of hydrocarbons.

Kumar et al.[54] applied an alternative method in which the chemical potential of a segment was calculated. The segmental chemical potential did not depend on the chain length for a long chain polymer which could be treated as the Gaussian chain. Sheng et al.[55] studied phase equilibria of polymer systems with this method, and Kumar[56] considered polymer blend systems. This method, however, cannot be applied to short chain molecules because the

segmental chemical potentials depend strongly on the chain length for these systems.

In this chapter, the excess chemical potentials of methane, water, and ethanol in PDMS and PE and those in aqueous ethanol solutions (0, 50, 100 wt %) are calculated by the Widom test particle insertion method and are compared to those by the Shing–Gubbins method.[28, 29] The solubility of small molecules in the polymers has a simple relation to the excess chemical potential. The permeation rates of the small molecules in the polymers are calculated from the diffusion coefficients and the solubilities. The energy maps of ghost molecules are analyzed in order to establish a relation between the free volume and the solubility of a small molecule.

4.2 Model and Simulation Details

4.2.1 Model and Potential Functions

The PDMS and PE samples are modeled as described in Chapter 2. Simulations are carried out for systems containing five polymer chains in a cubic periodic box at the following experimental densities: 0.95 g/cm^3 for PDMS and 0.855 g/cm^3 for PE. The degree of polymerization x of each chain is 30 for PDMS and 60 for PE. There are no cross-links and branches. All calculations were performed on CRAY Y-MP2E supercomputer using the molecular simulation program PAMPS which we coded. The AMBER/OPLS force field is used except for PDMS and water. The GROMOS force field is used for PDMS, and the SPC/E for water. All CH_4, CH_3– and –CH_2– groups are treated as united atoms. A detailed description of the potential functions is given in Appendix A.

4.2.2 MD Simulation

The trajectories of amorphous PDMS and PE are obtained by MD simulations at 300 K under constant NVE conditions in Chapter 2. The simulations

for aqueous ethanol solutions (0, 50, 100 wt %) are carried out under constant NPT conditions using the Nosé–Andersen method as described in Appendix D. The pressure is calculated from the atomic virial. The volume scaling is performed by atomic basis. The Lennard-Jones interactions are cut off at $r_{\rm cut} = 10$ Å. The contributions to the pressure and the potential energy from the long tail of the pair potential are estimated by assuming that the radial distribution function $g(r)$ is unity for $r > r_{\rm cut}$.[57] The Ewald sum was used for the calculation of the Coulombic interaction. The MD simulations are performed for aqueous ethanol solutions whose concentrations are 0 wt % (328 water molecules), 50 wt % (164 water molecules and 64 ethanol molecules), and 100 wt % (128 ethanol molecules). All the bond lengths and the bond angles are kept constant by the SHAKE algorithm. A time step of 0.5 fs is used. The molecules are confined in a cubic periodic box whose size is determined from the experimental density. After a steepest descent energy minimization, MD simulations are performed at 0.1 MPa and 300 K. After the systems are equilibrated, a trajectory of 100 ps is sampled for each system. The average unit cell lengths are 21.44, 22.35, and 23.52 Å for 0, 50, and 100 wt % solutions, respectively.

4.2.3 Particle Insertion Method

In the Widom method, insertion trials of test molecules are attempted for the systems which are obtained from the MD simulations. The excess chemical potential $\mu_{\rm r}$ is calculated as

$$\mu_{\rm r} = -kT \ln\langle \exp(-\psi/kT)\rangle_N \tag{4.1}$$

where ψ is the potential energy of the inserted (ghost) molecule with surrounding real molecules, and $\langle \ldots \rangle_N$ denotes the ensemble average over N molecules of the host matrix. For the NPT ensemble, eq 4.1 is replaced by

$$\mu_{\rm r} = -kT \ln \left[\frac{\langle V \exp(-\psi/kT)\rangle_{NPT}}{\langle V \rangle_{NPT}} \right] \tag{4.2}$$

All the interactions are calculated in the same way as in the MD simulations. The interaction between a ghost molecule and its image is not included in the calculation. This is the situation in which a ghost molecule is inserted into a infinitely spreading matrix.

The EVMS (excluded volume map sampling) method[30] is used to increase the efficiency of sampling. For aspherical molecules, such as water and ethanol, an excluded volume map is constructed for the oxygen atom. The unit cell is divided into 100 × 100 × 100 grid points. If a grid point located at $\mathbf{r}_t$ satisfies the condition

$$|\mathbf{r}_t - \mathbf{r}_i| \le a\sigma_{ti} \tag{4.3}$$

where $\mathbf{r}_i$ is the position of a host atom i, σ_{ti} is the Lennard-Jones size parameter between the atoms t and i, and a is an empirical parameter, the grid point belongs to a family of excluded volume. Since the Boltzmann factor of the ghost molecule is approximately zero in the excluded volume, the insertion trials are attempted only at the grid points which are out of the excluded volume; the Boltzmann factor is multiplied by the weight $f_{\rm v}/N_{\rm s}$, where $f_{\rm v}$ is a non-excluded volume fraction and $N_{\rm s}$ is the number of samples for this configuration. We tested several values of the empirical parameter a and determined suitable values for a by referring to the energy distribution functions. The larger the value of a, the more the regions are excluded, and the greater the efficiency of EVMS. If the value a is too large, low-energy regions are also excluded and the calculated value of $\mu_{\rm r}$ is estimated erroneously by EVMS. In the case of $a = 1.0$, the absolute value of $\mu_{\rm r}$ is obviously underestimated by EVMS. For $a \le 0.9$, $\mu_{\rm r}$ is independent of a. In this study we use $a = 0.8$ for all systems.

In the insertion of chain molecules, the CCB (continuum configurational bias) method[31] is used in combination with the EVMS method to increase the efficiency of the dihedral angle sampling. In this method, the chain of a test molecule is grown site by site in a way similar to the modified self-avoiding random walk method which was used for the generation of the initial structure

of the polymers. A dihedral angle is chosen among n_{dis} discretized points, which are equally spaced, with the probability

$$W_j = \frac{w_j}{\sum_{k=1}^{n_{\mathrm{dis}}} w_k} \tag{4.4}$$

where w_j is the Boltzmann factor $\exp(-U_j/kT)$ for the jth discretized position of the dihedral angle. U_j is the interaction energy of the adding position j, which interacts with the atoms in the host matrix and also with the atoms in the already inserted part of the ghost molecule. The dihedral angle $[-\pi, \pi]$ is discretized into n_{dis} equally spaced values, the first of which is chosen at random. The excess chemical potential is calculated as

$$\mu_{\mathrm{r}} = -kT \ln\langle W^{(m)} \exp(-\psi/kT)\rangle_N \tag{4.5}$$

where

$$W^{(m)} = \prod_{l=1}^{m} \left(\frac{1}{W_{jl} n_{\mathrm{dis}}}\right) \tag{4.6}$$

where m is the number of dihedral angles in a ghost chain and W_{jl} is equal to the value of W_j (eq 4.4) when the position of the lth dihedral angle is j. ψ is the potential energy of the inserted ghost molecule which has a set of dihedral angles, $[j_1, j_2, \ldots, j_m]$. For ethanol, the insertion trial of the head group, H–O–CH_2–, is made with a random orientation, applying the EVMS method for the oxygen atom, and subsequently the –CH_3 group is inserted by the CCB method. The number of discretization of the dihedral angle n_{dis} is 12 in our calculations.

4.2.4 Shing–Gubbins Method

The ghost molecule energy distribution function

$$f(U) = \frac{\int \delta(\psi - U)\exp(-\Psi/kT)\mathrm{d}\mathbf{q}_0\mathrm{d}\mathbf{q}_1\ldots\mathrm{d}\mathbf{q}_N}{\int \exp(-\Psi/kT)\mathrm{d}\mathbf{q}_1\ldots\mathrm{d}\mathbf{q}_N} \tag{4.7}$$

is calculated by the Widom method, where $\mathbf{q}_i$ is the coordinate of the ith molecule, including the coordinate of the center of mass, the orientation, and the internal degrees of freedom of the molecule. The coordinate of the test molecule is denoted by $\mathbf{q}_0$. $\Psi = \Psi(\mathbf{q}_1, \mathbf{q}_2, \ldots, \mathbf{q}_N)$ is the total potential of the N molecules system, $\psi = \psi(\mathbf{q}_0; \mathbf{q}_1, \mathbf{q}_2, \ldots, \mathbf{q}_N)$ is the potential of the inserted molecule with all other molecules, and δ is the Dirac delta function. The ensemble average is taken for the N host molecules. The value $f(U)\mathrm{d}U$ is the probability that the interaction energy between the test (ghost) molecule and the host molecules lies in the range U to $U + \mathrm{d}U$.

The real molecule energy distribution function

$$g(U) = \frac{\int \delta(\psi - U)\exp(-\psi/kT)\exp(-\Psi/kT)\mathrm{d}\mathbf{q}_0\mathrm{d}\mathbf{q}_1\ldots\mathrm{d}\mathbf{q}_N}{\int \exp(-\psi/kT)\exp(-\Psi/kT)\mathrm{d}\mathbf{q}_0\mathrm{d}\mathbf{q}_1\ldots\mathrm{d}\mathbf{q}_N} \tag{4.8}$$

is also calculated by the inverse-Widom method.[28, 29] The ensemble average is taken for the $N + 1$ molecules including the test (real) molecule. The value $g(U)\mathrm{d}U$ is the probability that the interaction energy between the test (real) molecule and the host molecules is in the range U to $U + \mathrm{d}U$.

The ratio of eq 4.7 and eq 4.8 leads to

$$\ln\left[\frac{f(U)}{g(U)}\right] = \frac{U}{kT} - \frac{\mu_{\mathrm{r}}}{kT} \tag{4.9}$$

This implies that a plot of $\ln[f(U)/g(U)]$ versus U has a slope of $1/kT$ and an intersection with the zero-energy axis of $-\mu_{\mathrm{r}}/kT$.[28, 29]

4.2.5 Solubility in Polymer

The solubility of a small penetrant in the ideal gas phase is calculated by

$$S_{\mathrm{g}} = \exp(-\mu_{\mathrm{r}}/RT) \tag{4.10}$$

where the solubility S is defined as the ratio of the number densities between two phases. The solubility of a small penetrant in the liquid phase is calculated

by

$$S_l = \exp(-\Delta\mu_r/RT) \tag{4.11}$$

where $\Delta\mu_r = \mu_r^p - \mu_r^l$, and μ_r^p and μ_r^l are the excess chemical potentials in a polymer and in a liquid, respectively. In this study, we ignore any structural change which may occur in the membrane from the absorption of small penetrants.

4.3 Results and Discussion

4.3.1 Simulation of Aqueous Ethanol Solution

The MD simulations were performed for the aqueous ethanol solutions (0, 50, 100 wt %) under constant NPT conditions. Phase separation was not observed for the ethanol 50 wt % solution; ethanol mixed with water uniformly.

Table 4.1. Densities and Diffusion Coefficients of Aqueous Ethanol Solutions

c (wt %)	ρ (g/cm^3)	$D \times 10^5$ (cm^2/s)	
		ethanol	water
	Calculated		
0	0.995		2.63
50	0.878	0.71	1.62
100	0.752	1.21	
	Experimental[a]		
0	0.9965		2.14
50	0.91		
100	0.7851	1.01	

[a] From refs 37, 79, 49, and 50.

Table 4.1 lists the densities and diffusion coefficients calculated from the MD simulations. The density of pure water agrees well with the experimental data. The densities of pure ethanol and 50 wt % ethanol solution are approximately 4% smaller than the experimental data. Jorgensen[79] simulated pure liquid ethanol by the NPT Monte Carlo method using the OPLS potential. He obtained a density of 0.748 ± 0.003 g/cm^3, which agrees with our value. The diffusion coefficients of pure water and ethanol agree well with the experimental values. The diffusion coefficients which are calculated in Chapter 3 from the MD simulation under the constant NVT conditions at the experimental densities are 2.38×10^{-5} and 1.11×10^{-5} cm^2/s, which are almost the same as the values from the NPT simulations. The difference in density (4%) leads to the difference in the diffusion coefficient. In the 50 wt % aqueous ethanol solution, the diffusion coefficient of ethanol is smaller than that in the pure liquid.

4.3.2 Ghost Molecule Energy Distribution Function

The ghost molecule energy distribution function $f(U)$ was calculated by the Widom method. For the polymer/penetrant systems, 1000 coordinates were used as host matrices, and 10 000 insertion trials were performed for each coordinate. For the systems of the aqueous ethanol solutions (0, 50, 100 wt %), 10 000 coordinates were used as host matrices, and 1000 insertion trials were performed for each coordinate.

Figure 4.1a shows the $f(U)$ of water and ethanol in the aqueous ethanol solutions. Figures 4.2a and 4.3a show the $f(U)$ of methane, water, and ethanol in PDMS and in PE, respectively. Since the raw histograms of $f(U)$ fluctuate greatly in low-energy regions, the distribution functions were smoothed by the running average method in which an average value of the successive three columns of the histogram is put into the central column. This operation was applied to all columns, shifting the columns sequentially. The procedure was repeated three times to get the distribution functions shown in the figures.

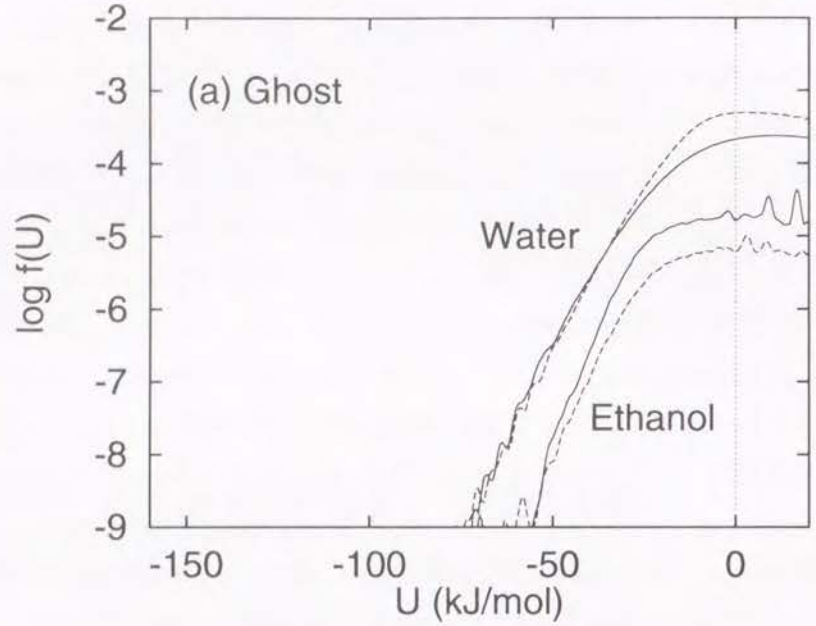

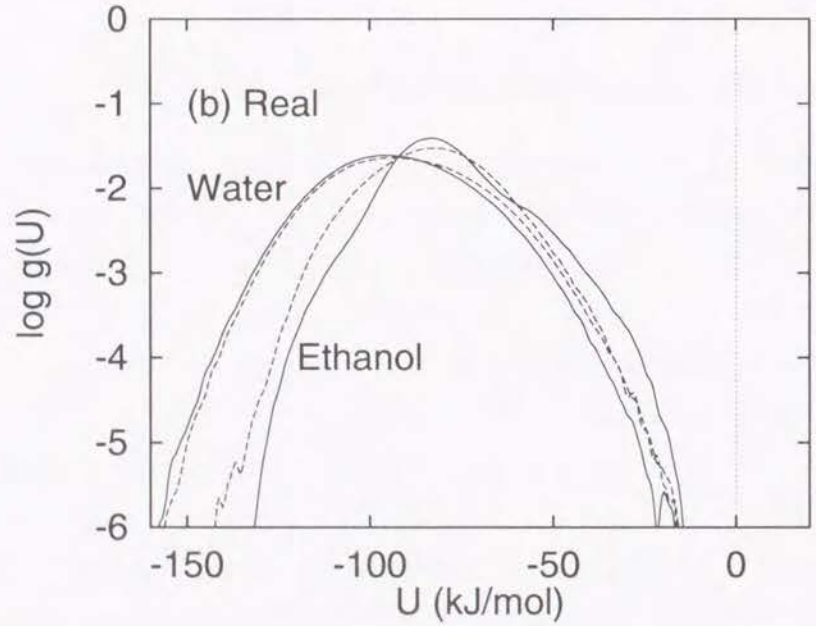

Figure 4.1. Energy distribution functions (a) $f(U)$ and (b) $g(U)$ of water and ethanol in aqueous ethanol solutions: (solid lines) in the pure liquids (water in water and ethanol in ethanol); (dashed lines) in the 50 wt % solutions.

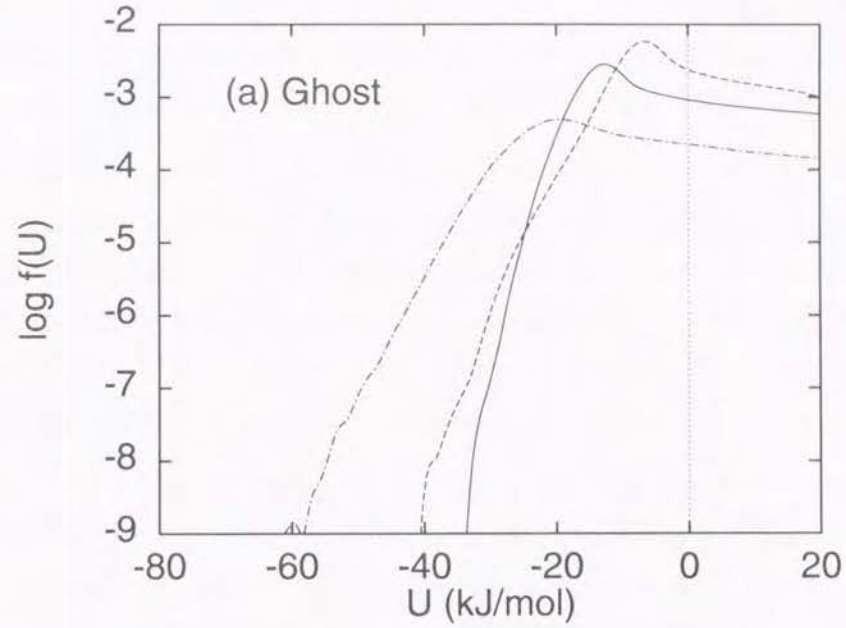

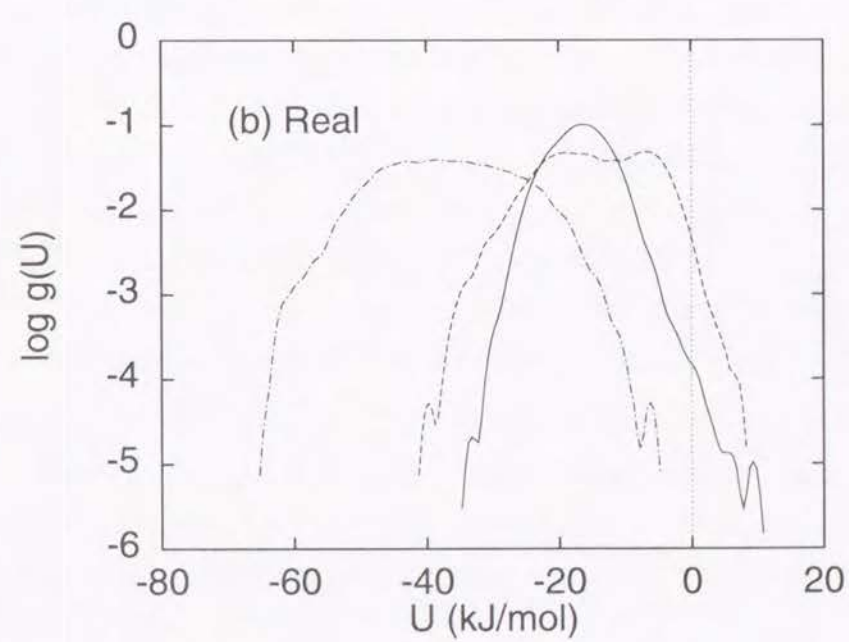

Figure 4.2. Energy distribution functions (a) $f(U)$ and (b) $g(U)$ of small molecules in PDMS: (solid line) methane; (dashed line) water; (dashed-dotted line) ethanol.

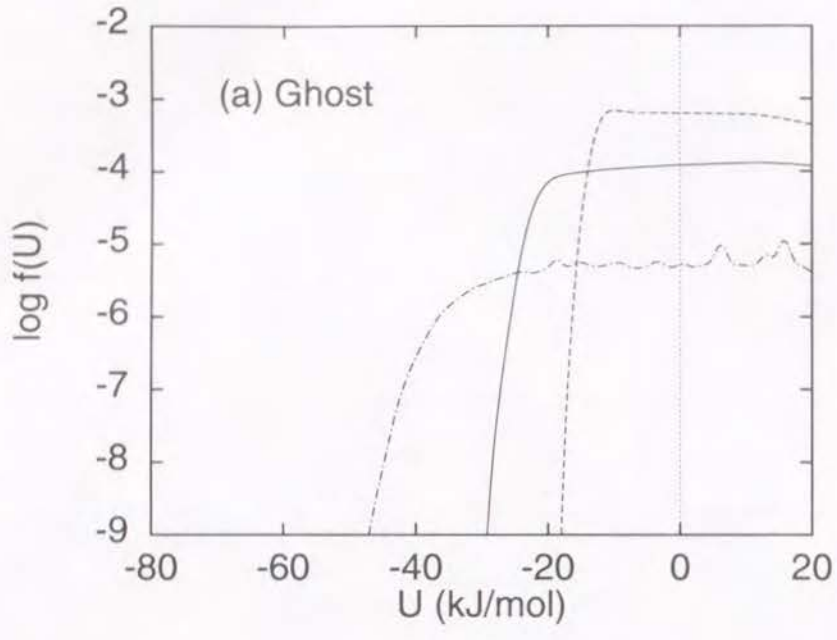

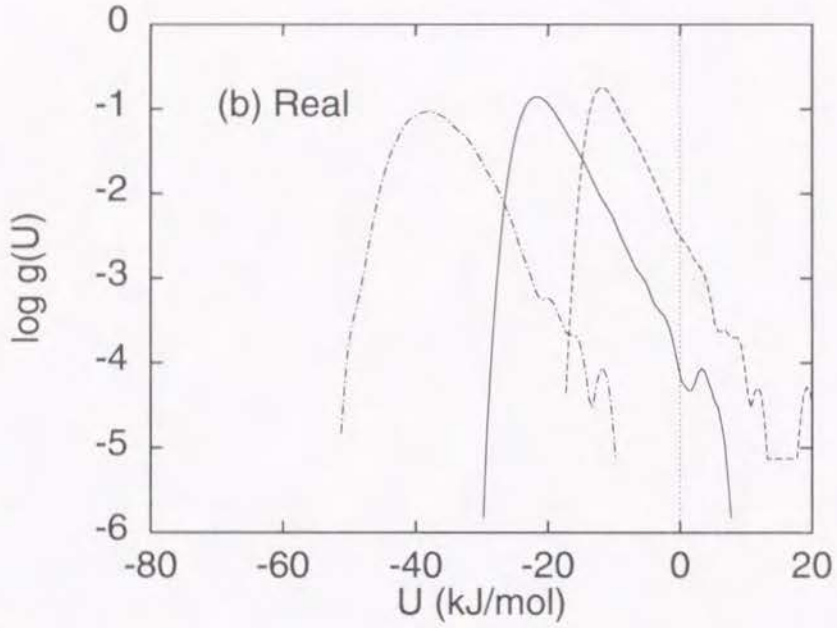

Figure 4.3. Energy distribution functions (a) $f(U)$ and (b) $g(U)$ of small molecules in PE: (solid line) methane; (dashed line) water; (dashed-dotted line) ethanol.

Although the insertion probability is very low in the insertion of ethanol into the aqueous ethanol solutions, the distribution functions are rather smooth. This shows the advantage of the use of the EVMS and the CCB methods.

In Chapter 2, we calculated the insertion probability $P(R)$ of a hard sphere atom into PDMS, PE, water, and ethanol and showed that PDMS had a broader distribution of the free volume than the other systems. In PDMS, the distribution of $f(U)$ has a larger peak than that in any other system. This arises from the broader distribution of free volume. This accounts for the observation that larger molecules are soluble in PDMS.

Since the Lennard-Jones size parameter of water is smaller than that of methane, the $f(U)$ of water in the polymers is larger than that of methane in the high-energy region. Water also has a smaller value of the Lennard-Jones energy parameter. Therefore, in PE, where only the Lennard-Jones term contributes to the interaction, the distribution of the $f(U)$ of methane spreads to the lower energy region whereas that of water is approximately zero below $U = -20$ kJ/mol. The same tendency as in PE is observed in PDMS for $U > -20$ kJ/mol. The difference is found at $U < -20$ kJ/mol; the distribution of the $f(U)$ of water spreads to a lower energy region than methane because of the weak Coulombic interaction. Since ethanol has a larger molecular size than water or methane but a greater Lennard-Jones interaction, the distribution of the $f(U)$ of ethanol is spread to the lower energy region.

There exists a peak in the $f(U)$ of PDMS. In the energy range where the peak in $f(U)$ is found, the ghost molecule feels moderate Lennard-Jones attractive interactions. Therefore, large holes exist in PDMS and the effective insertion trials are attempted mainly in the holes. We will discuss this point in a later subsection.

Using $f(U)$, μ_{r} is expressed as

$$\mu_{\mathrm{r}} = -kT \ln I(\infty) \tag{4.12}$$

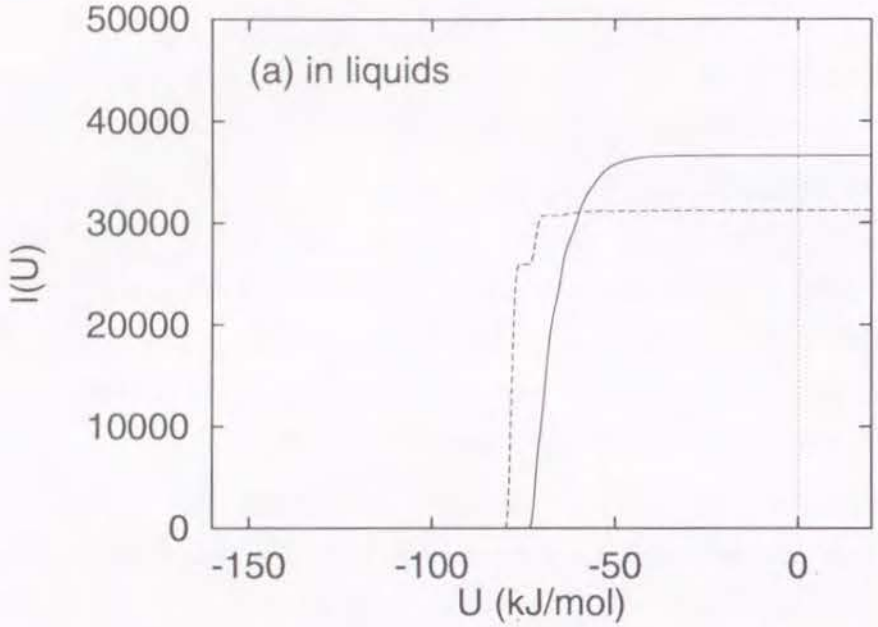

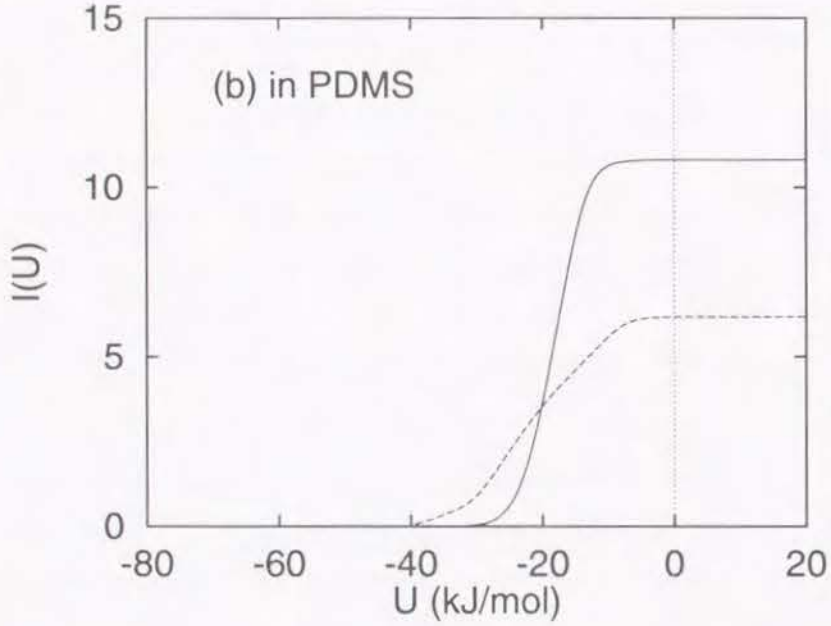

Figure 4.4. Plots of $I(U) = \int_{-\infty}^{U} f(u)\exp(-u/kT)\mathrm{d}u$ of small molecules: (a) (solid line) water in pure water, (dashed line) ethanol in the 50 wt % aqueous ethanol solution; (b) (solid line) methane in PDMS, (dashed line) water in PDMS.

where

$$I(U) = \int_{-\infty}^{U} f(u)\exp(-u/kT)\mathrm{d}u \tag{4.13}$$

as plotted in Figure 4.4. The solid line in Figure 4.4a shows the $I(U)$ of pure water, and the dashed line shows that of ethanol in the ethanol 50 wt % solutions. For water, half the contribution to $I(U)$ arises from the energy range of $U < -68$ kJ/mol. The low-energy configurations which form the hydrogen-bond contribute significantly to the calculated value of μ_{r}. The configuration of $U = -78$ and -72 kJ/mol were "incidentally" sampled for ethanol. These two energy points contribute to the main part of $I(U)$. The value of μ_{r} for ethanol in the 50 wt % solution calculated from eq 4.12 was -23.7 kJ/mol. (The value is corrected by subtracting the contribution from the dihedral angle potential, as described in a later subsection.) If we ignore the samples with $U = -78$ and -72 kJ/mol, the value of μ_{r} becomes -13.3 kJ/mol, which is approximately 10 kJ/mol higher than the original value. The probability that a ghost molecule forms hydrogen bonds with the matrix molecules is very low for ethanol. If the hydrogen-bonded configuration is incidentally sampled, the fluctuation of the calculated value becomes large.

Figure 4.4b shows the plot of $I(U)$ for methane (solid line) and water (dashed line) in PDMS. The profile of $I(U)$ is smooth. Those for all the other polymer/penetrant systems are also smooth, though not shown in the figure. We can expect that the statistical error is very small for these systems. For methane in PDMS, the energy range of $U < -18$ kJ/mol contributes half of $I(U)$. The rest of $I(U)$ arises from the energy ranges of $-18 < U < -8$ kJ/mol, in which the peak in $f(U)$ appears as shown in Figure 4.2a. For water in PDMS, $I(U)$ tends to increase in lower energy region by the Coulombic interaction and the contribution from $U < -20$ kJ/mol amounts to half of $I(U)$. The peak of $f(U)$ contributes to a higher energy region than that of methane since the Lennard-Jones interaction is weaker. Therefore, the energy region of $-10 < U < 0$ kJ/mol, in which $f(U)$ has a peak, makes little contribution to the $I(U)$ of water.

The EVMS method affects $f(U)$ at $U > 10$ kJ/mol; $f(U)$ decreases gradually. Since $I(U)$ has saturated fully in this region, the EVMS method can raise the efficiency of sampling without changing the resultant μ_r value.

4.3.3 Real Molecule Energy Distribution Function

The real molecule energy distribution function $g(U)$ was calculated by the inverse-Widom method. Averages were taken for 10 000 coordinates and for the number of molecules for each system. We calculated $g(U)$ for the small molecules in PDMS and in PE using trajectories generated in Chapter 3. Figure 4.1b shows $g(U)$ in the aqueous ethanol solutions. Figures 4.2b and 4.3b show $g(U)$ in PDMS and in PE, respectively. These figures were obtained from the running average method, as explained for $f(U)$. The distributions in PDMS are broader than in PE. This again arises from the broader distribution of the free volume in PDMS; even the distribution of methane, which has no Coulombic interaction, is broader.

Table 4.2 lists the components of the interaction energy between the test molecule and the host matrix. The Coulombic interaction is dominant for water and ethanol in the aqueous ethanol solutions. On the other hand, the Lennard-Jones interaction is dominant in PDMS, and the Coulombic interaction makes a minor contribution. In PDMS ethanol interacts with PDMS more strongly than water does.

4.3.4 Shing–Gubbins Plot

We calculated μ_r for the aqueous ethanol solutions by the Shing–Gubbins method. Parts a and b of Figure 4.5 show the Shing–Gubbins plots for water and ethanol in the pure liquids and in the 50 wt % aqueous ethanol solution, respectively. The straight lines are the least-squares fits with the slope fixed to $1/kT$. The plots show a high linearity and satisfy the condition of a slope of $1/kT$ in the whole energy region. This indicates that the values of μ_r were calculated with a small statistical error.

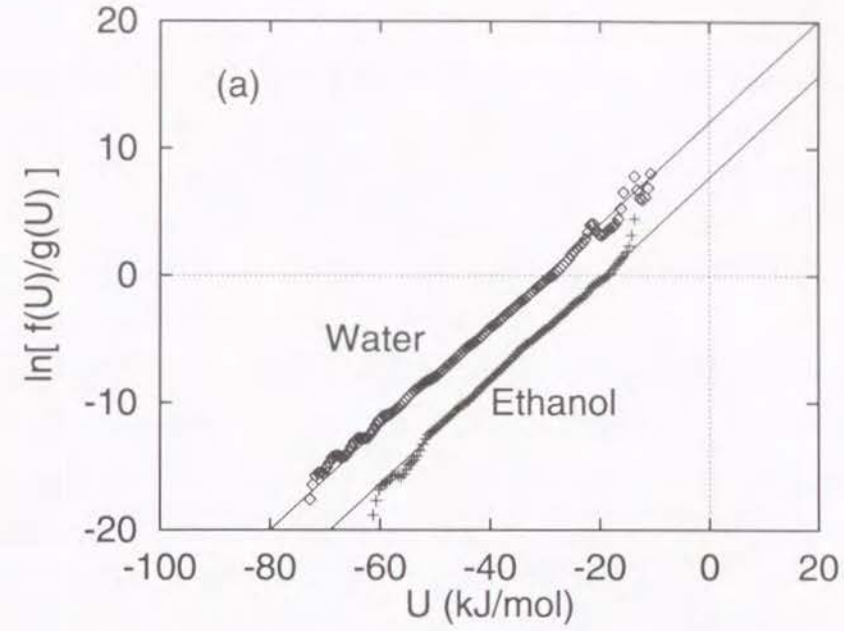

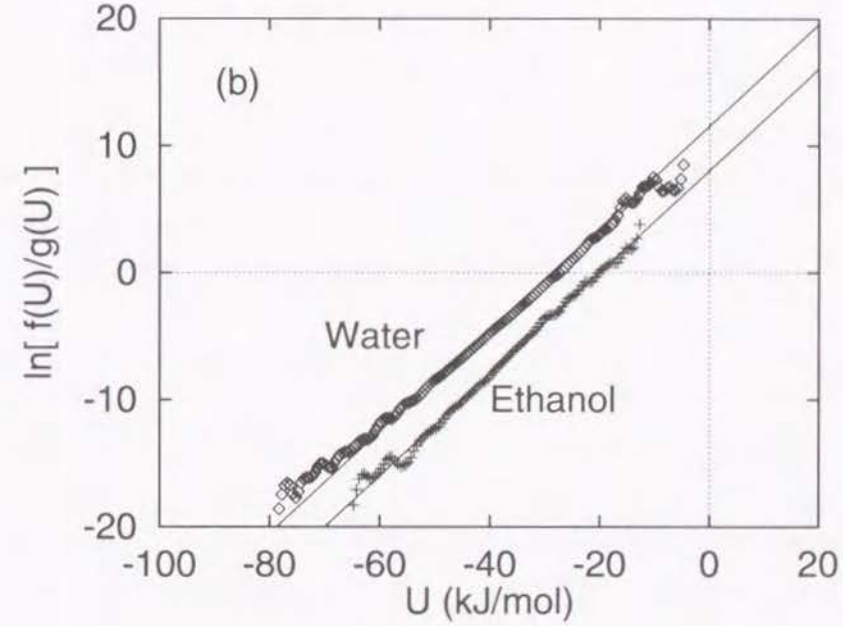

Figure 4.5. Shing–Gubbins plots for water and ethanol (a) in the pure liquids and (b) in the 50 wt % aqueous ethanol solution. The straight lines show the least-squares fits with the slope fixed to $1/kT$. The intersection with the zero-energy axis is equal to $-\mu_r/kT$.

Table 4.2. Average Interaction Energy of Real Molecules in kJ/mol

penetrant	LJ	Coulomb	dihedral	total
		in PDMS		
methane	−16.67			−16.67
water	−9.38	−6.09		−15.47
ethanol	−35.59	−4.61	1.99	−38.20
		in PE		
methane	−20.25			−20.25
water	−10.35			−10.35
ethanol	−39.12		2.12	−37.00
		in Pure Water		
water	17.65	−110.68		−93.03
		in 50 wt % Aqueous Ethanol Solution		
water	15.09	−102.93		−87.84
ethanol	−16.31	−66.47	2.02	−80.76
		in Pure Ethanol		
ethanol	−19.96	−62.51	2.06	−80.41

A Shing–Gubbins plot was made for the small molecules in PDMS and in PE. Straight lines with a slope of $1/kT$ were obtained except for water and ethanol in PDMS, for which $g(U)$ was not accurate enough for evaluation of the chemical potential.

4.3.5 Excess Chemical Potential

The SPC/E potential function was parameterized so as to include the induced dipole moment effectively.[85] Since the dipole moment of the model is larger than the experimental value in vacuum, the interaction energy is overestimated. Therefore, a polarization correction energy of +5.22 kJ/mol,[85] which is the energy needed for a water molecule to polarize, was added to μ_{r} for the system of pure water, by assuming that the induced dipole moment was the same on the average for the N molecules system and the $N+1$ molecules system of a volume V. For water in PDMS, the polarization correction energy is unknown. Because the Coulombic interaction is not dominant in the system, we ignored the polarization correction for this system. The Coulombic interaction energy of water in the 50 wt % solution is not much different from that in pure liquid water, as shown in Table 4.2. Therefore the magnitude of the induced dipole moment in the aqueous solution is assumed to be the same as that in pure water. Thus, the same correction energy was added for water in the aqueous solution. In the OPLS potential, no induced dipole moment effect is included in the parameter fitting. Therefore, we did not take account of this effect for ethanol.

The free energy of the dihedral angle

$$\mu_{\mathrm{DA}} = -kT \ln \int_{-\pi}^{\pi} \exp\left[-V(\phi)/kT\right] \mathrm{d}\phi \tag{4.14}$$

was taken into consideration in the reference state of ethanol, where ϕ is the dihedral angle of ethanol and $V(\phi)$ is the torsional potential energy function described by eq A.4. The excess chemical potential relative to the ideal gas phase, μ_{r}, is obtained by subtracting $\mu_{\mathrm{DA}} = -2.03$ kJ/mol from the calculated value in the simulation.

Table 4.3 lists the excess chemical potentials of water and ethanol in the aqueous ethanol solutions. The chemical potential values were also calculated for the NPT ensemble according to eq 4.2. For the NPT ensemble these agree within 0.03 kJ/mol with those for the NVT ensemble. Since the fluctuation

Table 4.3. Calculated Excess Chemical Potentials in Aqueous Ethanol Solutions Relative to the Ideal Gas Phase

penetrant	μ_r (kJ/mol)		
	0 wt %	50 wt %	100 wt %
	Widom Method[a]		
water	−20.9(2.3)	−23.5(4.0)	
ethanol		−23.5(6.9)	−18.7(4.0)
	Shing–Gubbins Method[b]		
water	−24.9(0.7)	−23.6(1.2)	
ethanol		−18.1(0.2)	−17.2(0.7)

[a] Shown in parentheses are errors which are estimated from 20 subsets of 5 ps each. [b] Shown in parentheses are the differences between the values from least-squares fitting with a slope constrained to $1/kT$ and those from non-constrained fitting.

of the volume is very small in a usual liquid, eq 4.2 has no advantage in this case.

Errors for the Widom method are estimated as standard deviations of 20 separate subsets of 5 ps each. Each subset is composed of 500 configurations. Errors in the Shing–Gubbins method are estimated as the differences between two chemical potential from least-squares fitting with a slope constrained to $1/kT$ and from non-constrained fitting. Comparing the result from the Widom method with that from the Shing–Gubbins method, we find that agreement in the Widom and the Shing–Gubbins methods is excellent for water in the 50 wt % aqueous ethanol solution. For water in pure water and for ethanol in the aqueous solutions, however, agreement is rather poor. In the Widom method, the probability that the ghost molecule forms hydrogen bonds with the matrix molecules is very low. If the hydrogen-bonded configuration is incidentally

sampled, the fluctuation of the calculated value becomes large. On the other hand, stable hydrogen-bonded configurations are almost always sampled in the inverse-Widom method. Since use of both $f(U)$ and $g(U)$ has the benefit of a mutual error cancelation in the Shing–Gubbins method, we can expect that the statistical error is small even for ethanol. This is indeed true, as shown in Table 4.3. Therefore, the chemical potential values from the Shing–Gubbins method are used in the following analysis.

The calculated excess chemical potential of liquid water is slightly lower than the experimental value −23.9 kJ/mol.[58] The excess free energy of mixing of the 50 wt % aqueous ethanol solution was estimated to be a positive value, 0.7 kJ/mol, which agrees reasonably with the experimental value, ~ 0.5 kJ/mol.[59] This shows the adequacy of our simulation.

In our previous paper,[60] we performed MD simulations for pure water (216 molecules) and for pure ethanol (128 molecules) under constant NVT conditions and calculated μ_r by the Widom method. The chemical potentials for water and ethanol were −27.5(5.0) and −8.9(2.8) kJ/mol, respectively (errors are in parentheses). The chemical potential of water is lower than that in the present simulation by 2.6 kJ/mol, and that of ethanol is higher by 8.3 kJ/mol. One reason for the discrepancy is that the "incidentally" sampled low-energy configuration makes a large contribution to the value of μ_r in the Widom method. To overcome this, a Shing–Gubbins plot was also made for the system of the NVT ensemble. The chemical potentials for water and ethanol are −25.5(3.0) and −12.0(2.7) kJ/mol, respectively, which are closer to those of the NPT ensemble by the same method than those by the Widom method. For ethanol, however, the difference is approximately 5 kJ/mol. The density is approximately 4% lower in the NPT ensemble than in the NVT ensemble. This leads to a difference in the average values of the accessible volume fraction for an oxygen atom of ethanol: 0.055 in the NPT ensemble and 0.038 in the NVT ensemble. This is supposed to be one of the origins for the difference in μ_r.

Table 4.4. Calculated Excess Chemical Potentials in Polymers Relative to the Ideal Gas Phase

penetrant	μ_r (kJ/mol)	
	in PDMS	in PE
Widom Method[a]		
methane	−5.84(0.12)	−1.17(0.58)
water	−4.44(0.40)	2.99(0.21)
ethanol	−15.5(1.2)	−6.1(1.5)
Shing–Gubbins Method[b]		
methane	−5.3(0.5)	−1.0(1.3)
water		2.9(2.8)
ethanol		−6.0(1.4)

[a] Shown in parentheses are errors which are estimated from 10 subsets of 50 ps each. [b] See footnote *b* of Table 4.3.

Table 4.4 lists μ_r of the small molecules in the polymers. The error was estimated in the same way as in the case of aqueous ethanol solutions; all of the configurations are separated into 10 subsets each of which consists of 100 configurations corresponding to a 50 ps trajectory. The values of μ_r from the Widom method agree well with those from the Shing–Gubbins method. For the systems of water and ethanol in PDMS, the Shing–Gubbins plots were not linear. The small molecules diffuse by the jump process in the polymers; the vibrational motion in a cage is dominant for most of the simulation time. It is difficult to sample all the configurational space during the simulation time. Therefore, $g(U)$ is liable to have some statistical errors. On the other hand, the Widom method does not suffer from such a problem. Since the Lennard-Jones interaction is dominant in PDMS and PE, the errors which are caused mainly by the strong Coulombic interaction are expected to be very low. The

estimated errors in Table 4.4 support this conjecture. Therefore, we use the μ_r from the Widom method for the small molecules in the polymers.

The chemical potentials are always lower in PDMS than in PE. This is due to the broader free volume distribution in PDMS. The ethanol molecule is larger in size but has a lower μ_r than water or methane because the Lennard-Jones interaction is stronger.

4.3.6 Solubility of Penetrant in Polymer

The solubilities, S_g and S_l, were calculated from eqs 4.10 and 4.11, respectively, and are listed in Table 4.5 and Table 4.6. The solubility of methane in PDMS is higher than the experimental value 0.56[15] but is close to the calculated value 12.5 which Sok et al.[15] evaluated by the Widom method. Since the standard deviation is very small, the discrepancy with the experimental value is probably due to inaccuracy of the potential functions. The solubilities, S_l, of ethanol are approximately 760 and 350 times higher in PDMS and PE, respectively, than those of water. Although the insertion probability of ethanol in PDMS is smaller than that of water, the solubility of ethanol is higher than that of water because the Lennard-Jones interaction of ethanol is stronger. The solubilities, S_g, of methane, water, and ethanol in PDMS are approximately 7, 20, and 42 times higher, respectively, than those in PE. This is due to the broader free volume distribution in PDMS. For a large molecule such as ethanol, the difference in solubility is significant.

Okamoto et al.[47] measured the solubilities of the aqueous solution of ethanol at various concentrations by sorption experiments. Water has a low solubility in the PDMS membrane, and there are no experimental data for pure liquid water. The solubility extrapolated to zero concentration is smaller than 1×10^{-3}. The calculated solubility, 2.76×10^{-4}, agrees reasonably well with the experiment. The solubility of liquid ethanol, 0.50, is higher than the experimental value, 0.092. The solubilities at infinite dilution were calculated in this simulation. Considering the fact that the discrepancy from Henry's law

Table 4.5. Calculated Solubilities and Permeation Rates of gases[a]

penetrant	polymer	S_g	D (cm^2/s)	P_g (cm^2/s)
methane	PDMS	10.4 (0.5)	0.57×10^{-5}	5.9×10^{-5}
water	PDMS	5.9 (1.0)	1.53×10^{-5}	9.1×10^{-5}
ethanol	PDMS	490 (250)	0.20×10^{-5}	9.8×10^{-4}
methane	PE	1.60 (0.38)	0.16×10^{-5}	2.6×10^{-6}
water	PE	0.302 (0.025)	0.78×10^{-5}	2.4×10^{-6}
ethanol	PE	11.6 (7.2)	0.07×10^{-5}	8.1×10^{-6}

[a] Errors are in parentheses.

Table 4.6. Calculated Solubilities of liquids[a]

penetrant	polymer	S_l		
		0 wt %	50 wt %	100 wt %
water	PDMS	$2.76(0.82) \times 10^{-4}$	$4.6(2.3) \times 10^{-4}$	
ethanol	PDMS		$3.5(1.8) \times 10^{-1}$	$5.0(2.6) \times 10^{-1}$
water	PE	$1.40(0.42) \times 10^{-5}$	$2.3(1.2) \times 10^{-5}$	
ethanol	PE		$8.3(5.1) \times 10^{-3}$	$11.8(7.3) \times 10^{-3}$

[a] Errors are in parentheses.

becomes larger for a penetrant with high solubility, the agreement between the calculated and experimental values is satisfactory.

4.3.7 Permeation Rate

In Chapter 3, the diffusion coefficients D were determined for small molecules in polymers. The diffusion coefficients for methane, water, and ethanol in PDMS and PE are listed again in Table 4.5. Ethanol, which is larger in size than water, has a smaller diffusion coefficient in polymers than water. The

Table 4.7. Calculated Permeation Rates of liquids[a]

penetrant	polymer	P_l (cm^2/s)		
		0 wt %	50 wt %	100 wt %
water	PDMS	4.2×10^{-9}	7.0×10^{-9}	
ethanol	PDMS		7.0×10^{-7}	10.0×10^{-7}
water	PE	1.1×10^{-10}	1.8×10^{-10}	
ethanol	PE		5.8×10^{-9}	8.3×10^{-9}

[a] Errors are in parentheses.

permeation rate is calculated from the product of the diffusion coefficient and the solubility. The permeation rates of gases (P_g) and liquids (P_l) are listed in Table 4.5 and Table 4.7, respectively.

Considering the accuracy of simulations and experiment, our calculated values agree with the experimental values: 1.1×10^{-5}, $< 1 \times 10^{-8}$, and 4.1×10^{-7} cm^2/s for methane gas, pure liquid water, and pure liquid ethanol in PDMS at 300 K.[47, 48] The agreement between the simulation and the experiments is better than in our previous paper.[60] This is probably due to the use of the Shing–Gubbins method for the calculation of the excess chemical potentials in the liquids. The result that the permeation rate of ethanol is higher than water agrees with the permselectivity of ethanol by the PDMS membrane. Ethanol has a smaller diffusion coefficient than water in PDMS but has a much larger permeation rate. This is a consequence of the difference in solubility between water and ethanol.

4.3.8 Energy Map of Ghost Molecule

A three-dimensional energy map of the ghost molecule was generated to examine where the effective sampling points are distributed in the unit cell. Considering $100 \times 100 \times 100$ grid points in the unit cell of PDMS, all the grid

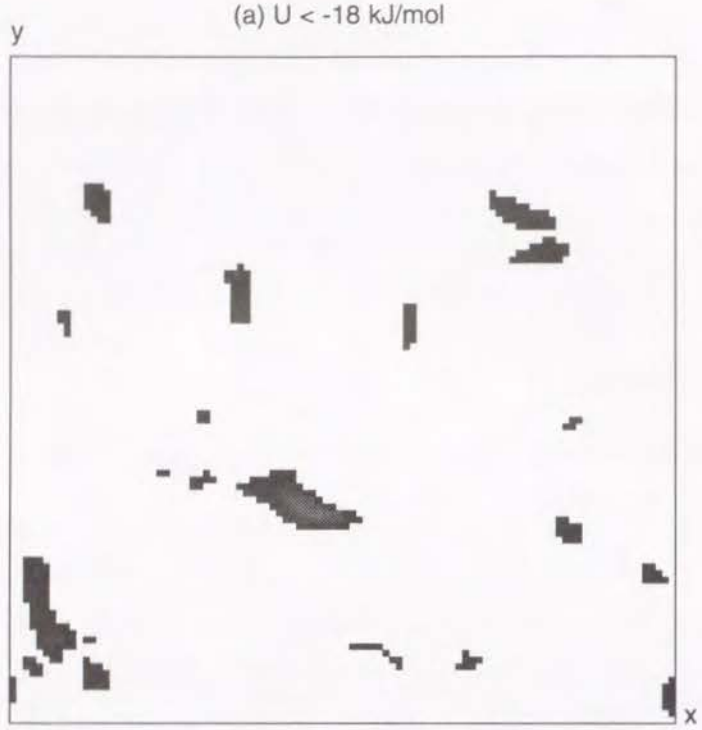

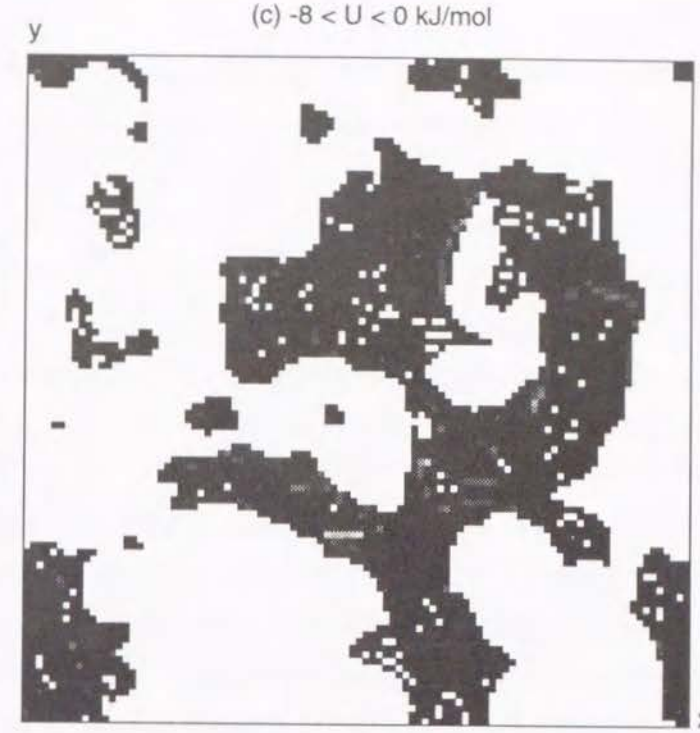

Figure 4.6. The x–y projections of the clusters of grid points at which a methane molecule interacts with the surrounding matrix of PDMS in the energy ranges (a) $U <$ −18, (b) $-18 < U < -8$, and (c) $-8 < U < 0$ kJ/mol.

points were classified by the interaction energy U between a methane molecule on the grid point and the host matrix.

The cluster analysis was performed for grid points which belong to the same class, using the method described in Chapter 2. Parts a–c of Figure 4.6 show the projection of the clusters with $U < -18$, $-18 < U < -8$, and $-8 < U < 0$ kJ/mol, respectively. Table 4.8 lists the results of the cluster analysis. Figure 4.6a shows the low energy regions at which U is less than −18 kJ/mol. The regions are surrounded by the clusters of $-18 < U < -8$ kJ/mol, which are shown in Figure 4.6b. The lower energy regions are not restricted to a small area but rather are scattered uniformly. The clusters move ubiquitously in the cell as time evolves. Therefore, the points where the low energy configurations are sampled are randomly distributed in the unit

Table 4.8. Cluster Analysis of Energy Map for Methane in PDMS

U (kJ/mol)	$f_v \times 10^4$	$\langle V_c \rangle$ (Å^3)	$\langle s^2 \rangle^{1/2}$ (Å)	$\langle b/s^2 \rangle$
$U < -18$	13.5	3.55	0.98	0.523
$-18 < U < -8$	203.5	186.97	6.78	0.575
$-8 < U < 0$	87.4	4.72	1.96	0.616

cell. Referring to Figure 4.4, these regions contribute half to $I(U)$, in spite of the small volume.

Figure 4.6b shows the region $-18 < U < -8$ kJ/mol, which contributes to the peak in $f(U)$ of methane in PDMS, as shown in Figure 4.2a. The size and position of the clusters correspond to the free volume clusters in Figure 2.7a. Comparing Table 2.3 with Table 4.8 shows that each item of the clusters of the energy map for $-18 < U < -8$ kJ/mol agrees well with that of the free volume in PDMS (the former is slightly larger). Therefore, the peak in $f(U)$ is attributed to the insertion trials into the large free volume. The radius of water, 1.5828 Å, is approximately 85% of that of methane (1.865 Å). Many effective samplings were made for the regions which are accessible for a probe with a radius of 85% of the molecular radius. When the excluded volume map is generated in the EVMS method, the Lennard-Jones size parameters of both a matrix atom and a test atom are scaled by the factor a in eq 4.3. Therefore the white background in Figure 2.7a corresponds to the excluded volume map of methane with a scale factor of $a = 0.92$.

Figure 4.6c shows the energy region of $-8 < U < 0$ kJ/mol. The clusters are spread widely in the entire cell. The dark black grid points show that the depths of all the clusters are small. By comparison of each item in Table 4.8, f_v is 43% of that of $-18 < U < -8$ kJ/mol. Nevertheless, $\langle V_c \rangle$ is only 2.5%. The region $-8 < U < 0$ kJ/mol in Figure 4.6c surrounds the region $-18 < U < -8$ kJ/mol in Figure 4.6b. The former region, however, makes little contribution

to $I(U)$, as shown in Figure 4.4.

4.4 Conclusion

The excess chemical potentials μ_r of methane, water, and ethanol in PDMS and PE were calculated by the Widom method. The excess chemical potentials of water and ethanol in the aqueous ethanol solutions (0, 50, 100 wt %) were also calculated by the Shing–Gubbins method. The solubilities of the small molecules in the polymers were calculated from the values of μ_r.

PDMS and PE are hydrophobic polymers. The solubility of ethanol is much higher than that of water in PDMS and PE. This is owing to the Lennard-Jones interaction between ethanol and the polymers. The free volume analysis shows that PDMS has larger free volume clusters than the other systems. PDMS has a structure in which a large molecule is soluble.

The permeation rates, which were calculated from the diffusion coefficients and the solubilities, were in reasonable agreement with experimental data. Although ethanol has a smaller diffusion coefficient than water, ethanol has a larger permeation rate. This is because ethanol has a higher solubility in PDMS. This character explains the ethanol selectivity of the PDMS membrane.

Part II

Permeation into Hydrophilic Membranes

Chapter 5

Hydrogen-bonded Structure in Hydrogels

5.1 Introduction

Water molecules are highly influenced in the presence of polymer chains. Terada et al.[61] evaluated the number of hydrogen-bond defects caused by a monomer unit of polymers by measuring the relative intensities of collective bands in the Raman spectroscopy. The numbers of defects of water in hydrophilic polymer solutions are greater than those in hydrophobic polymer solutions. Maeda et al.[62] evaluated the dependence of the number of defects on the molecular weights and the degrees of cross-links of polymers. They found that the numbers of defects increase with increasing the molecular weights and the degrees of cross-links. They argued that the number of defects increases when the size of the cluster of *interstitial water* surrounded by polymer networks decreases below a critical size and the orientation of water molecules is restricted.

Poly(vinyl alcohol) (PVA) is miscible with water at high temperature but is insoluble at low temperature. On the other hand, poly(vinyl methylether) (PVME) and poly(N-isopropyl acrylamide) (PNiPAM) are soluble in water at low temperature but are not soluble and phase separations are observed at high temperature: PVME and PNiPAM have LCST. The difference in solubility arises necessarily from a difference in the interaction between water and polymers. Ohta et al.[63] measured the mobility of water molecules in the PNiPAM solution around the volume phase transition temperature, by the spin–spin relaxation time T_2 in NMR. In the pure water, T_2 increases linearly with temperature. Though T_2 in the PNiPAM solution increases with tem-

perature in most the temperature range, it decreases discontinuously at the phase transition temperature, at which the mobility of water molecules is significantly depressed. It is generally accepted that the volume phase transition phenomenon has a close relation to the change of the entropy of water caused by the hydrophobic effect.

In this chapter, we have performed MD simulations for the hydrogel models of PVA, PVME, and PNiPAM to elucidate the interaction between water and polymers. Simulations are performed for the hydrogel models with various water contents under several temperature conditions. Structure and distribution of hydrogen-bonds are analyzed to examine the effect of polymers on the hydrogen-bond networks.

5.2 Model and Simulation Details

5.2.1 Model and Potential Functions

The primary structures of PVA, PVME, and PNiPAM are shown in Figure 5.1. Polymer samples of water contents 0, 25, 50, and 75 wt % are generated and used for hydrogel models. Table 5.1 lists the water content c_w, the degree of polymerization x, and the number of water molecules n_w of the systems simulated. The tacticity of all the main chains is set to be atactic. Sequences of monomer units of d- and l-structures are generated randomly with constraining the fraction of meso diads to 0.5.

The AMBER/OPLS force field is used for the polymers, and the SPC/E for water. The united atom approximation is applied for $-CH_3$, $-CH_2-$, and $-CH-$ groups, each of which is treated as a single interaction site. A detailed description of the potential functions is given in Appendix A. Calculations are performed on NEC SX-3 and CRAY Y-MP2E supercomputers and HP-9000 700-series workstations, using the molecular simulation program PAMPS we coded.

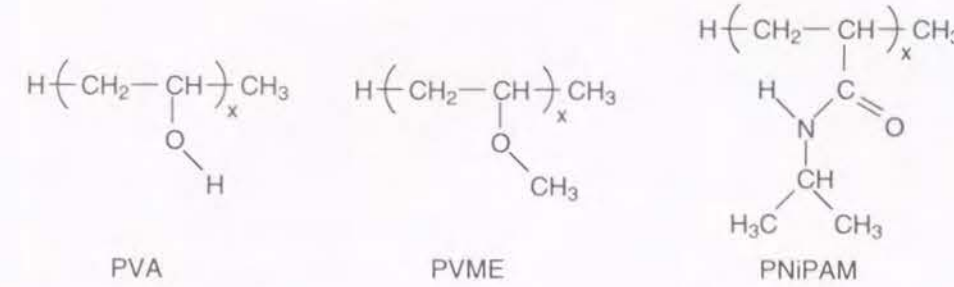

Figure 5.1. Structures of poly(vinyl alcohol) (PVA), poly(vinyl methylether) (PVME), and poly(N-isopropyl acrylamide) (PNiPAM).

5.2.2 Generation of Initial Structures

Using the modified self-avoiding random walk method (see Appendix C), a single polymer chain is confined in a unit cell under the periodic boundary condition at the density of 0.01 g/cm^3. After the steepest-descent energy minimization, MD simulations are performed under the constant NVE ensemble.

If the Coulomb potentials are calculated using the dielectric constant in vacuum for eq A.7, polymer chains cohere at low density condition since the pair potentials are too strong. To incorporate the screening effect on the Coulomb potential by water molecules, the distance dependent dielectric constant (see Appendix B) is used instead of that in vacuum. The cutoff length, r_{sw} and r_{cut} of eq B.1, is 8 and 9 Å respectively. Although the Coulomb potentials are cut off at 9 Å on this stage, all the long-range Coulomb interactions are considered by the Ewald sum method in the later stages, not using the switching function.

A simulation of 10 000 steps is performed with scaling velocities of atoms at regular intervals to keep the temperature to 300 K. The equations of motion are solved by the Verlet algorithm[26] with a time step of 0.5 fs. The bond angles, H–O–H of water and CH–O–H of PVA, and all the bond lengths are constrained by the SHAKE algorithm. The chains cannot interact with the image chains at this density. Then, the unit cell is compressed to a density of 0.1 g/cm^3. After

Table 5.1. Samples of Hydrogels

Polymer	x	n_w	c_w (wt%)
	$c_w \simeq 0$ wt%		
PVA	161	5	0.25
	$c_w \simeq 25$ wt%		
PVA	161	150	27.54
PNiPAM	81	150	22.74
	$c_w \simeq 50$ wt%		
PVA	81	199	50.00
PVME	81	199	43.16
PNiPAM	41	199	43.50
	$c_w \simeq 75$ wt%		
PVA	21	215	79.72
PVME	21	215	74.96
PNiPAM	11	215	75.44

The values x, n_w, and c_w are degree of polymerization, number of water molecules in a unit cell, and water content, respectively.

the steepest-descent energy minimization, a MD simulation of 10 000 steps is performed. A further simulation is performed for 10 000 steps, compressing the unit cell towards a density of 0.25 g/cm^3 step by step. An equilibration run of 50 000 steps is performed at the fixed density. The alternate compression and equilibration runs produce the equilibrium structures of the densities of 0.25, 0.5, 0.75, 1.0, 1.25 g/cm^3.

An initial structure of the hydrogel model is obtained by inserting the

prescribed number of water molecules into the structure of an appropriate density. For example, 150 water molecules and a polymer structure of PNiPAM ($x = 81$) with a density of 0.75 g/cm^3 produce an initial structure of the PNiPAM hydrogel model with water content 25 wt %. The initial structures for the systems with water contents 0, 25, and 50 wt % are obtained by the method described above. Those for the systems with a water content 75 wt % are obtained, however, by another method since degrees of polymerization are low and there is few entanglement of main chains. A polymer chain and 215 water molecules are confined directly in a unit cell under the periodic boundary condition at the density of 1.0 g/cm^3.

5.2.3 MD Simulation

After the steepest-descent energy minimization, MD simulations are performed at 5 temperatures (400, 350, 300, 250, 200 K). The sampling is made for a period of 50 ps (100 000 steps) at each temperature, writing out coordinates and velocities of atoms with 20 steps interval to disk files for later analyses. The sampling is made after equilibration runs of 120 000 steps (60 ps) at 400 K. The last configuration sampled at 400 K is used for an initial structure of MD runs at 350 K, and the last configuration at 350 K for an initial structure at 300 K, and so on. The profile of temperature is shown in Figure 5.2. Between two sampling runs, an equilibration run is performed for 30 000–90 000 steps (15–45 ps), which are longer at low temperature. During the sampling periods, the temperature and density of systems are fluctuating around average values, not shifting systematically.

MD simulations of the first 70 000 steps at 400 K are performed under the constant NVE ensemble, and the subsequent simulations under the constant NPT ensemble by Nosé–Andersen method with a constant pressure of 0.1 MPa ($\simeq$ 1 atm). The Long-range Coulombic interactions are handled by the Ewald sum method. The short-range Lennard-Jones terms of the potentials are cut off at 9 Å, and the long-range correction terms are added.[57] The other

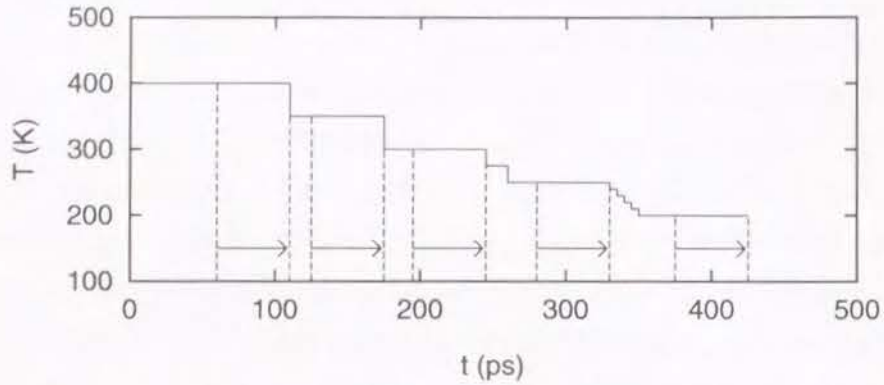

Figure 5.2. Temperature profile of MD simulation of hydrogel model systems. Arrows in the figure indicate sampling periods and the remaining parts is devoted to equilibration.

conditions, the bond length and angle constrain and the time step, are the same as in the generation phase of initial structures.

Simulations for pure water (216 molecules in a unit cell) are also performed by the same method. MD simulations are also performed for the system of PVA with a water content approximately 0 wt % (0.25 wt %). After simulations are performed for pure PVA without water with stepwise lowering of temperature by a similar way to those for hydrogel models, five water molecules are inserted in the equilibrium structure at 300 K. MD simulations of 500 000 steps (250 ps) are sampled after equilibration runs.

5.2.4 Definition of Hydrogen-bonds

Two water molecules are defined to be hydrogen-bonded if distances and an angle between two molecules satisfy

$$\begin{aligned} R_{\mathrm{OO}} &\leq 3.60\text{Å} \\ R_{\mathrm{OH}} &\leq 2.45\text{Å} \\ \phi &\leq 30^{\circ} \end{aligned} \tag{5.1}$$

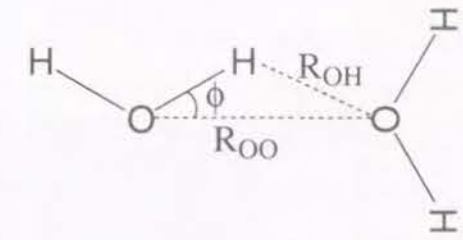

Figure 5.3. Definition of hydrogen-bonds.

where R_{OO} and R_{OH} are distances $\mathrm{O}_1 \cdots \mathrm{O}_2$ and $\mathrm{O}_1 \cdots \mathrm{H}_2$, ϕ is an angle $\mathrm{O}_1 \cdots \mathrm{O}_2$—$\mathrm{H}_2$, where the subscripts 1 and 2 show indices of water molecules. A schematic expression is shown in Figure 5.3. This is the same definition as Luzar and Chandler.[64] They demonstrated that the number of hydrogen-bonds by this definition is almost the same as that by another definition based on the pair potential energy with an appropriate threshold. The hydrophilic groups of the polymers also form hydrogen-bonds to water. The hydrogen-bonds are defined also for –OH of PVA and >NH of PNiPAM in the same manner. The groups –O– of PVME and =O of PNiPAM are assumed to form the hydrogen-bonds with water as a proton acceptor.

5.3 Results and Discussion

5.3.1 Structures

Figure 5.4 shows the final structures of hydrogel models with water contents 25, 50, and 75 wt % at 300 K. Polymer chains are drawn by the ball-and-stick model, and water molecules by the wireframe model. The cell sizes in the figure are proportional to real cell lengths: approximately 19.6–26.3 Å. For the systems of $c_{\mathrm{w}} \simeq 25$ and 50 wt %, polymer chains are entangled with themselves and also with image chains. Especially for PVA, numbers of polymer–polymer hydrogen-bonds are formed and the network structure is constructed by the hydrogen-bonds.

For the system of $c_{\mathrm{w}} \simeq 75$ wt %, the degrees of polymerization are 21

or 11, which are rather small. The end-to-end distances of the chains are approximately the same order as the unit cell lengths. Though few entanglements are observed, the chains are capable of interacting with the image chains; intermolecular hydrogen-bonds are formed for PVA and PNiPAM.

Although no chemical cross-links are introduced in the present hydrogel models, a complicated network structure is formed by intra- and intermolecular hydrogen-bonds for PVA and PNiPAM hydrogel models. Furthermore, the systems are constrained to some extent by imposing the cubic periodicity because the cell shape is fixed and the cell lengths are scaled uniformly. Therefore, we expect that the influence of cross-links are incorporated effectively on all the properties which are determined by local structures and short time scale motions.

5.3.2 Densities

The densities are fluctuating around average values, not shifting systematically. Figure 5.5 shows the temperature dependences of the average densities. For the hydrogel models, the densities are higher than those for pure water. PVME and PNiPAM models have almost the same densities, and PVA models have higher densities. The densities are higher for the systems with lower water contents. The dependence on water contents is smaller for PVME and PNiPAM but is rather distinct for PVA. One of the reason is that polymer–polymer hydrogen-bonds of PVA are supposed to be more tight than those of PVME and PNiPAM. Distribution and tightness of hydrogen-bonds are examined below.

The temperature dependences of densities are varied with the water contents for PVME and PNiPAM but are not for PVA. For the systems with a high water content (75 wt %), the temperature dependences are distinct for PVME and PNiPAM; the densities decrease remarkably at high temperature. Since there is no way to hold water molecules at high temperature by destruction of polymer–water hydrogen-bonds, a behavior like the phase separation

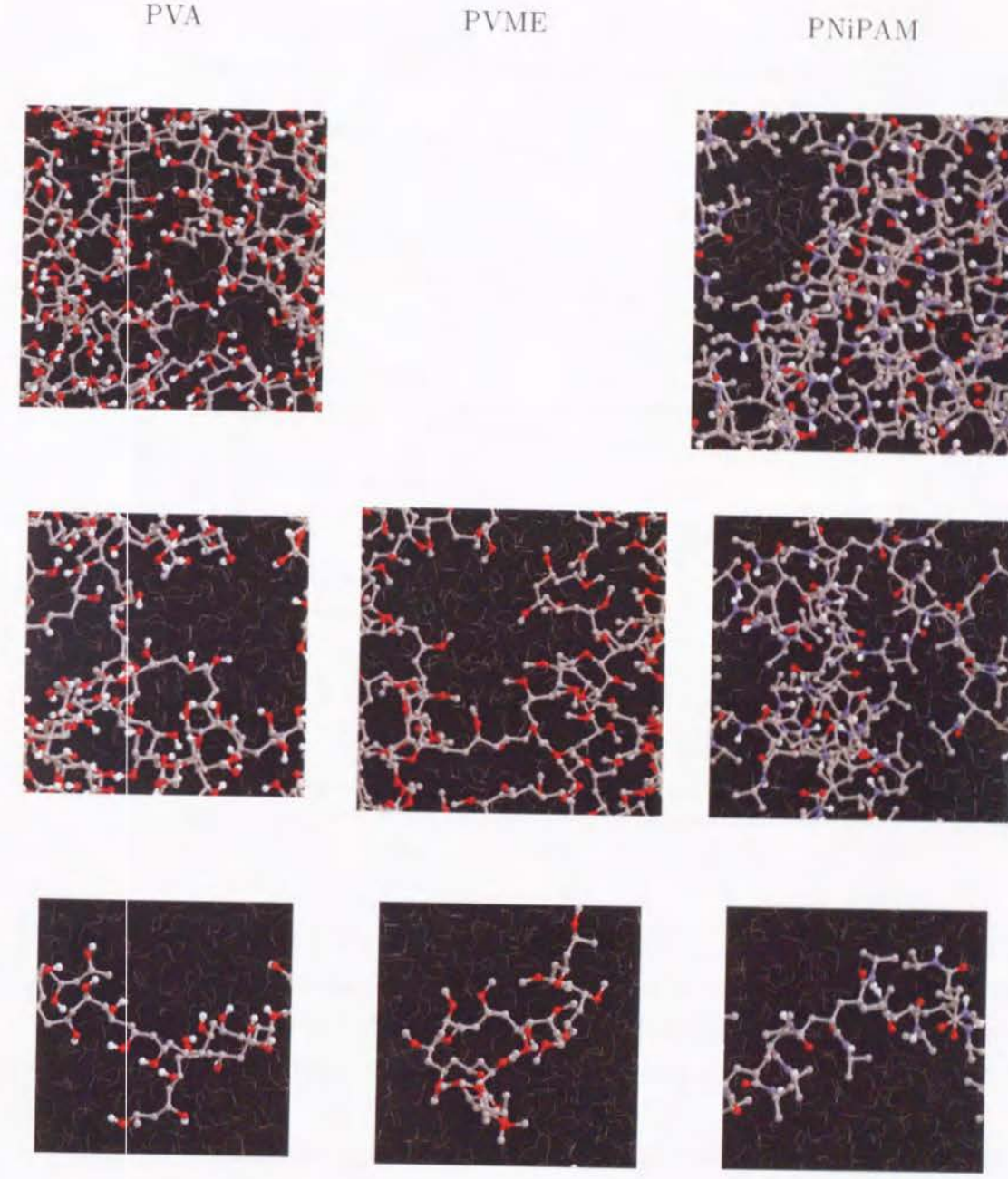

Figure 5.4. Snap shots of final structures of PVA, PVME, and PNiPAM hydrogel models at 300 K. Water contents are 25, 50, and 75 wt % for upper to lower snap shots. Polymer chains are drawn by the ball-and-stick model: (gray) united atom carbon, (red) oxygen, (light blue) nitrogen, (white) hydrogen. Water molecules are drawn by the wireframe model.

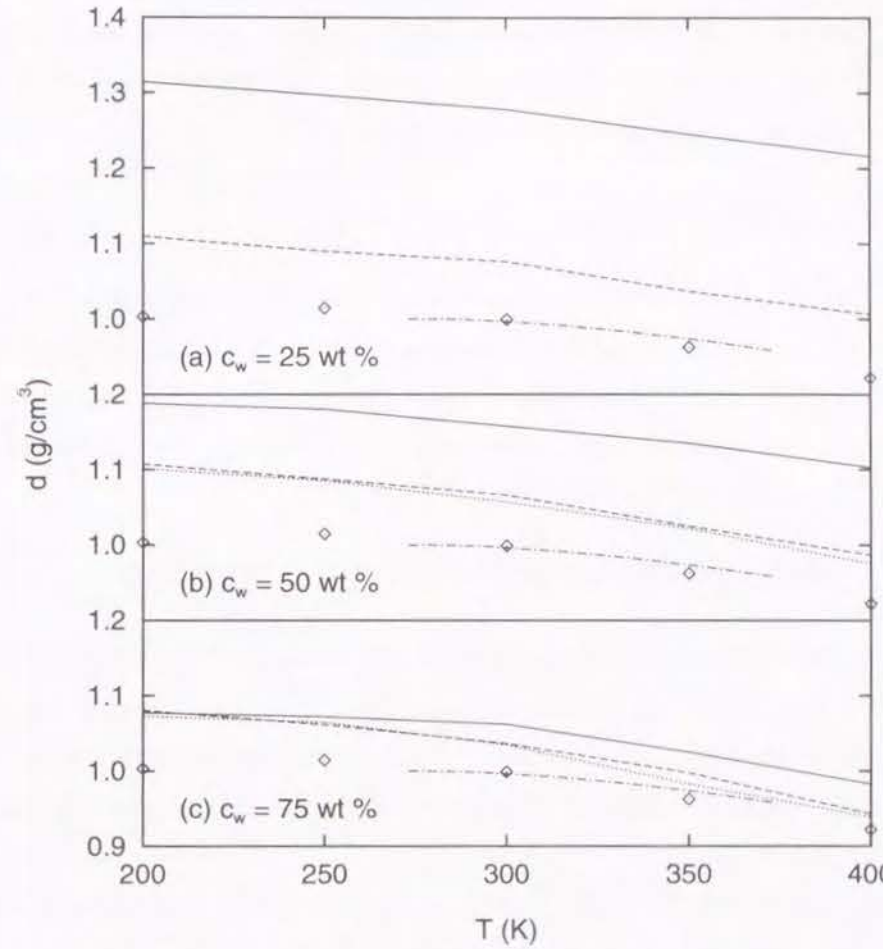

Figure 5.5. Temperature dependence of the densities calculated for the hydrogel models with water contents (a) 25, (b) 50, and (c) 75 wt % and also for pure water: (solid line) PVA, (dotted line) PVME, (dashed line) PNiPAM, (dash-dot line) experimental values of pure water, (diamond) calculated values of pure water.

occurs for PVME and PNiPAM. For the systems with lower water contents, entanglements of polymer chains may diminish sharpness of the transition observed in our simulation for $c_w \simeq 75$ wt %, where a polymer chain is too short to entangle.

The calculated densities for pure water agree well with the experimental values.[37] The value for the PVA model with $c_w \simeq 0$ is 1.274 g/cm^3, which agrees

well with the experimental values 1.27–1.31 g/cm^3. The densities for PVA hydrogel models with water molecules are distributed between those for pure water and those for pure PVA. Correct densities are presumably reproduced by the simulation at intermediate water content.

5.3.3 Radial Distribution Function

The radial distribution function $g(r)$ between water oxygen and functional groups of polymers are calculated. Those are shown in Figures 5.6a and 5.6b, where hydrophilic and hydrophobic groups are chosen as a polymer site. The results are for the systems with a water content 50 wt % at 300 K. The heights of the first peaks follow the order of

$$\mathrm{O(PVA)} > \mathrm{O(PNiPAM)} > \mathrm{O(PVME)} \simeq \mathrm{N(PNiPAM)}$$

PVA is the most hydrophilic among three polymers, and PVME is the least. For PVME and PNiPAM, large peaks are found in $g(r)$ around the $-CH_3$ groups, which are exposed into water. With increasing the temperature, the heights of the peaks become lower and the positions of the peaks shift slightly toward the longer distance.

Regarding the region in the first peaks of $g(r)$ as the first hydration shell, the coordination number of water molecules

$$n_{\mathrm{cd}} = 4\pi\rho \int_0^{r_{\mathrm{cd}}} g(r) r^2 \mathrm{d}r \tag{5.2}$$

are calculated for polar groups of polymers, where ρ is the number density of water and r_{cd} is the location of the first minimum in $g(r)$. Since the temperature dependence of r_{cd} is very small, we used an fixed r_{cd} value averaged over five temperatures. The values of r_{cd} are 3.3 and 3.4 Å for oxygen and nitrogen atoms, respectively.

As listed in Table 5.2, the coordination numbers are approximately 2.2 for O (PVA), and 1 for O (PVME) and N (PNiPAM) for the systems with $c_{\mathrm{w}} \simeq 75$ wt % at 300 K. An intermediate value of these two numbers, approximately

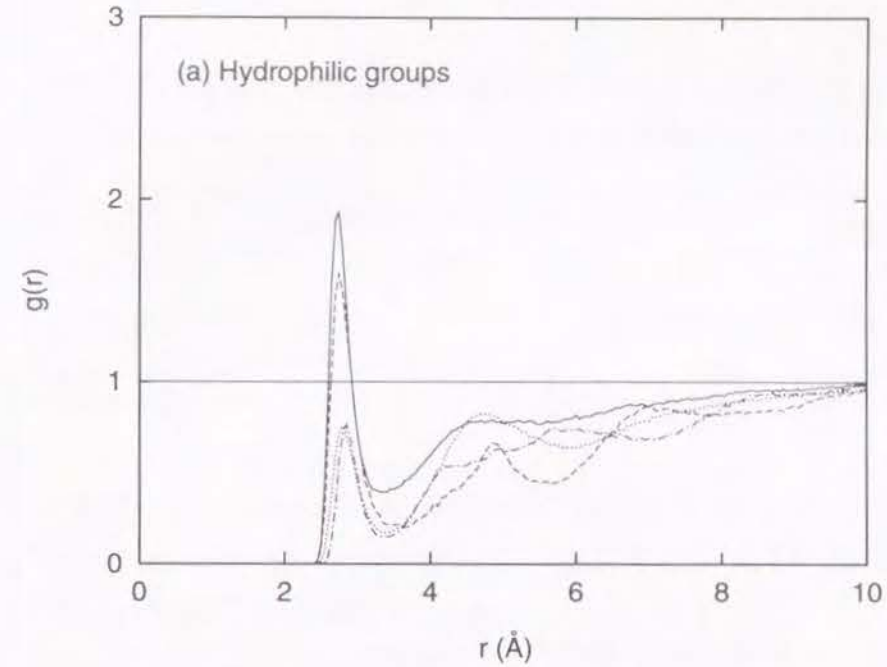

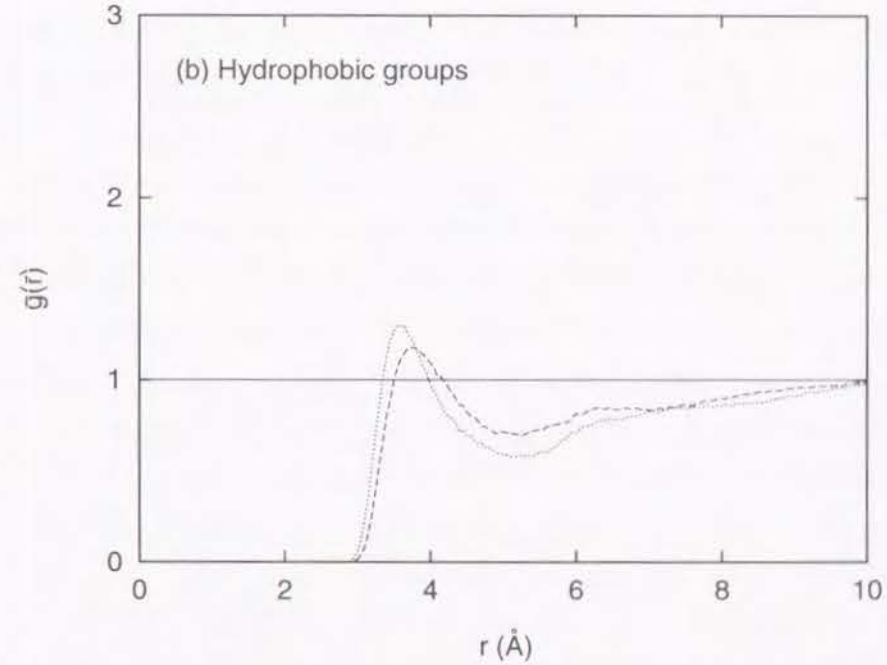

Figure 5.6. Radial distribution function $g(r)$ at 300 K (a) for O(water)–O(polymer) and O(water)–N(polymer) and (b) for O(water)–CH_3(polymer): (solid line) O of PVA, (dotted line) O and CH_3 of PVME, (dashed line) O and CH_3 of PNiPAM, (dash-dot line) N of PNiPAM.

Table 5.2. Coordination Number of Water around Hydrophilic Groups of Polymers at 300 K

c_w	O (PVA)	O (PVME)	O (PNiPAM)	N (PNiPAM)
25 wt %	1.239		0.821	0.490
50 wt %	1.526	0.536	1.042	0.510
75 wt %	2.209	1.046	1.797	0.984

1.8, is observed for O (PNiPAM). The coordination numbers decrease at higher temperature and for the systems with smaller water contents.

5.3.4 Classification of Water Molecules

water molecules are classified into three categories: (1) those around hydrophilic groups, (2) those around hydrophobic groups, and (3) the bulk region. The region 1 is defined so as to cover the inner region up to the first peaks of $g(r)$ of water oxygen atoms around hydrophilic groups: –OH, –O–, and –CONH–. The region 2 is similarly defined for hydrophobic groups: >CH–, $-CH_2-$, and $-CH_3$. The regions which belong to both the region 1 and 2 are incorporated in the region 1. The region 3 (bulk region) is defined as a region outside the region 1 and 2. The other classification method based on the mass center of water makes no difference. Table 5.3 lists the center atom species of the region 1 and 2, and radii of the regions around the atoms.

Table 5.4 lists the average number of water molecules contained in each region. The values are averaged over five temperatures from 200 to 400 K. The numbers of water molecules in the region 1 follow the order of

$$(\mathrm{PVA}) > (\mathrm{PNiPAM}) > (\mathrm{PVME})$$

and those in the region 2 the order of

$$(\mathrm{PVME}) > (\mathrm{PNiPAM}) > (\mathrm{PVA})$$

Table 5.3. Classification of Water Molecules[a]

atom[b]	polymer	radius (Å)
	Region 1 (hydrophilic)	
O	PVA, PVME, PNiPAM	3.30
H (OH)	PVA	2.45
H (NH)	PNiPAM	2.60
N	PNiPAM	3.40
C (CO)	PNiPAM	4.40
	Region 2 (hydrophobic)	
CH	PVA, PVME	4.10
CH	PNiPAM	4.50
CH_2	PVA, PVME, PNiPAM	4.50
CH_3	PVA, PVME, PNiPAM	4.50

[a]Space around hydrophilic and hydrophobic atoms of polymers are defined as the region 1 and 2, respectively. Each space covers the region inside the first peak of the polymer–water radial distribution function. [b]Center atom of each region.

The orders can be accounted for from the fact that PVA is more hydrophilic and PVME is less hydrophilic. The numbers in the region 3 follow the order of

$$(\mathrm{PVA}) > (\mathrm{PNiPAM}) \simeq (\mathrm{PVME})$$

Since the radius from the center atom is large for the hydrophobic region, the number of water molecules in the bulk region is small for PVME and PNiPAM, which have large hydrophobic side groups. The numbers in the region 3 are very small for the systems with $c_w \simeq 25$ wt %. In this water content, almost all the water molecules are highly perturbed by polymers. Most of water molecules belong to the region 1 for PVA, while the numbers in the region 1

Table 5.4. Number of Water Molecules in Three Classified Regions[a]

Polymer	Region 1	Region 2	Region 3
	$c_w \simeq 25$ wt %		
PVA	111.0	24.2	14.8
PNiPAM	71.4	69.5	9.1
	$c_w \simeq 50$ wt %		
PVA	87.4	43.4	68.2
PVME	38.5	113.0	47.5
PNiPAM	50.3	94.7	54.0
	$c_w \simeq 75$ wt %		
PVA	39.9	31.1	144.0
PVME	18.7	97.1	99.2
PNiPAM	29.8	76.3	108.9

[a] Average values over five temperatures from 200 K to 400 K.

and 2 are almost same for PNiPAM.

As for temperature dependence, the numbers decrease in the region 1 and 2 and increase in the region 3 as increasing temperature. The water molecules are extracted from the hydration shell into the bulk region at higher temperature.

5.3.5 Residence Rate of Water

The water molecules diffuse from one region to another with the passage of time. The residence rate, $P_{res}(t)$, is defined as the probability that the water molecule which exists in one region at time t_0 stays in the same region at later time $t + t_0$, not departing from the region. The volumes of the region

1 are almost the same for –OH, –O–, =O, and >NH, as shown in Table 5.3. Figures 5.7a, 5.7b, and 5.7c show $P_{res}(t)$ at 300 K for the regions 1, 2, and 3, respectively.

In the region 1 (hydrophilic), the decay curves of $P_{res}(t)$ have long tails for PVA and PNiPAM. This is because the hydrogen-bonds between water and polymers bind the water molecules to the region for a long time. Although the partial charges are the same for –O– and =O as shown in Table A.8, $P_{res}(t)$ of =O resides for a longer time than that of –O–. Irrespective of the larger partial charge for –OH than >NH, $P_{res}(t)$ of >NH resides for a longer time than that of –OH. The reason for these observations is that the groups =O and >NH of PNiPAM are located in a somewhat isolated space from the bulk solvent; water molecules around the groups are hard to leave the area. Since the region around –CONH–, which includes those around both =O and >NH, is a combined wide space for water molecules to move around, $P_{res}(t)$ resides for a very long time period despite the number of water molecules being the half of that around –OH groups of PVA (see Table 5.4).

In the region 2 (hydrophobic), $P_{res}(t)$ decreases in a rather shorter time than that in the region 1 because the hydrophobic groups form no hydrogen-bonds with water. For PVME and PNiPAM, the relaxations of $P_{res}(t)$ are slower than those for PVA because the volumes of the region 2 are large (see Table 5.4) for former two polymers and also mobility of water are decreased by the structuralization of water molecules around $-CH_3$ groups. For PVME, the relaxation of $P_{res}(t)$ in the region 2 is the same rate as that in the region 1. In the region 3 (bulk), no marked difference is observed among three polymers.

5.3.6 Hydrogen-bond of Water

The distribution of hydrogen-bond number per an atom, $P_{HB}(n)$, where n is the number of hydrogen bonds, is calculated averaging 1000 configurations for each system of $c_w \simeq 25$ and 50 wt %, and 800 configurations for each system of $c_w \simeq 75$ wt %. Figure 5.8 shows $P_{HB}(n)$ of water–water hydrogen-bonds in

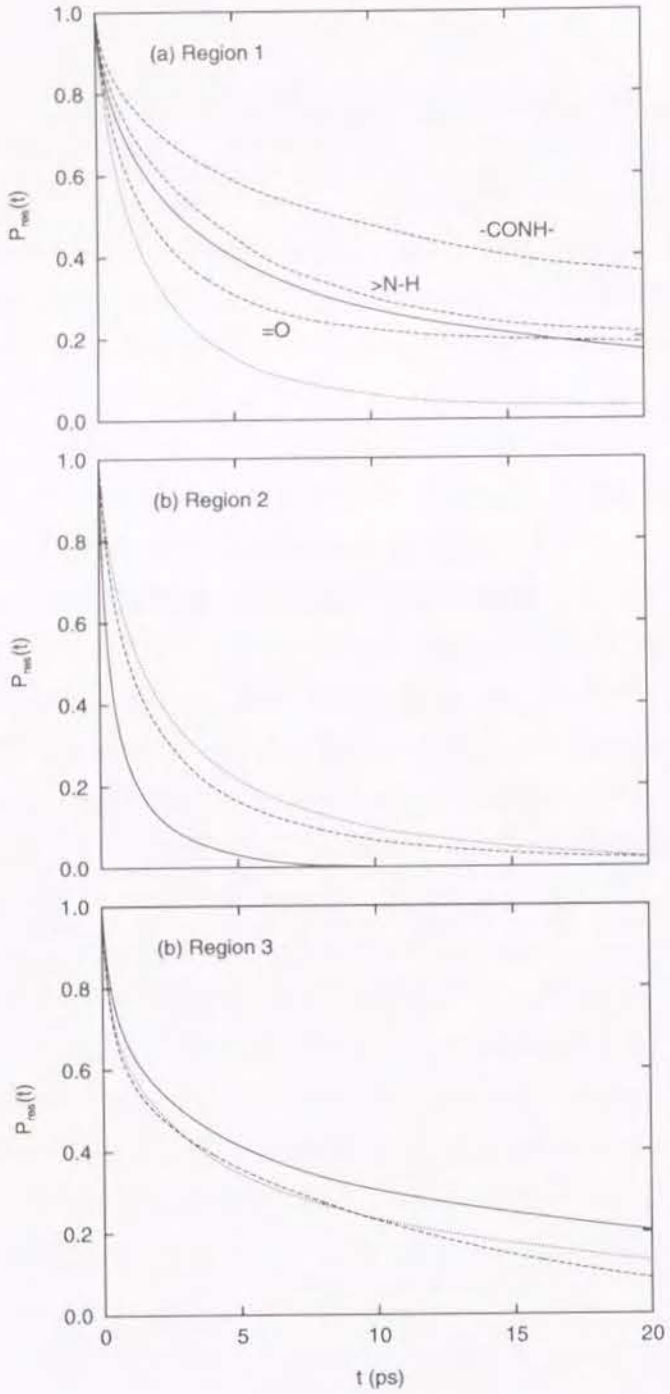

Figure 5.7. Residence rate $P_{\rm res}(t)$ of water at 300 K for (a) region 1, (b) region 2, and (c) region 3: (solid line) PVA, (dotted line) PVME, (dashed line) PNiPAM.

each region for the system of PVA with a water content 50 wt %. In pure water, 50 % of water molecules form four hydrogen-bonds. In the region 3 (bulk), the distribution is similar to those in pure water; the fraction of four hydrogen-bonds is slightly larger. The fractions of three and four hydrogen-bonds are almost same around hydrophobic groups. On the other hand, most of the hydrogen-bond number around hydrophilic groups is 2 or 3, which is smaller by 1 than those in pure water. Water–water hydrogen-bonds are defected since hydrogen-bonds are formed between water and –OH groups of PVA.

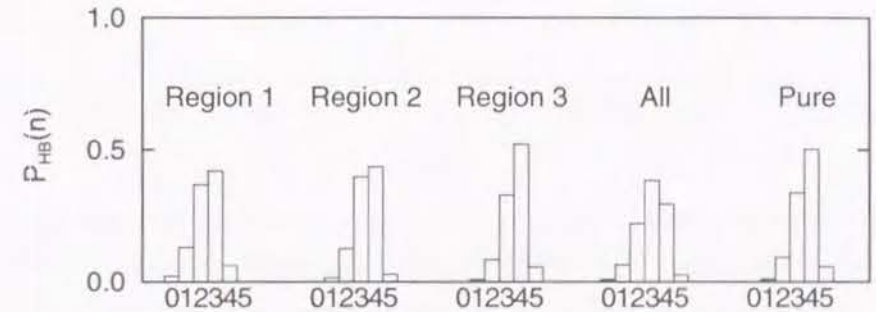

Figure 5.8. Hydrogen-bond number distribution, $P_{\rm HB}(n)$, calculated for water–water hydrogen-bonds at 300 K in the PVA hydrogel model with a water content 50 wt % and in pure water. The distributions are calculated for each region.

The average hydrogen-bond number, $\langle n_{\rm HB}\rangle$, is calculated from the distribution $P_{\rm HB}(n)$. Figures 5.9 and 5.10 show $\langle n_{\rm HB}\rangle$ of a water molecule in each region for the systems with $c_{\rm w} \simeq 50$ wt %. Figure 5.9 is obtained by counting the number of hydrogen-bonds of a water molecule in region 1 (hydrophilic). The lines with squares indicate $\langle n_{\rm HB}\rangle$ values calculated only for water–water hydrogen-bonds. The other lines show $\langle n_{\rm HB}\rangle$ for both water–water and water–polymer hydrogen-bonds. The calculated values in pure water are represented by diamonds. In the region 1, $\langle n_{\rm HB}\rangle$ values of water–water hydrogen-bonds are smaller by more than 1 bond than those in pure water since water molecules

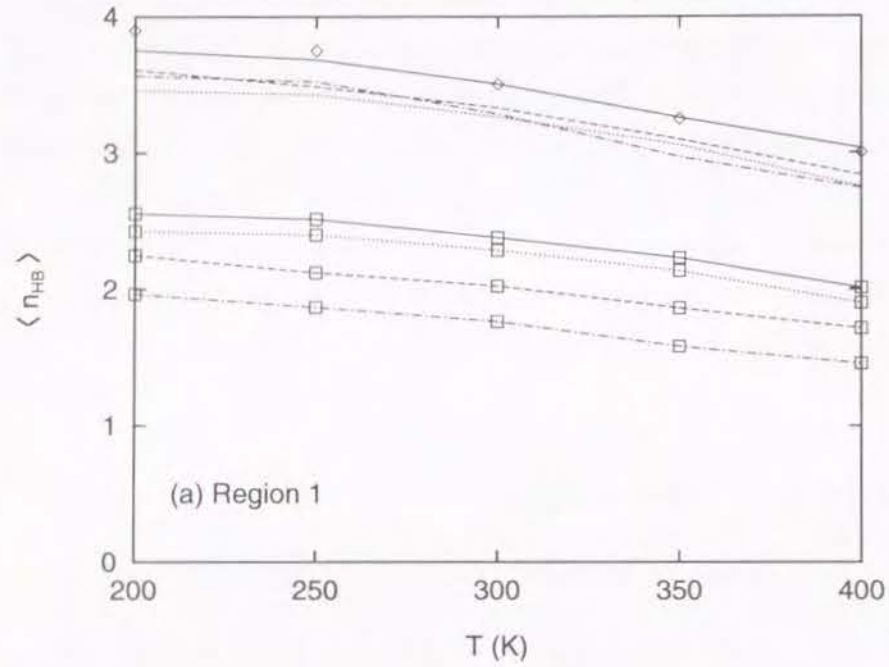

Figure 5.9. Average hydrogen-bond number $\langle n_{\mathrm{HB}} \rangle$ of a water molecule in the region 1: (solid line) PVA, (dotted line) PVME, (dashed line) around =O group of PNiPAM, (dash-dot line) around >NH group of PNiPAM, (diamond) pure water. Lines with squares indicate the values of $\langle n_{\mathrm{HB}} \rangle$ calculated for only water–water hydrogen-bonds. Other lines show $\langle n_{\mathrm{HB}} \rangle$ for both water–water and water–polymer hydrogen-bonds.

form hydrogen-bonds with the polymers. Around the >NH groups of PNiPAM, the values are smaller by approximately 1.5–1.9. Including the water–polymer hydrogen-bonds, the total numbers of hydrogen-bonds for the PVA hydrogel models are approximately equal to those in pure water. For the system of PVME and PNiPAM hydrogel models, the numbers are slightly smaller. The defects of water–water hydrogen-bonds are completely compensated by the water–polymer hydrogen-bonds for PVA but not for PVME and PNiPAM.

Figure 5.10 is obtained by counting the number of hydrogen-bonds of a water molecule in region 2 (hydrophobic). In the region 2, the number of water molecules around one water molecule is smaller than that in pure water by the presence of the polymer chains. Though this leads to smaller $\langle n_{\mathrm{HB}} \rangle$ values,

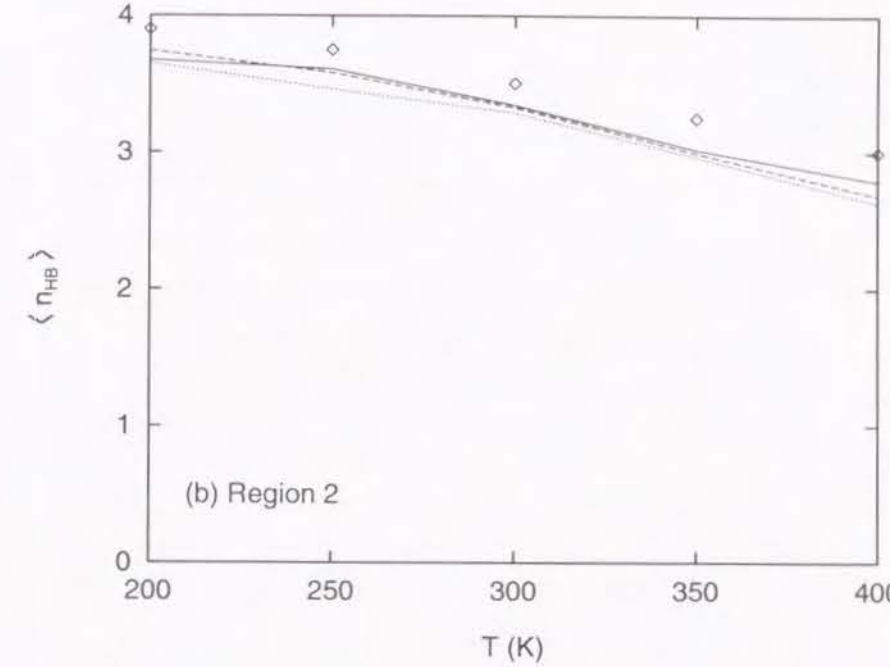

Figure 5.10. Average hydrogen-bond number $\langle n_{\mathrm{HB}} \rangle$ of a water molecule in the region 2: (solid line) PVA, (dotted line) PVME, (dashed line) PNiPAM, (diamond) pure water.

the degree of the decrease is very small. Therefore, the hydrogen-bonds are promoted so as to compensate for the small number of water molecules.

The values of $\langle n_{\mathrm{HB}} \rangle$ decrease with temperature. The slopes of the lines in Figure 5.9 and 5.10 are less steeper around the hydrophilic groups than those in pure water, and much steeper around the hydrophobic groups.

Though not shown in the figure, $\langle n_{\mathrm{HB}} \rangle$ values of a water molecule in the region 3 are equal to those in pure water irrespective of polymer species and water contents. In the region out of the first hydration shell, the hydrogen-bond numbers are not changed by polymers.

5.3.7 Hydrogen-bond of Polymer

Figure 5.11 shows $\langle n_{\mathrm{HB}} \rangle$ of a functional group of polymers for the systems with $c_{\mathrm{w}} \simeq 50$ wt %. Figure 5.11a shows $\langle n_{\mathrm{HB}} \rangle$ calculated from polymer–

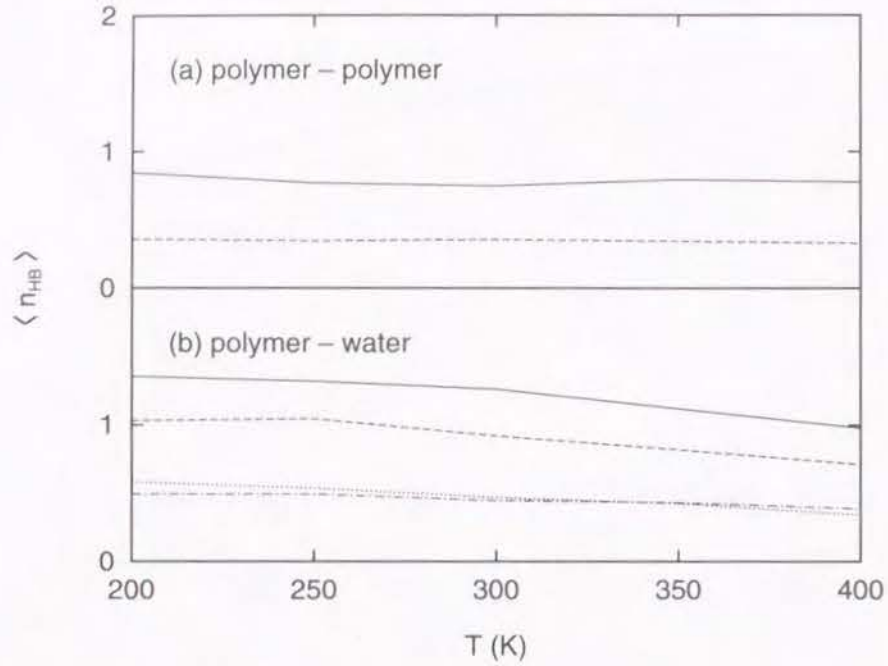

Figure 5.11. Average hydrogen-bond number $\langle n_{\rm HB} \rangle$ of a hydrophilic group of polymers calculated for (a) polymer–polymer and (b) polymer–water hydrogen-bonds: (solid line) PVA, (dotted line) PVME, (dashed and dash-dot lines) PNiPAM. Two lines for PNiPAM in part b show $\langle n_{\rm HB} \rangle$ of (dashed line) =O and (dash-dot line) >NH groups.

polymer hydrogen-bonds. PVA and PNiPAM forms polymer–polymer hydrogen-bonds, and PVME does not. The hydrogen-bond number is approximately 0.75 for a –OH group of PVA, and approximately 0.35 for =O and >NH groups of PNiPAM. The temperature dependences are very small; the numbers are approximately constant.

Figure 5.11b shows the results calculated from polymer–water hydrogen-bonds. A –OH group of PVA forms hydrogen-bonds with 1.3 water molecules, and a –O– group of PVME and a >NH group of PNiPAM with 0.5 water molecules at 300 K. The =O group of PNiPAM forms those with an intermediate number of water molecules: approximately 0.9. These values are 85–95 % of the coordination numbers of each system (see Table 5.2). The values of $\langle n_{\rm HB} \rangle$ decrease as increasing temperature.

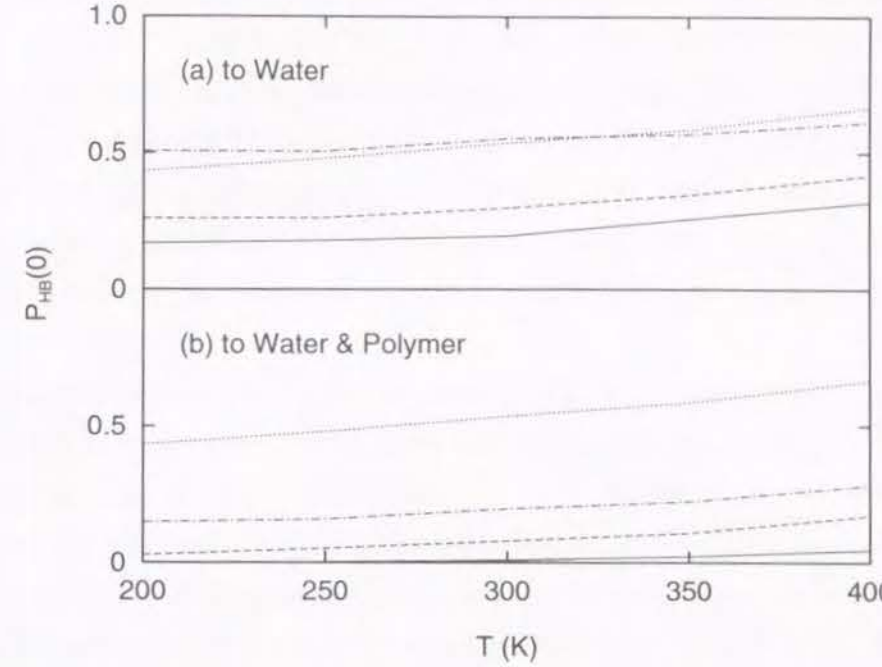

Figure 5.12. Non-hydrogen-bonded fraction $P_{\rm HB}(0)$ of a hydrophilic group of polymers calculated (a) for only polymer–water hydrogen-bonds and (b) for both polymer–water and polymer–polymer hydrogen-bonds: (solid line) PVA, (dotted line) PVME, (dashed line) =O group of PNiPAM, (dash-dot line) >NH group of PNiPAM.

It is expected that polymer–polymer hydrogen-bonds are also broken at high temperature, which leads to increase in mobility of side chains. In practice, polymer–polymer hydrogen-bond numbers, however, scarcely depend on temperature. The numbers of polymer–polymer hydrogen-bonds do not decrease. Global conformational transitions involving the whole chain are not observed. The conformation involving the polymer–polymer hydrogen-bonds is scarcely changed. Even when the hydrogen-bonds of side groups are broken, those are reformed in a short time period.

Figure 5.12 shows $P_{\rm HB}(n = 0)$ for the functional groups of polymers, which is interpreted as the probability that the groups form no hydrogen-bonds. Figure 5.12a shows the results obtained from only polymer–water hydrogen-bonds. For –O– of PVME and >NH of PNiPAM, half the polar groups form no

hydrogen-bonds with water at 300 K. The fraction of such groups is less than 30 % for >C=O of PNiPAM and less than 20 % for –OH of PVA. The values of $P_{\mathrm{HB}}(0)$ increase at high temperature; the *naked* polar groups increase with temperature. Figure 5.12b shows the results obtained from both polymer–water and polymer–polymer hydrogen-bonds. In the case including polymer–polymer hydrogen-bonds, $P_{\mathrm{HB}}(0)$ values of PVA and PNiPAM become smaller. Most of the polar groups of PVA are hydrogen-bonded in all the temperature range.

PVME and PNiPAM are soluble in water at low temperature but undergo phase separation at high temperature. Even if water molecules stay inside the polymer, the so-called hydrophobic interaction driven by the entropic contribution prevails and forces to squeeze the water molecules outside the gel and water molecules in contact with the polymer no longer stabilize it in gel form. Although the polymer–water hydrogen-bonds for PVA also decrease at high temperature, the effect to lower hydrophilicity is small.

5.3.8 Dependence on Water Content

Figure 5.13 shows the dependence of $\langle n_{\mathrm{HB}} \rangle$ of water on c_{w} at 300 K. The dash-dot lines are obtained by counting water–water hydrogen-bonds in the region 1 (hydrophilic). The numbers decrease at low water contents because of the decrease in number density of water molecules and the increase in polymer–water hydrogen-bonds. The numbers for PVA are larger than those for PNiPAM. The solid lines are obtained by counting both water–water and water–polymer hydrogen-bonds in the region 1. The numbers also decrease at low water contents. The slope of the dependence for PNiPAM is steeper than that for PVA. The dashed lines are obtained by counting hydrogen-bonds in the region 2 (hydrophobic), where the numbers also decrease at low water contents. The dependence is, however, less steeper than that in region 1. The dependence is hardly observed especially for PVA. In the region 3 (bulk), $\langle n_{\mathrm{HB}} \rangle$ values are independent of water contents and are the same as those in pure

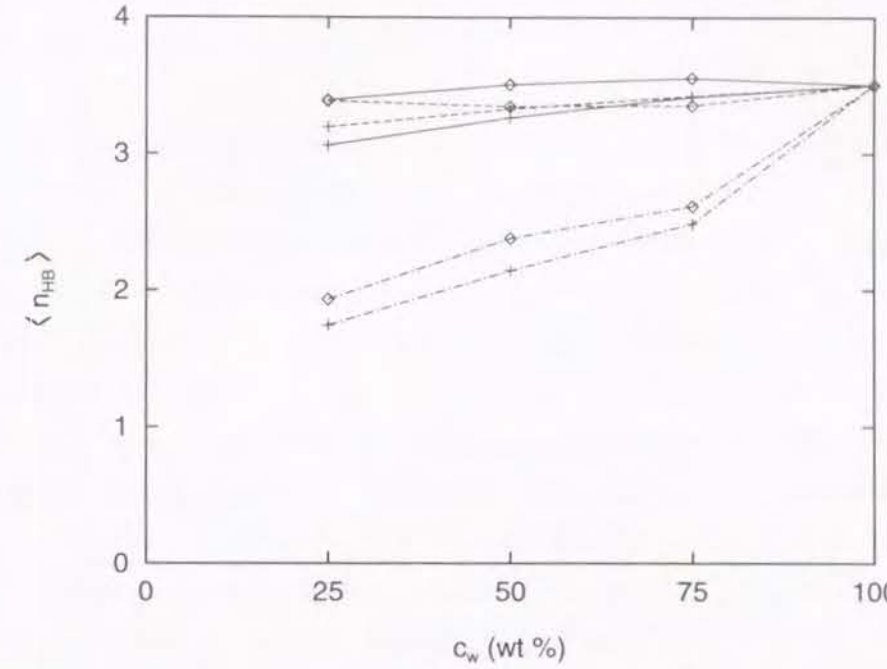

Figure 5.13. Average hydrogen-bond number $\langle n_{\mathrm{HB}} \rangle$ of a water molecule plotted against water content c_{w} at temperature 300 K: (solid line) region 1 (for both water–water and water–polymer), (dash-dot line) region 1 (for only water–water), (dashed line) region 2. Species of polymers are indicated by diamond (PVA) and cross (PNiPAM).

water.

Figure 5.14 shows the dependence of $\langle n_{\mathrm{HB}} \rangle$ on c_{w} for polar groups of polymers at 300 K. Parts a and b of Figure 5.14 are those for PVA and PNiPAM, respectively. With decreasing the water contents, the numbers of polymer–polymer hydrogen-bonds increase and polymer–water hydrogen-bonds decrease. The total numbers of hydrogen-bonds decrease at low water contents. The dependences are, however, small. For PNiPAM, the dependence of >C=O is larger than that of >NH.

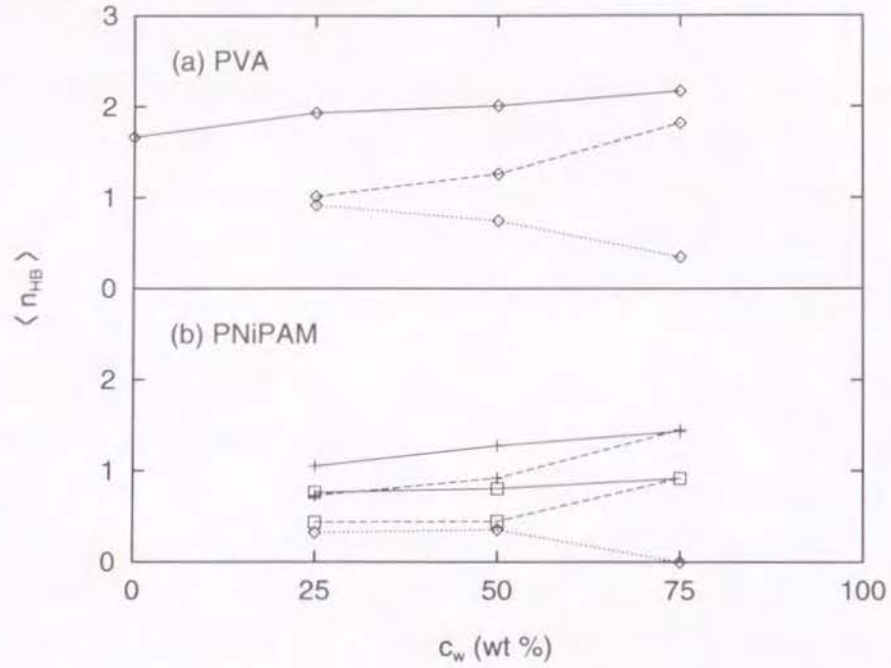

Figure 5.14. Average hydrogen-bond number $\langle n_{\mathrm{HB}} \rangle$ of a hydrophilic group of polymers plotted against water content c_{w}: (solid line) both polymer–water and polymer–polymer, (dashed line) only polymer–water, (dotted line) only polymer–polymer hydrogen-bonds. The groups =O and >NH of PNiPAM are indicated by crosses (=O) and squares (>NH).

5.3.9 Hydrogen-bond Defect

Defects of water–water hydrogen-bonds in comparison with pure water are caused in hydrogels by the presence of polymers. The number of defects per monomer unit is defined as

$$N_{\mathrm{D}} = \frac{\langle n_{\mathrm{HB}} \rangle_{\mathrm{w}} - \langle n_{\mathrm{HB}} \rangle_{\mathrm{g}}}{\langle n_{\mathrm{HB}} \rangle_{\mathrm{w}}} \times \frac{1}{f_{\mathrm{x}}} \tag{5.3}$$

where $\langle n_{\mathrm{HB}} \rangle_{\mathrm{w}}$ and $\langle n_{\mathrm{HB}} \rangle_{\mathrm{g}}$ are average numbers of water–water hydrogen-bonds per a water molecule in pure water and in hydrogel models, respectively, f_{x} is the number of monomer unit per one O–H group of water, which is expressed in this simulation as

$$f_{\mathrm{x}} = \frac{x}{2n_{\mathrm{w}}} \tag{5.4}$$

where x is the degree of polymerization and n_{w} is the number of water molecules in a unit cell.

The results are tabulated in Table 5.5. Clear temperature dependence is not observed. As for dependence on water contents, the numbers of water–water hydrogen bonds themselves decrease with decreasing water contents (see Figure 5.13), which leads to increase in the total numbers of hydrogen-bond defects. On the contrary, the defects per monomer unit, N_{D}, decrease because the fraction of the polar groups which induce defects in water–water hydrogen-bonds decreases by the increase of hydrogen-bonds between two polar groups of polymers. The N_{D} values are small for PVME, since the number of hydrogen-bonds to water is also small. The N_{D} values are large for PVA and PNiPAM because the numbers of hydrogen-bonds to water are large and, especially, PNiPAM has two polar groups in a monomer unit.

Terada et al.[61] determined the N_{D} values for various hydrophilic polymers by Raman spectroscopy. The values are varied by degrees of polymerization and cross-links. The results for aqueous solutions with a water content 70 wt % at 298 K are 2.6–9.8 for cross-linked polyacrylamide (PAAm) gel, 3.2–5.1 for linear PAAm, 1–2.3 for linear poly(ethylene glycol) (PEG), etc. The N_{D} values increased with increasing degrees of polymerization and cross-links. Since the conditions, degree of polymerization and polymer species, are different from our calculations, the calculated values cannot be compared directly to the experiments. It could be stated, however, that the calculated values are in a reasonable range. Terada et al.[61] showed that the numbers of defects in hydrophilic polymer solutions are greater than those in hydrophobic polymer solutions. This agrees qualitatively with our calculation. Maeda et al.[62] argued that the number of defects increases when the size of the cluster of *interstitial water* surrounded by polymer networks decreases below a critical size and the orientation of water molecules is restricted. Definitive evidence, however, is not be obtained from our calculation.

Table 5.5. Number of Hydrogen-bond Defects per Monomer Unit

T (K)	PVA	PVME	PNiPAM
	$c_w \simeq 25$ wt %		
200	0.69		1.05
250	0.67		1.07
300	0.63		1.04
350	0.64		1.13
400	0.63		1.22
Ave.	0.65		1.10
	$c_w \simeq 50$ wt %		
200	0.85	0.61	1.17
250	0.79	0.60	1.25
300	0.75	0.50	1.17
350	0.76	0.53	1.31
400	0.70	0.62	1.39
Ave.	0.77	0.57	1.26
	$c_w \simeq 75$ wt %		
200	1.12	0.97	2.06
250	1.06	0.97	1.75
300	1.08	0.68	1.59
350	1.09	0.91	1.82
400	1.21	1.06	2.43
Ave.	1.11	0.92	1.93

Table 5.6. Energy of Water–Water Hydrogen-bonds (kJ/mol)[a]

Polymer	Region 1	Region 2	Region 3
PVA	−19.64	−19.53	−19.42
PVME	−21.08	−20.18	−19.35
PNiPAM	−20.35	−19.89	−19.35

[a]For hydrogel models with a water content 50 wt % at 300 K.

5.3.10 Energy of Hydrogen-bonds

The energy of hydrogen-bonds is calculated to estimate the tightness of hydrogen-bonds. The nonbonded pair interaction energy is calculated for a pair of molecules which form a hydrogen-bond each other. The energy is averaged over 1000 configurations for each system. Table 5.6 lists the energies of water–water hydrogen-bonds in each region classified above. The table shows those for hydrogel models with $c_w \simeq 50$ wt % at 300 K. In the region 3 (bulk), the energies are almost the same as that in pure water, −19.35 kJ/mol, irrespective of polymer spices. In the region 1 (hydrophilic) and 2 (hydrophobic), the energies are lower (more stable) than those in the region 3. The stabilization of hydrogen-bond energy is very small for PVA but large for PVME and PNiPAM. Hydrogen-bonds are enhanced around polymer chains most significantly for PVME, which is most hydrophobic among three polymers. The same tendency is observed also for the systems with other water contents at other temperatures. Water–water hydrogen-bonds are enhanced by the presence of hydrophobic groups.

Table 5.7 lists the energy of polymer–water and polymer–polymer hydrogen-bonds. A monomer unit of polymer is treated as one group; the nonbonded pair potential energies are calculated for hydrogen-bond pairs between the group and water and between the two groups. No pairs of direct bonded neighbor groups are included in calculating the energy between two groups of polymers.

Table 5.7. Hydrogen-bond Energy of Polymers (kJ/mol)[a]

Polymer	Polymer–Water		Polymer–Polymer[b]	
	Coulomb	Total	Coulomb	Total
PVA (−OH)	−26.55	−20.58	−26.32	−21.53
PVME (−O−)	−20.63	−17.86		
PNiPAM (>CO)	−24.70	−22.34	−28.41	−38.05
PNiPAM (>NH)	−29.69	−26.13		

[a]For hydrogel models with a water content 50 wt % at 300 K.

[b]Not include hydrogen-bonds between neighbor segments.

The total energy, which includes the Coulomb and the Lennard-Jones terms, is very low for PNiPAM because PNiPAM has many Lennard-Jones interaction sites (carbon atoms) in a monomer unit. The Coulomb interaction energy is determined mostly by the contribution from atoms which participate directly in the hydrogen-bond. Therefore, the tightness of hydrogen-bonds can be estimated based on the Coulomb interaction. The tightness of polymer–water hydrogen-bonds follow the order of

$$\mathrm{NH(PNiPAM)} > \mathrm{OH(PVA)} > \mathrm{CO(PNiPAM)} > \mathrm{O(PVME)}$$

Although the >NH group of PNiPAM has small number of hydrogen-bonds, it forms the strongest hydrogen-bonds. The hydrogen-bonds are very tight for the >NH group. Those for PVME are not so tight since PVME is less polar. The polymer–polymer hydrogen-bonds are more tight for PNiPAM than PVA.

5.4 Conclusion

MD simulations have been carried out for the hydrogel models of PVA, PVME, and PNiPAM to elucidate the structure and dynamics between water and polymers. The simulations are performed for the systems with water

contents 0, 25, 50, and 75 wt % at five temperatures ranging from 200 to 400 K. The distributions of hydrogen-bonds are analyzed for water molecules which are classified into three categories: (1) around hydrophilic groups, (2) around hydrophobic groups, and (3) the remaining bulk region.

The average hydrogen-bond number $\langle n_{\mathrm{HB}} \rangle$ is calculated for a water molecule. In the region 1, water molecules are highly perturbed by the hydrophilic groups of polymers; the values of $\langle n_{\mathrm{HB}} \rangle$ of water–water hydrogen-bonds are smaller by 1–1.9 than those in pure water. The defects of water–water hydrogen-bonds are completely compensated by the water–polymer hydrogen-bonds for PVA but not for PVME and PNiPAM. In the region 2, $\langle n_{\mathrm{HB}} \rangle$ values are only slightly smaller than those in pure water, in spite of the presence of polymer chains. In the region 3, which is far from polymers, $\langle n_{\mathrm{HB}} \rangle$ values of a water molecule are equal to those in pure water irrespective of polymer species and water contents. The hydrogen-bonds are stabilized in the region 1 and 2 especially for PVME and PNiPAM; water–water hydrogen-bonds are enhanced by the presence of large hydrophobic groups. The hydrogen-bond numbers between water and polymers are the largest for PVA and the smallest for PVME. PVA is the most hydrophilic in character; only a small number of –OH groups are *naked* (not hydrogen-bonded to water).

In this chapter static properties of hydrogen-bonds are examined. Dynamics of hydrogen-bonds and mobility of water molecules are analyzed in Chapter 6.

Chapter 6

Dynamical Properties of Hydrogels

6.1 Introduction

The hydration structure and dynamics of proteins have been investigated by MD simulation. Kitao et al.[66] studied the hydration of melittin, which is a bioactive polypeptide consisting of 26 amino acid residues and is a main component of bee venom. The diffusion coefficients of water are calculated in the classified areas around charged, polar, and nonpolar groups and in bulk. The water molecules in the first hydration shell around charged groups are immobilized by the strong interaction. The diffusion coefficients in the first hydration shell around polar and nonpolar groups are 40–50 % of that in pure water.

Poly(vinyl alcohol) (PVA) is soluble in water at high temperature. On the other hand, poly(vinyl methylether) (PVME) and poly(N-isopropyl acrylamide) (PNiPAM) undergo the volume phase separation at high temperature. Ohta et al.[63] examined the mobility of water molecules in the PNiPAM solution around the volume phase transition temperature, by NMR measurement of the spin–spin relaxation time T_2. In the pure water, T_2 increases linearly with temperature. In the PNiPAM solution, though T_2 increases with temperature in most the temperature range, it decreases discontinuously at the phase transition temperature, at which the mobility of water molecules is significantly suppressed. It is generally accepted that the volume phase transition phenomenon has a close relation to the change of the entropy of water caused by the hydrophobic hydration.

In this chapter, dynamics of hydrogen-bonds and mobility of water mole-

cules are analyzed for the hydrogel models of PVA, PVME, and PNiPAM.

6.2 Model and Simulation Details

The AMBER/OPLS force field is used for the polymers, and the SPC/E for water. The united atom approximation is applied for $-CH_3$, $-CH_2-$, and $-CH-$ groups. A detailed description of the potential functions is given in Appendix A. Initial structures of hydrogel model of PVA, PVME, and PNiPAM are generated by using the modified self-avoiding random walk method (see Appendix C). MD simulations are performed at 5 temperatures ranging from 200 to 400 K at a pressure 0.1 MPa (ca. 1 atm). Detailed descriptions of the generation of initial structures and MD simulations are given in Chapter 5. Analyses are made for the trajectories generated in Chapter 5.

6.3 Results and Discussion

6.3.1 Lifetime of Hydrogen-bonds

In order to explore dynamical properties of hydrogen-bonds, the lifetime of hydrogen-bonds is examined. The formation and destruction of hydrogen-bonds are recurring in hydrogels. $P_{\rm on}(t)$ is defined as a distribution of time from formation of a hydrogen-bond to destruction of the bond. $P_{\rm off}(t)$ is defined as a distribution of time from destruction of a hydrogen-bond to re-formation of the bond which was bonded previously with the exactly same pair. Histograms of $P_{\rm on}(t)$ and $P_{\rm off}(t)$ are calculated using the 5000 configurations separated by 10 fs, which amounts to 50 ps trajectory. The histograms are smoothed by averaging the values of successive 5 columns. Figures 6.1 and 6.2 show the distributions of $P_{\rm on}(t)$ and $P_{\rm off}(t)$, respectively, for the systems with $c_{\rm w} \simeq 50$ wt % at 300 K. For the hydrogen-bonds between polar groups of polymers, rapid destruction and re-formation whose time scale is shorter than 0.1 ps are observed dominantly in both $P_{\rm on}(t)$ and $P_{\rm off}(t)$. Very slow processes of the destruction and re-formation are also seen.

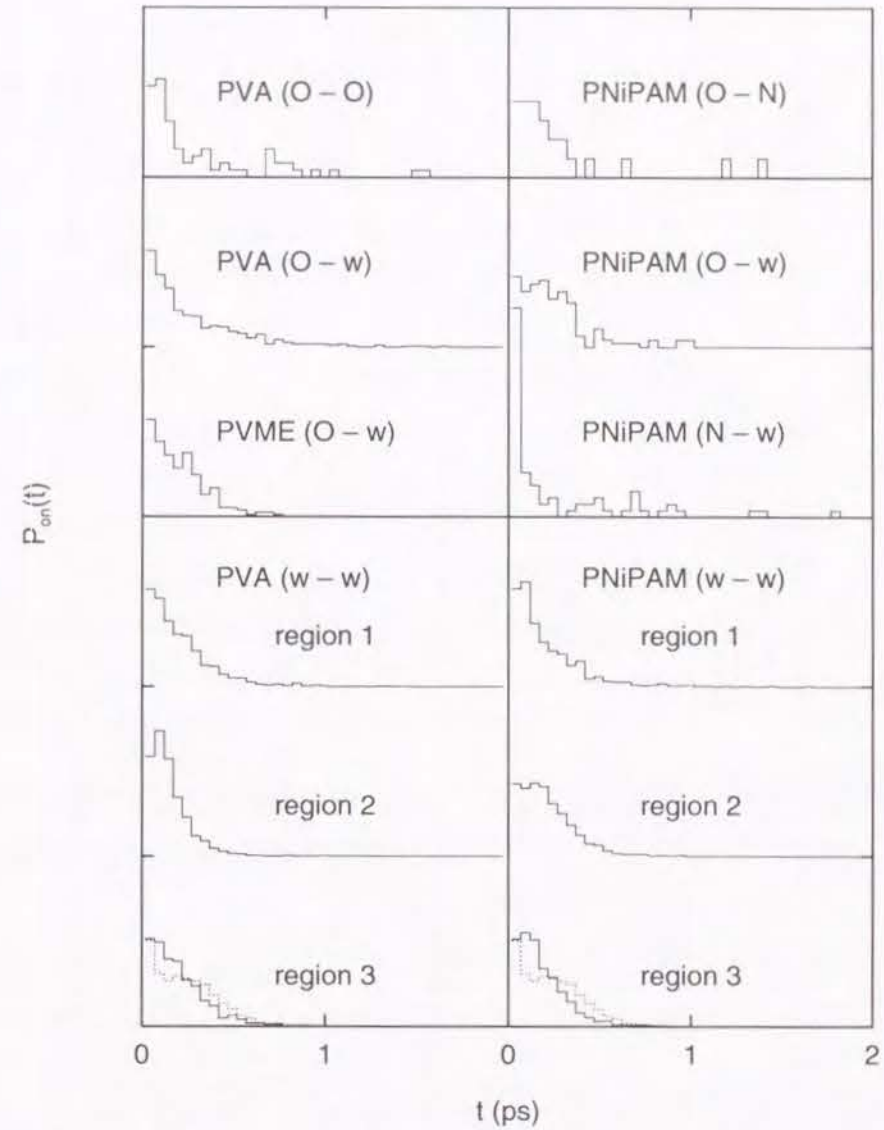

Figure 6.1. Lifetime distributions $P_{\rm on}(t)$ of hydrogen-bonds for hydrogel models with a water content 50 wt % at 300 K. Symbols O and N indicate oxygen and nitrogen atoms of polymers, respectively, and w indicates water. Dotted lines show those for pure water.

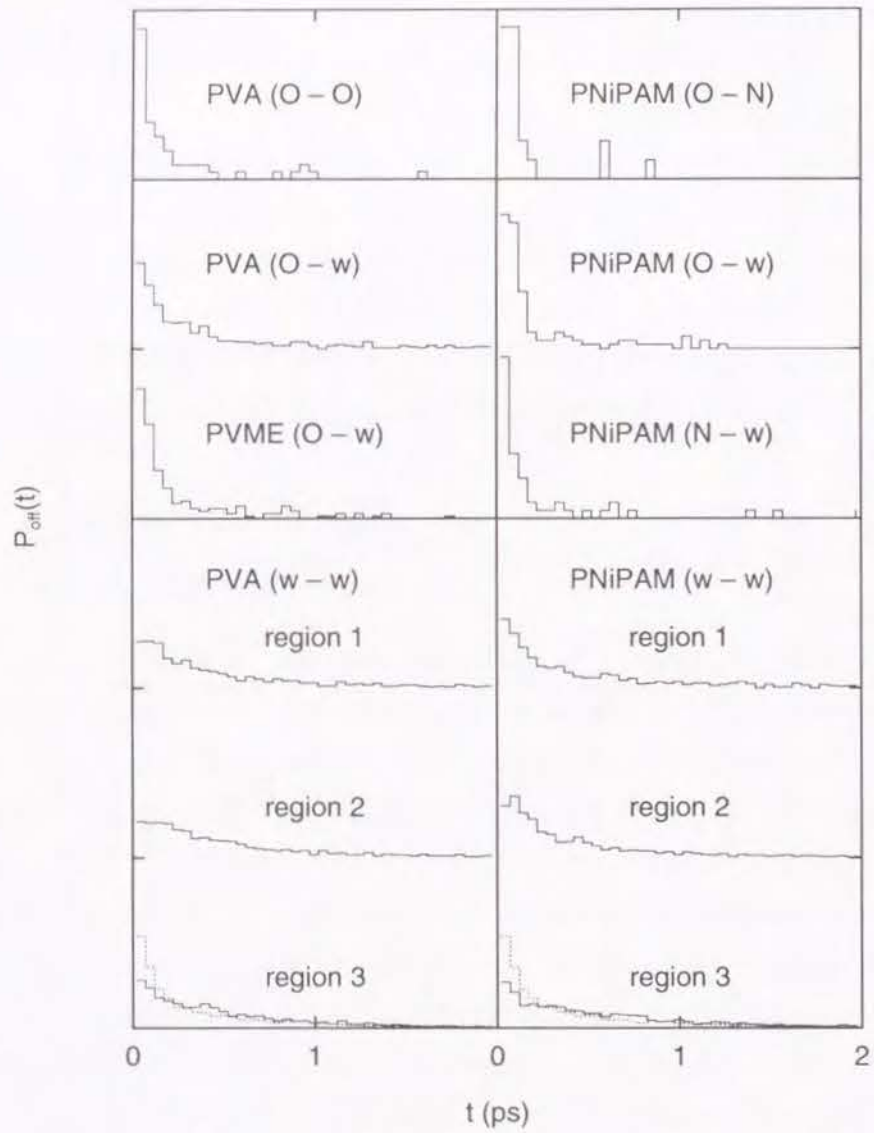

Figure 6.2. Lifetime distributions $P_{\rm off}(t)$ of hydrogen-bonds for hydrogel models with a water content 50 wt % at 300 K. Symbols O and N indicate oxygen and nitrogen atoms of polymers, respectively, and w indicates water. Dotted lines show those for pure water.

For the hydrogen-bonds between water and polymers, the distributions of $P_{\rm on}(t)$ and $P_{\rm off}(t)$ are highly dependent on the species of polar groups. The distributions for –OH of PVA and –O– of PVME are all similar to that for pure water. Those for PVA have the components longer than 1 ps, those for PVME do not. For a =O group of PNiPAM, the populations shorter than 0.1 ps are small; the distribution is broaden towards 0.5 ps. There are few pairs whose hydrogen-bond lifetime is longer than 1 ps. On the other hand, for a >NH group of PNiPAM, the populations shorter than 0.05 ps is much dominant. However, there are some pairs whose lifetime is fairly long. The distribution is as a whole similar to that between polar groups of polymers.

The distribution for water–water hydrogen-bonds around polymers is different from those in pure water. In the region 3, though the distributions resemble that in pure water, populations with shorter lifetime ($P_{\rm on}(t)$) and those of longer re-formation time ($P_{\rm off}(t)$) increase. In the region 2, the lifetime of PNiPAM is longer than that of PVA. The lifetime around hydrophobic groups of PNiPAM are longer than that in pure water, which arises partly from the structure promotion around those groups.

6.3.2 Correlation of Hydrogen-bond Pair

To obtain the information related to the exchange of hydrogen-bond pairs, we calculated the hydrogen-bond pair autocorrelation function

$$C_{\rm HB}(t) = \frac{\langle \sum_i h_i(t+t_0) \cdot h_i(t_0) \rangle}{\langle \sum_i h_i(t_0) \cdot h_i(t_0) \rangle} \tag{6.1}$$

where $h_i(t)$ is defined for an atom pair i at time t as

$$h_i(t) = \begin{cases} 1 & \text{(bonded)} \\ 0 & \text{(nonbonded)} \end{cases} \tag{6.2}$$

The sums are taken over the atom pairs which have already formed hydrogen-bonds at time t_0, and are averaged over all the time origins t_0. Calculation is performed for 5000 points of time origins (10 fs interval) during 50 ps. If

the same hydrogen-bond pairs persist for a long period, the $C_{\mathrm{HB}}(t)$ have a large value. If exchanges of bond pairs occur frequently, the values of $C_{\mathrm{HB}}(t)$ decrease in a short time.

Figure 6.3 shows those correlations for the systems with a water content 50 wt %. For $C_{\mathrm{HB}}(t)$ of hydrogen-bonds between two polar groups of polymers, the correlation of hydrogen-bond pairs of PNiPAM continues for a longer time than that of PVA. PNiPAM has large side chains, which depress the conformational transitions of polymer chains. Therefore, the exchange of hydrogen-bonds is suppressed.

For the hydrogen-bonds between water and polymers, $C_{\mathrm{HB}}(t)$ depends on the characters of polar groups. The polar groups of PVA and PVME show similar decays of $C_{\mathrm{HB}}(t)$. Those for PNiPAM exhibit longer correlation of hydrogen-bond pairs, especially for the >NH group. In the region 1 (hydrophilic) of PNiPAM, the decay of $P_{\mathrm{res}}(t)$ of water is slower than the other systems, as shown in Figure 5.7a. The profiles of $C_{\mathrm{HB}}(t)$ also show that smaller numbers of exchange of water molecules occur and the hydrogen-bonds which are formed by the same pairs exist for a long time.

For water–water hydrogen-bonds around polymers, the behaviors are again different for different region. The bottom parts of Figure 6.3 show those at 300 K for the systems of $c_{\mathrm{w}} \simeq 50$ wt %. The decay of $C_{\mathrm{HB}}(t)$ in the region 3 is the same as that for pure water but those in the region 1 and 2 are slower. The results for PVA are shown in the bottom-left part of Figure 6.3. In the region 1, rearrangements of water–water hydrogen-bonds are suppressed because of the decrease in the mobility of water molecules by polymer–water hydrogen-bonds. In the region 2, the correlation for a long time cannot be calculated since $P_{\mathrm{res}}(t)$ decays fast. The results for PNiPAM are shown in the bottom-right part of Figure 6.3. Since the exchanges of water molecules are hard to occur as described previously, only a small number of rearrangements is observed for water–water hydrogen-bonds in the region 1. The correlation in the region 2 is also higher than that in region 3.

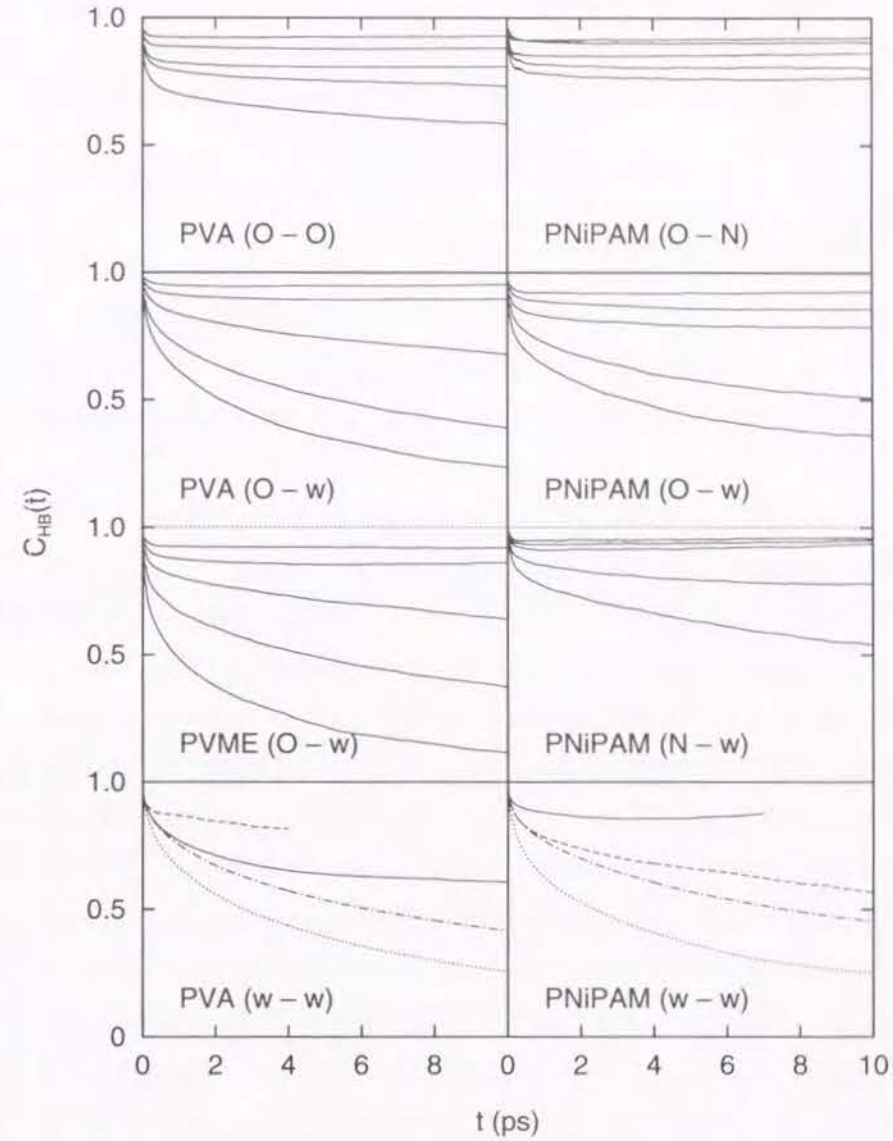

Figure 6.3. Hydrogen-bond pair autocorrelation function $C_{\mathrm{HB}}(t)$ of hydrogel models with a water content 50 wt %. Symbols O and N indicate oxygen and nitrogen atoms of polymers, respectively, and w indicates water. The $C_{\mathrm{HB}}(t)$ functions for polymer–polymer and polymer–water hydrogen-bonds (upper six parts of the figure) are calculated at 200, 250, 300, 350, and 400 K; each corresponds to the upper to the lower lines in each part. The $C_{\mathrm{HB}}(t)$ functions for water–water hydrogen-bonds (lowest two parts) are calculated at 300 K for (solid line) region 1, (dashed line) region 2, (dotted line) region 3, and (dash-dot line) whole region.

Similar results are obtained for the systems with the other water contents. All the correlations become higher for a longer time, with decreasing the water contents, for both polymer–water and water–water hydrogen-bonds. This is because the diffusivity of water molecules decreases in the systems with low water contents.

6.3.3 Diffusion of Water

To examine the effects of polymers on the translational motions of water, the diffusion coefficient of water is calculated for three regions classified above. The diffusion coefficient D is calculated from the mean-square displacement (MSD) as eq 3.1.

The MSD's deviated from linear at long time scales, when those are calculated for classified regions. This is because the relaxation of $P_{\rm res}(t)$ is very fast in the region 1 of PVME and the region 2 of the three polymers and the number of samples becomes very small in the regions. The long time behavior is characterized only by the particular samples which stay in the region for a long period. The molecules which staying in a specific region for a long time have low mobility, which gives rise to the deviation of MSD from a linear line. We should not consider the longer time behavior too seriously for calculation of diffusion coefficients and orientational relaxation time. In the time scales of 0.5–5 ps, the MSD's are approximately linear in time for all the systems. Therefore, the values of D are determined from the least-squares fit with a fitting range of this time scale. Figure 6.4 shows the Arrhenius plots of D calculated for the systems with $c_{\rm w} \simeq 50$ wt %. Parts a and b of Figure 6.4 show the results for PVA and PNiPAM, respectively. The straight lines in the figure are obtained by the least-squares method. The diffusion coefficients are well-fitted to the equation

$$D = D_0 \exp\left(-\frac{E_{\rm D}}{RT}\right) \tag{6.3}$$

from which the activation energy of diffusion, $E_{\rm D}$, is calculated.

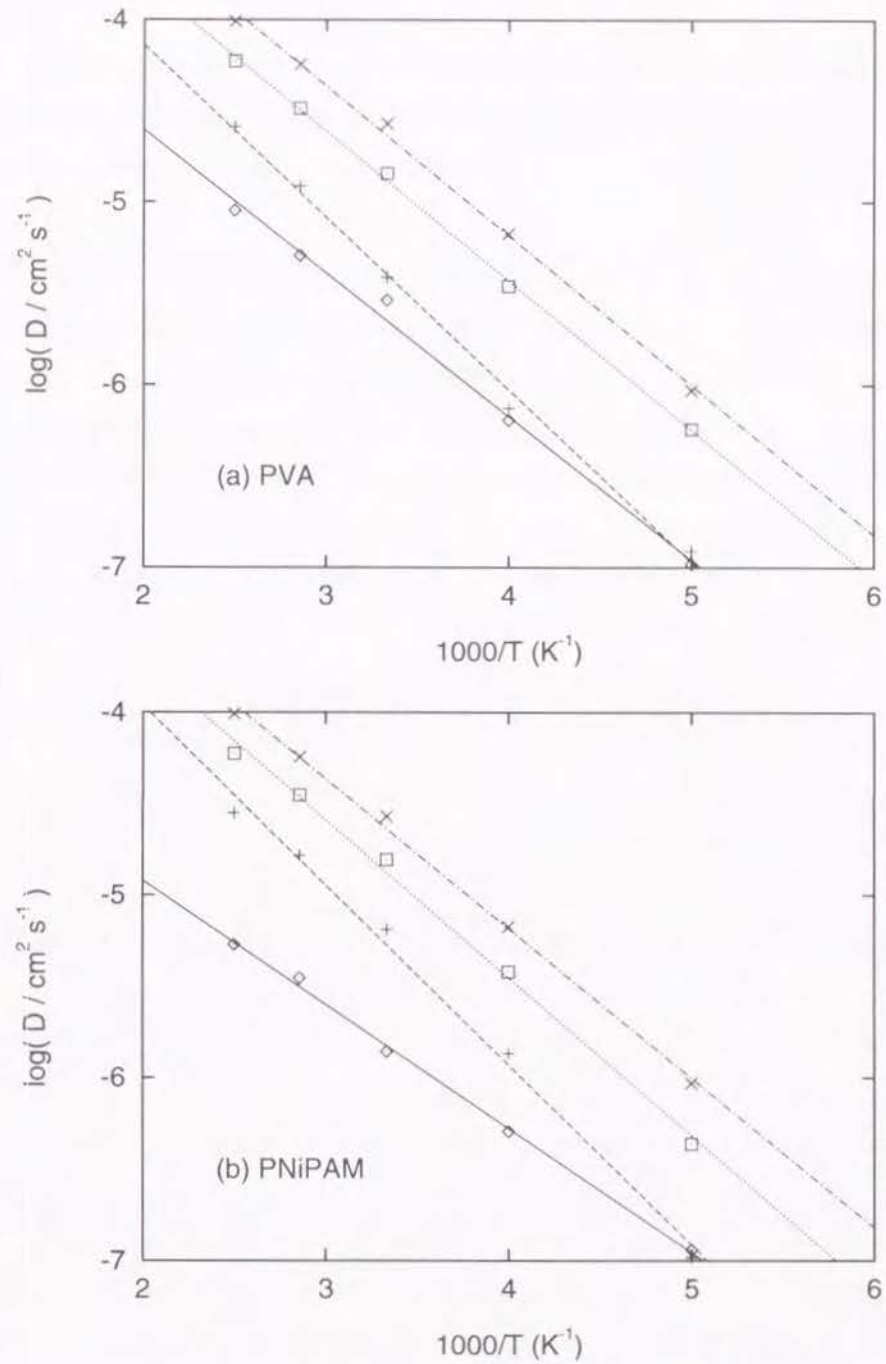

Figure 6.4. Arrhenius plot of diffusion coefficient D of water for (a) PVA and (b) PNiPAM hydrogel models with a water content 50 wt %: (solid line) region 1, (dashed line) region 2, (dotted line) region 3, (dash-dot line) pure water. The straight lines show the least-squares fits.

The experimental[37] diffusion coefficient for pure water is 2.11–2.66 $\times 10^{-5}$ cm^2/s at 298 K. The calculated value at 300 K agrees with the experiments. The calculated value of E_D is 3.7 kcal/mol, which agrees with the experimental values 4.4–4.8 kcal/mol, though slightly smaller.

In the region 1 and 2, the motions of water molecules are highly hindered by the presence of polymer chains. The diffusion coefficients are approximately 10–40 % of those in pure water. The motions are suppressed more significantly in the region 1 than in the region 2. The same tendency is observed for the PVME hydrogel models. In the region 1, the motions are hindered because of tight hydrogen-bonds between water and polymers and stabilization of water–water hydrogen-bonds. In the region 2, the motions are hindered because of the structuralization of water.

Knapp and Muegge[67] performed MD simulations for bovine pancreatic trypsin inhibitor (BPTI) in water and determined diffusion coefficient for water moving away from the protein surface with the aid of an analytical model. The diffusion of water is a factor of 4 slower in hydrophilic areas and is a factor of 15 faster in hydrophobic areas than in bulk water. Direct comparison between those results and ours is less meaningful since they determined the diffusion coefficients of water away from the surface by a parameter fitting method. The result in hydrophilic areas is, however, similar to our results. Using MD simulation, Kitao et al.[66] studied the hydration of melittin. The diffusion coefficients of water are calculated in the classified areas around charged, polar, and nonpolar groups and in bulk. The water molecules in the first hydration shell around charged groups are immobilized by the strong interaction. The diffusion coefficients in the first hydration shell around polar and nonpolar groups are 40–50 % of that in pure water. These values are the same order as our results.

Even in the region 3, where water molecules are distant from polymers, D is influenced by polymer and becomes smaller than that in pure water. For the systems with a water content 75 wt %, D values in the region 3 are almost

the same as those in pure water. For the systems with lower water contents, however, D values decrease in the bulk region by the presence of polymers. The reason for this is discussed below.

6.3.4 Local Motion of Water

In order to obtain the information about the local motion of water molecules, the spectral densities are calculated for the translational motion of water. The spectral density $G(\omega)$ is obtained from the Fourier transform of the translational velocity autocorrelation function as

$$G(\omega) = \frac{2}{\pi}\int_0^\infty \langle \mathbf{v}(t+t_0)\cdot\mathbf{v}(t_0)\rangle \cos(\omega t)\mathrm{d}t \tag{6.4}$$

where $\mathbf{v}(t)$ is the velocity of center of mass of a water molecule at time t, ω is the angular frequency, and $\langle \ldots \rangle$ means the ensemble average. Calculations are performed using the 5000 configurations saved by a 10 fs interval for 50 ps long. The spectra are smoothed with a help of a window function.

Figure 6.5 shows those spectra. The horizontal axis is wave number κ in cm^{-1} and the vertical axis is the spectral density $G(\kappa)$ in arbitrary unit. In the region 3 (bulk), the distributions are almost the same as those in pure water except for the diffusional component near $\kappa = 0$. In the region 2 (hydrophobic), the distributions are shifted by 15 cm^{-1} towards high frequency without deformation of the waveform. It is evident that the structure enhancement gives rise to this shift. There is little difference between PVA and PNiPAM. In the region 1 (hydrophilic), the intensity curves are highly deformed by the polymers; the high frequency components of 100–250 cm^{-1} increase. The intensities of the high frequency components follow the order of

$$\mathrm{NH(PNiPAM)} > \mathrm{CO(PNiPAM)} > \mathrm{OH(PVA)}$$

These results together with the analyses of the lifetime of hydrogen bonds lead us to a picture that water molecules around the >NH groups are strongly bounded to the groups and are also making intermittent formation and destruction of hydrogen-bonds in a short time scale.

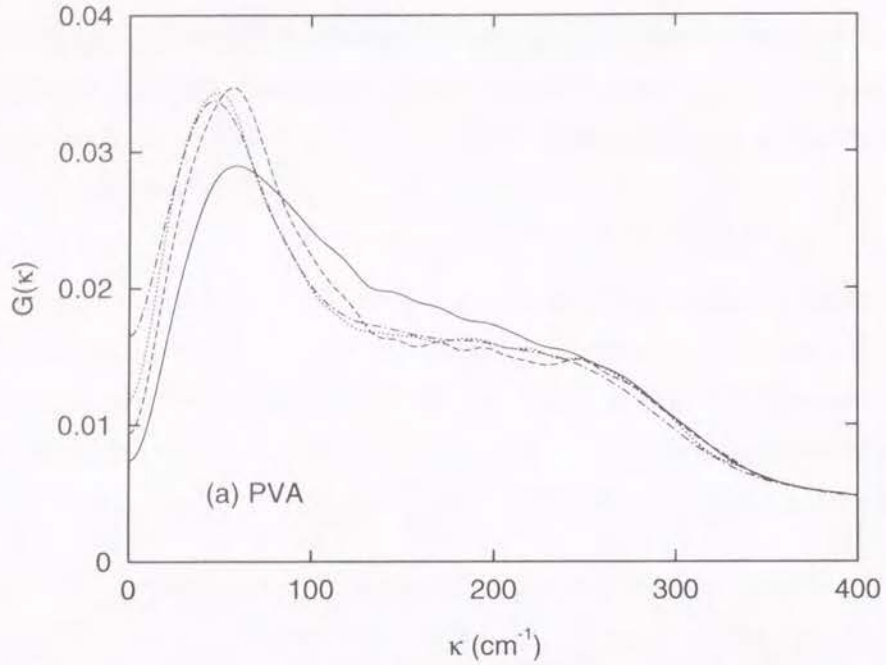

Figure 6.5. Spectral density $G(\kappa)$ of translational motion of water for (a) PVA and (b) PNiPAM hydrogel models with a water content 50 wt %: (solid line) region 1, (dashed line) region 2, (dotted line) region 3, (dash-dot line) pure water.

6.3.5 Orientational Relaxation of Water

To examine the effect of polymers on the rotational motions of water, the orientational relaxation time τ_{R} is calculated from the orientational autocorrelation function

$$C_{\mathrm{R}}(t) = \frac{\langle \boldsymbol{\mu}(t+t_0) \cdot \boldsymbol{\mu}(t_0) \rangle}{\langle \boldsymbol{\mu}(t_0) \cdot \boldsymbol{\mu}(t_0) \rangle} \tag{6.5}$$

where $\boldsymbol{\mu}(t)$ is the dipole vector of a water molecule at time t. At the time region shorter than 0.1 ps, the rapid relaxation caused by the libration of molecules is observed in $C_{\mathrm{R}}(t)$. At the time regions longer than 0.5 ps, the single exponential decay is observed. The orientational relaxation time τ_{R} is calculated by fitting the decay of $C_{\mathrm{R}}(t)$ to the exponential function

$$C_{\mathrm{R}}(t) = A \exp\left(-\frac{t}{\tau_{\mathrm{R}}}\right) \tag{6.6}$$

where A is a constant. When water molecules are classified into the regions, the decay of $C_{\mathrm{R}}(t)$ deviates from a single exponential function because of the problems previously described. In this case, the fitting procedure is performed with supplementing the long time scale behavior.

Figure 6.6 shows the Arrhenius plots of τ_{R} for water in each region of hydrogel models with a water content 50 wt %. Parts a and b of Figure 6.6 show those for PVA and PNiPAM, respectively. The plots are linear in all the regions. In the region 1 and 2, also the rotational motions of water molecules are highly suppressed by the presence of polymer chains. The motions are suppressed more severely in the region 1 than in the region 2. The values of τ_{R} are large around the hydrophilic groups because the motion of water molecules is constrained by the water–polymer hydrogen-bonds. The values of τ_{R} are also large around the hydrophobic groups because the structure of water is promoted in the region 2.

Even in the region 3, which is far from polymers, τ_{R} is influenced by polymer and is longer than that in pure water. Although τ_{R} values in the bulk region are not affected by the polymers for the systems with a water content 75 wt %, the values decrease for the systems with lower water contents.

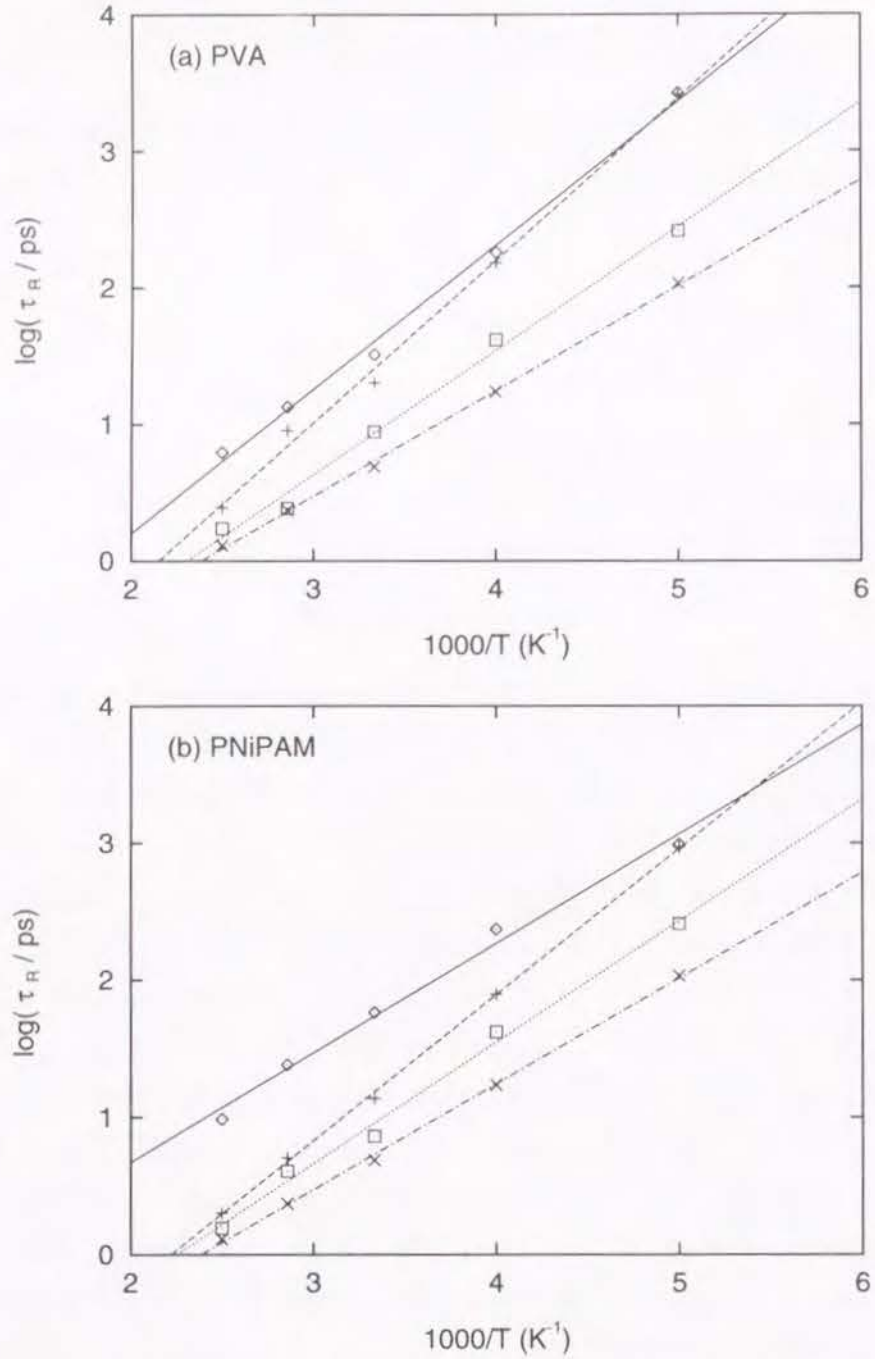

Figure 6.6. Arrhenius plot of orientational relaxation time τ_R of water for (a) PVA and (b) PNiPAM hydrogel models with a water content 50 wt %: (solid line) region 1, (dashed line) region 2, (dotted line) region 3, (dash-dot line) pure water. The straight lines show the least-squares fits.

In the bulk region, hydrogen-bond numbers and local motions are equal to those in pure water, irrespective of water contents. The translational diffusion and the orientational relaxation of water molecules are, however, suppressed by polymers for the systems of lower water contents. Water molecules are continuously spread over in whole the simulation cell and are preferentially dissolved in the bulk region for the system with a high water content. On the other hand, water molecules are compartmentalized for the system with a low water content. Therefore, though the local structure and local motion of water are not affected, the mobility of long time scales is suppressed for the latter system.

6.4 Conclusion

MD simulations have been carried out for the hydrogel models of PVA, PVME, and PNiPAM to elucidate the structure and dynamics between water and polymers. The simulations are performed for the systems with water contents 0, 25, 50, and 75 wt % at five temperatures ranging from 200 to 400 K. The distributions and dynamics of hydrogen-bonds, the translational diffusion, and the orientational relaxation are analyzed for water molecules which are classified into three categories: (1) around hydrophilic groups, (2) around hydrophobic groups, and (3) the remaining bulk region.

The effects of polymers on the properties of water molecules are varied with the spices of polar groups. The characters of the hydrophilic groups are reflected on the lifetime of hydrogen-bonds, the spectral density, etc. Around the >NH groups of PNiPAM, the analyses such as the residence rate, the lifetime of hydrogen-bonds, and the hydrogen-bond pair autocorrelation function show that exchange of water molecules hardly occurs and the polymer–water hydrogen-bonds persist for a long period. Although water molecules are strongly bounded to the >NH groups, the population having a lifetime of hydrogen-bonds shorter than 0.05 ps are dominant in the lifetime distribution. Those of very long time scales are also observed. This implies that the for-

mation and destruction of hydrogen-bonds are recurring in a short time scale. This is consistent with what we observed in the translational spectral density.

The mobility of water molecules is highly reduced around polymer chains for both translational and rotational motions. The mobility is reduced because of the hydrogen-bonds between water and polymers around the hydrophilic groups and because of the structuralization of water around the hydrophobic groups. In the bulk region, the hydrogen-bond numbers and local motions are equal to those in pure water irrespective of water contents. The mobility of long time scales is, however, lowered by polymers for the systems with low water contents. Compartmentation of water is one of the reason.

In this study, several analyses are made to elucidate interplay between water and polymers, with attentions directed mainly to the properties of water molecules. The effect of water molecules on the local motions of polymers is also an interesting subject. A discontinuous change is expected in the temperature dependence of mobility of water molecules around the phase transition temperature. In this study, however, it could not be observed partly because the simulation time is not long enough to observe the phase transition. Longer time scale simulations or more macroscopic models are needed since the entropy terms of polymer chains should be considered to describe the volume phase transition phenomena. The functional separation membrane is one of applications of hydrogels. Cooperative motions of water and polymers play an important role in the permeation phenomenon of gases in hydrogels. Further studies should be carried out to elucidate these phenomena.

Chapter 7

General Conclusion

The mechanism of permeation of small penetrants in polymer membranes were investigated from a microscopic view point by using the molecular simulation techniques. In the separation membranes, interaction between polymers and small molecules essentially contributes to their properties and functions. Influence of such interaction on static and dynamic properties was examined for hydrophobic (PDMS) and hydrophilic (hydrogels) membranes.

In Part I, a permeative mechanism of small molecules in hydrophobic polymer membranes was examined. MD simulations were performed for amorphous PDMS and PE as well as liquid water and ethanol. Diffusion processes and solubilities of small penetrants in those matrices were simulated.

In Chapter 2, the structures of the amorphous polymers and the liquids were generated and distribution and structure of the free volume were analyzed. In PDMS, the free volume is large and its distribution is broad; the free volume clusters are connected by channels. A penetrant in PDMS is expected to have large diffusion coefficient and large solubility, even for a large penetrant molecule such as ethanol.

In Chapter 3, the diffusion processes of methane, water, and ethanol in the polymers and the liquids were investigated. Diffusion coefficients of methane, water, and ethanol in PDMS are three times higher than those in amorphous PE. The calculated diffusion coefficients of the non-aggregated penetrant molecules agree reasonably with the experiments. Since water and ethanol have aggregative nature, they form aggregates in PDMS on our MD simulations. The calculated diffusion coefficients of aggregated molecules in PDMS are virtually zero, and those of free molecules are close to the experiments. This

implies that the overall transport is ascribed to diffusion of free penetrants.

In Chapter 4, the solubilities were evaluated from the excess chemical potentials which were calculated by the test particle insertion method (in the polymers) and the Shing–Gubbins method (in the liquids). The solubility of ethanol is much higher than that of water in PDMS and PE. This is owing to the strong Lennard-Jones interaction between ethanol and the polymers. PDMS has a structure in which a large molecule is soluble. The permeation rates, which were calculated from the diffusion coefficients and the solubilities, were in reasonable agreement with experimental data. Although ethanol has a smaller diffusion coefficient than water, ethanol has a larger permeation rate. This is because ethanol has a higher solubility in PDMS. This higher solubility accounts for the ethanol selectivity of the PDMS membrane.

In Part II, investigations were made on the interaction between water and polymers, which has close relation to the penetrant permeation phenomena. MD simulations have been performed for the hydrogel models of PVA, PVME, and PNiPAM to elucidate the interaction between water and polymers. The simulations were performed for the hydrogel models with various water contents under several temperature conditions.

In Chapter 5, analyses are made for the distribution and structure of hydrogen-bond networks. In the region 1, water molecules are highly perturbed by the hydrophilic groups of polymers; the average hydrogen-bond numbers $\langle n_{\mathrm{HB}} \rangle$ of a water molecule are smaller by 1–1.9 than those in pure water. In the region 2, $\langle n_{\mathrm{HB}} \rangle$ values are only slightly smaller than those in pure water. The hydrogen-bonds are stabilized in the region 1 and 2 especially for PVME and PNiPAM. Water–water hydrogen-bonds are enhanced by the presence of large hydrophobic groups.

In Chapter 6, dynamics of hydrogen-bonds and translational and rotational motions of water were analyzed. The mobility of water molecules is highly reduced around polymer chains. The mobility is reduced because of the hydrogen-bonds between water and polymers around the hydrophilic groups

and because of the structuralization of water around the hydrophobic groups. In the bulk region, the hydrogen-bond numbers and local motions are equal to those in pure water irrespective of water contents. The mobility of long time scales is, however, lowered by polymers for the systems with low water contents. Compartmentation of water is one of the reason for this.

The molecular simulation techniques may establish a direct relation between a microscopic structure and macroscopic thermodynamic properties. Taking advantage of the techniques, the permeation phenomenon of small penetrants in polymer materials was elucidated in view of atomistic information such as the interaction energy, the free volume distribution, and hydrogen-bond networks. Furthermore, atomistic information was successfully related to macroscopic properties such as the diffusion coefficient and the solubility. Application of these methods to various functional membranes and functional gels leads to prediction of properties and elucidation of mechanisms of functional expression. These methods are practicable to the material design in collaboration with experimental research. For wide application to the material design, longer time and longer range phenomena are desired to be simulated. This is hopefully realized in combination with a more macroscopic model or by coarse-graining with retaining information of interest.

Appendix A

Potential Functions and Parameters

Force Fields

For molecular mechanics (MM) and molecular dynamics (MD) simulation of nucleic acids and proteins, several research groups developed force fields, for example, AMBER,[69, 70] CHARMm,[71] GROMOS,[72] DREIDING,[73] UUF,[74] etc. In these force fields, molecules are modeled as interaction sites connected by chemical bonds. The sites interact with each other by bonded (bond length, bond angle, and dihedral angle) interactions and by nonbonded (Lennard-Jones and Coulomb) interactions. Structures and dynamics of various nucleic acids and proteins are examined by these force fields. MM and MD simulations of synthetic polymers have been performed by extending these force fields.

Structures and physico-chemical properties of water are well elucidated by molecular simulations. Jorgensen et al. made a comparison of simple potential functions for liquid water: Bernal–Fowler (BF), SPC, ST2, TIPS2, TIP3P, and TIP4P.[75] For simulations of proteins with water, 3 sites potential models are used for convenience, for example, TIP3P or SPC.

Jorgensen et al. determined a set of simple, transferable intermolecular potential functions (TIPS) for water, alkanes, alcohols, and ethers.[76] They reparameterized the TIPS to treat branched alkanes accurately.[77] The reparameterized potential functions along with the TIP4P potential for water are referred to as the OPLS functions for optimized potentials for liquid simulations. The OPLS models are extended to other organic liquids: peptide,[78] alcohol,[79] sulfur,[80] ether,[81, 82] ester,[83] etc. The OPLS describes intermolecular interaction effectively and reproduces experimental thermodynamic proper-

ties by molecular simulations. To simulate mixtures of polypeptide and water, the OPLS force field was merged into the AMBER,[69] i.e. the OPLS for intermolecular potential functions and the AMBER for intramolecular ones (AMBER/OPLS).[84] They performed energy minimization for crystals of polypeptide with water and obtained reasonable results.

Atom Types

For molecular simulations of mixtures of polymers and small molecules, intermolecular interaction is important as well as intramolecular ones. Table A.1 lists atom types of the PAMPS together with those of the AMBER and the CHARMm force fields. The Lennard-Jones size- and energy-parameters, σ and ϵ, respectively, are based on the OPLS potentials, which reproduces experimental thermodynamic properties. The parameters for PDMS are taken from a paper of Sok et al.[15] (GROMOS). The SPC/E[85] 3 sites model, which is a modified potential of the SPC, is used for water in the present study. In order to save computational resources, the united atom approximation can be used for >CH–, –CH_2–, –CH_3, and CH_4 groups, each of which is treated as a single interaction site.

Bonded Potentials

The intramolecular interactions are taken from the AMBER. Similar potential types, such as the CHARMm and the GROMOS, are also used instead of the AMBER type. The bond lengths and bond angles are subjected to the harmonic potentials given by

$$V(r) = k_r(r - r_0)^2 \tag{A.1}$$

$$V(\theta) = k_\theta(\theta - \theta_0)^2 \tag{A.2}$$

where r_0 is the equilibrium bond length, θ_0 is the equilibrium bond angle, and k_r and k_θ are the force constants. The bond lengths and bond angles can be

constrained to the equilibrium values r_0 and θ_0, respectively, by the SHAKE[92] algorithm.

The dihedral angle rotations are described by periodic functions as

$$V(\phi) = k_\phi[1 + \cos(n\phi - \delta)] \tag{A.3}$$

where k_ϕ is the force constant, n is the multiplicity factor, and δ is the phase shift. In the AMBER force field, the dihedral angle potential function is also used to describe the improper torsion angle potential, which ensures planarity of the sp^2 bond and prevents transitions from *d*- to *l*-structures and vice versa when used the united atom approximation for chiral >CH– groups.

The dihedral angle potential adopted for ethanol is taken from the OPLS potential model

$$V(\phi) = V_0 + \frac{V_1}{2}(1 + \cos\phi) + \frac{V_2}{2}(1 - \cos 2\phi) + \frac{V_3}{2}(1 + \cos 3\phi) \tag{A.4}$$

where V_i $(i = 0, 1, 2, 3)$ are the force constants.

All the bonded potential parameters used in the present study are summarized in Table A.2–A.6. The original potential parameters of the AMBER are used for bonded interactions. The bond angle parameters for CH_2–CH_2–CH_2, CH_2–CH–CH_3, and CH_2–O–CH_3 are substituted for CH_2–CH_2–CH_3, CH_2–CH–CH_2, and CH–O–CH_3, respectively, because the latter parameters are not defined in the original AMBER force field. The potential parameters for PDMS are taken from the GROMOS.[15]

Nonbonded Potentials

The Lennard-Jones interaction between atom i and j is described as

$$V_{\mathrm{LJ}}(r_{ij}) = \frac{A_{ij}}{{r_{ij}}^{12}} - \frac{C_{ij}}{{r_{ij}}^{6}} \tag{A.5}$$

where r_{ij} is the distance between atom i and j, A_{ij} and C_{ij} are parameters arising from the Lennard-Jones parameters. Standard combining rules are

used such that

$$\begin{aligned} A_{ij} &= \sqrt{A_{ii}A_{jj}} \\ C_{ij} &= \sqrt{C_{ii}C_{jj}} \end{aligned} \tag{A.6}$$

where A_{ii} and C_{ii} are expressed in terms of the Lennard-Jones size- and energy-parameters, ϵ and σ, as $A_{ii} = 4\epsilon_i{\sigma_i}^{12}$ and $C_{ii} = 4\epsilon_i{\sigma_i}^{6}$.

The Coulomb interaction is described as

$$V_C(r_{ij}) = \frac{q_i q_j}{4\pi\varepsilon_0 r_{ij}} \tag{A.7}$$

where q_i is the charge of atom i and ε_0 is the dielectric constant in vacuum.

Nonbonded interactions are not applied to 1,2- and 1,3-interacting pairs in the same molecule. The 1,4-nonbonded interactions are scaled from the normal nonbonded interactions by dividing the Lennard-Jones terms by factors 8.0 and the Coulomb terms by factors 2.0.[84] All the nonbonded potential parameters used in the present study are summarized in Table A.8.

Table A.1. Atom Types and Lennard-Jones Parameters

Atom type[a]			σ[b]	ϵ[c]	Comments
Hydrogen atoms					
H	(H	H)	0.0	0.0	amide and imino
HC	(HA	HC)	0.0	0.0	attached to carbon
HO	(H	HO)	0.0	0.0	hydroxyl or water
H3	(H	H3)	0.0	0.0	$-NH_3^+$
HS	(H	HS)	0.0	0.0	attached to sulfur
HT	(HT	HT)	0.0	0.0	TIP3P water
H_sc	(	)	0.0	0.0	SPC/E water
Carbon atoms					
C	(C	C)	3.750	0.105	carbonyl carbon
CT_2	(	)	3.750	0.105	C (sp^2)
CT_3	(CT	CT)	3.800	0.050	C (sp^3)
CH_2	(	)	3.800	0.115	CH (sp^2)
CH_3	(CH1E	CH)	3.850	0.080	CH (sp^3)
CH_n	(CH1E	CH)	3.800	0.080	CH (sp^3 with N_{amide})
C2_2	(	)	3.850	0.140	CH_2 (sp^2)
C2_3	(CH2E	C2)	3.905	0.118	CH_2 (sp^3)
C2_n	(CH2E	C2)	3.800	0.118	CH_2 (sp^3 with N_{amide}, O_{ester}, O_{ether}, S)
C3_1	(CH3E	C3)	3.775	0.207	CH_3 (C_1; ethane)
C3_2	(CH3E	C3)	3.905	0.175	CH_3 (C_2; n-butane)
C3_3	(CH3E	C3)	3.910	0.160	CH_3 (C_3; isobutane)
C3_4	(CH3E	C3)	3.960	0.145	CH_3 (C_4; neopentane)
C3_n	(CH3E	C3)	3.800	0.170	CH_3 (C_2 with N_{amide}, O_{ester}, O_{ether}, S)
C3sG	(	)	3.786	0.1799	PDMS (GROMOS)
C4	(C4	C4)	3.730	0.294	methane
C4_G	(	)	3.733	0.29775	methane (GROMOS)
CD	(C6RE	CD)	3.750	0.110	aromatic CH (6-membered ring)

Atom type[a]				σ[b]	ϵ[c]	Comments
Nitrogen atoms						
N	(NP	N	)	3.250	0.170	amide
N3	(NT	N3	)	3.250	0.170	$-NH_3{}^+$
NN	(		)	3.310	0.3101	N_2 (taken from ref 86)
Oxygen atoms						
O	(O	O	)	2.960	0.210	carbonyl
O2	(OC	O2	)	2.960	0.210	$-COO^-$
OH	(OT	OH	)	3.070	0.170	alcohol
OS	(OS	OS	)	3.000	0.170	ester
OE	(OE	OS	)	3.000	0.170	ether
OW	(OW	OW	)	3.1507	0.1521	TIP3P water
O_se	(		)	3.16556	0.15529	SPC/E water
OEsG	(		)	2.955	0.20285	PDMS (GROMOS)
OO	(		)	3.090	0.3708	O_2 (taken from ref 86)
Other atoms						
SIsG	(		)	3.385	0.58469	Silicon of PDMS (GROMOS)
AR	(		)	3.4	0.2388	argon (taken from ref 87)

[a] Atom types of CHARMm (1st) and AMBER (2nd) are shown in parentheses. [b] In Å. [c] In kcal/mol (1 cal = 4.1868 J).

Table A.2. Bonded Potential Parameters for PDMS[a]

bond	k_r	r_0	
C3sG–SIsG	250.0	1.880	
SIsG–OEsG	250.0	1.600	
angle	k_θ	θ_0	
C3sG–SIsG–C3sG	50.0	109.5	
C3sG–SIsG–OEsG	50.0	109.5	
SIsG–OEsG–SIsG	14.1	144.0	
OEsG–SIsG–OEsG	94.5	109.5	
dihedrals	k_ϕ	n	δ
C3sG–SIsG–OEsG–SIsG	0.90	3	0
SIsG–OEsG–SIsG–OEsG	0.90	3	0

[a]Energies are in kcal/mol (1 cal = 4.1868 J), distances in Å, and angles in rad (θ_0 in deg).

Table A.3. Bonded Potential Parameters for PE[a]

bond	k_r	r_0	
C2–C2	260.0	1.526	
C2–C3	260.0	1.526	
C3–C3	260.0	1.526	
angle	k_θ	θ_0	
C2–C2–C2	63.0	112.4	
C2–C2–C3	63.0	112.4	
C3–C2–C3	63.0	112.4	
dihedrals	k_ϕ	n	δ
C2–C2–C2–C2	2.00	3	0
C2–C2–C2–C3	2.00	3	0
C3–C2–C2–C3	2.00	3	0

[a] See footnote *a* of Table A.2.

Table A.4. Bonded Potential Parameters for PVA[a]

bond	k_r	r_0	
CH–C2	260.0	1.526	
CH–C3	260.0	1.526	
OH–CH	386.0	1.425	
HO–OH	553.0	0.960	
angle	k_θ	θ_0	
CH–C2–CH	63.0	112.4	
C2–CH–C2	63.0	111.5	
C2–CH–C3	63.0	111.5	
OH–CH–C2	80.0	109.5	
OH–CH–C3	80.0	109.5	
HO–OH–CH	55.0	108.5	
dihedrals	k_ϕ	n	δ
CH–C2–CH–C2	1.00	3	0
CH–C2–CH–C3	1.00	3	0
OH–CH–C2–CH	1.00	3	0
HO–OH–CH–C2	0.25	3	0
HO–OH–CH–C3	0.25	3	0
improper torsion	k_ϕ	n	δ
OH–CH–C2–C2	14.00	3	180
OH–CH–C2–C3	14.00	3	180
OH–CH–C3–C2	14.00	3	180

[a] See footnote *a* of Table A.2.

Table A.5. Bonded Potential Parameters for PVME[a]

bond	k_r	r_0	
CH–C2	260.0	1.526	
CH–C3	260.0	1.526	
OS–CH	320.0	1.425	
OS–C3	320.0	1.425	
angle	k_θ	θ_0	
CH–C2–CH	63.0	112.4	
C2–CH–C2	63.0	111.5	
C2–CH–C3	63.0	111.5	
OS–CH–C2	80.0	109.5	
OS–CH–C3	80.0	109.5	
C3–OS–CH	100.0	111.8	
dihedrals	k_ϕ	n	δ
CH–C2–CH–C2	1.00	3	0
CH–C2–CH–C3	1.00	3	0
CH–C2–CH–OS	1.00	3	0
C3–OS–CH–C2	0.70	3	0
C3–OS–CH–C3	0.70	3	0
C3–OS–CH–C3	0.10	2	0
improper torsion	k_ϕ	n	δ
OS–CH–C2–C2	14.00	3	180
OS–CH–C2–C3	14.00	3	180
OS–CH–C3–C2	14.00	3	180

[a] See footnote *a* of Table A.2.

Table A.6. Bonded Potential Parameters for PNiPAM[a]

bond	k_r	r_0
CH–C2	260.0	1.526
CH–C3	260.0	1.526
CH–C	317.0	1.522
C–O	570.0	1.229
C–N	490.0	1.335
N–H	434.0	1.010
N–CH	337.0	1.449
angle	k_θ	θ_0
CH–C2–CH	63.0	112.4
C2–CH–C2	63.0	111.5
C2–CH–C3	63.0	111.5
C3–CH–C3	63.0	111.5
C–CH–C2	63.0	111.1
C–CH–C3	63.0	111.1
CH–C–O	80.0	120.4
CH–C–N	70.0	116.6
O–C–N	80.0	122.9
C–N–H	35.0	119.8
CH–N–C	50.0	121.9
CH–N–H	38.0	118.4
C3–CH–N	80.0	109.5

dihedrals	k_ϕ	n	δ
CH–C2–CH–C2	1.00	3	0
CH–C2–CH–C3	1.00	3	0
CH–C2–CH–C	1.00	3	0
O–C–CH–C2	0.00	2	0
O–C–CH–C2	0.10	3	180
O–C–CH–C3	0.00	2	0
N–C–CH–C2	0.00	2	0
N–C–CH–C3	0.00	2	0
H–N–C–CH	2.50	2	180
H–N–C–O	0.60	1	0
H–N–C–O	2.50	2	180
CH–N–C–CH	2.50	2	180
CH–N–C–O	2.50	2	180
C3–CH–N–C	0.00	3	0
C3–CH–N–H	0.00	3	0
improper torsion	k_ϕ	n	δ
C–CH–C2–C2	14.00	3	180
C–CH–C2–C3	14.00	3	180
C–CH–C3–C2	14.00	3	180
O–C–N–CH	10.50	2	180
H–N–CH–C	1.00	2	180

[a] See footnote *a* of Table A.2.

Table A.7. Bonded Potential Parameters for Penetrants[a]

bond	k_r	r_0		
H_se–H_se	450.0	1.633		
H_se–O_se	450.0	1.000		
C2–C3	260.0	1.526		
OH–C2	386.0	1.425		
HO–OH	553.0	0.960		
angle	k_θ	θ_0		
H_se–O_se–H_se	[b]	109.5		
OH–C2–C3	80.0	109.5		
HO–OH–C2	55.0	108.5		
dihedrals (OPLS)	V_0	V_1	V_2	V_3
HO–OH–C2–C3	0.0	0.834	−0.116	0.747

[a] See footnote *a* of Table A.2. [b]The bond angle H_se–O_se–H_se of SPC/E water is fixed.

Table A.8. Nonbonded Potential Parameters[a]

atom	type	ϵ	σ	q	m
		PDMS			
Si	SIsG	0.58469	3.385	0.300	28.0800
O	OEsG	0.20285	2.955	−0.300	15.9990
CH_3	C3sG	0.17990	3.786	0.0	15.0350
		PE			
CH_2	C2_3	0.1180	3.905	0.0	14.0270
CH_3	C3_2	0.1750	3.905	0.0	15.0350
		PVA			
CH	CH_3	0.0800	3.850	0.265	13.0190
CH_2	C2_3	0.1180	3.905	0.0	14.0270
CH_3	C3_3	0.1600	3.910	0.0	15.0350
O	OH	0.1700	3.070	−0.70	15.9994
H	HO	0.0	0.0	0.435	1.0080
		PVME			
CH	CH_3	0.0800	3.850	0.25	13.0190
CH_2	C2_3	0.1180	3.905	0.0	14.0270
CH_3 (end)	C3_3	0.1600	3.910	0.0	15.0350
CH_3 (side)	C3_n	0.1700	3.800	0.25	15.0350
O	OE	0.1700	3.000	−0.50	15.9994

atom	type	ϵ	σ	q	m
		PNiPAM			
CH (main)	CH_3	0.0800	3.850	0.0	13.0190
CH (side)	CH_n	0.0800	3.800	0.20	13.0190
CH_2	C2_3	0.1180	3.905	0.0	14.0270
CH_3	C3_3	0.1600	3.910	0.0	15.0350
C (amide)	C	0.1050	3.750	0.50	12.0110
O (amide)	O	0.2100	2.960	−0.50	15.9994
N (amide)	N	0.1700	3.250	−0.57	14.0067
H (amide)	H	0.0	0.0	0.37	1.0080
		SPC/E water			
O	O_se	0.15529	3.1656	−0.8476	15.9994
H	H_se	0.0	0.0	0.4238	1.0080
		Ethanol			
CH_3	C3_2	0.1750	3.905	0.0	15.0350
CH_2	C2_3	0.1180	3.905	0.265	14.0270
O	OH	0.1700	3.070	−0.700	15.9994
H	HO	0.0	0.0	0.435	1.0080
		Gases			
CH_4	C4	0.2940	3.730	0.0	16.0430
N (N_2)	NN	0.3101	3.310	0.0	14.0067
O (O_2)	OO	0.3708	3.090	0.0	15.9994

[a]Energies are in kcal/mol, distances in Å, charges in e.s.u., and masses in g/mol.

Appendix B

Calculation of Long-range Forces

Potential Cutoff

The Lennard-Jones potential is cut off at $r_{\rm cut}$. The switching function

$$S(r) = \begin{cases} 1 & r \le r_{\rm sw} \\ \dfrac{(r - r_{\rm cut})^2(2r + r_{\rm cut} - 3r_{\rm sw})}{(r_{\rm cut} - r_{\rm sw})^3} & r_{\rm sw} < r < r_{\rm cut} \\ 0 & r_{\rm cut} \le r \end{cases} \tag{B.1}$$

is multiplied as

$$V_{\rm LJ}^{\rm swf}(r_{ij}) = V_{\rm LJ}(r_{ij})S(r_{ij}) \tag{B.2}$$

in order to smoothly cut off the Lennard-Jones interaction from full potential (at $r_{\rm sw}$) to zero (at $r_{\rm cut}$). Usually, we used $r_{\rm cut} = 10$ Å or so, and $r_{\rm cut} - r_{\rm sw} = 1$ Å. The contributions to the potential energy and pressure for $r > r_{\rm cut}$ are estimated by assuming that the radial distribution function $g(r)$ is unity in this region.[57]

The charge–charge interaction is categorized in the long-range force ($V_{\rm C}(r) \sim r^{-1}$), which causes a serious problem for the computer simulation since their range is greater than half the box length for a typical simulation of $\approx$ 500 molecules. In order to save computational time, however, the Coulomb potentials are also cut off at $r_{\rm cut}$ with the switching function $S(r)$ as

$$V_{\rm C}^{\rm swf}(r_{i_\alpha j_\beta}) = V_{\rm C}(r_{i_\alpha j_\beta})S(R_{\alpha\beta}) \tag{B.3}$$

where $R_{\alpha\beta}$ is the distance between the centers of mass of segments α and β, and $r_{i_\alpha j_\beta}$ is the distance between atom i_α (in segment α) and atom j_β (in segment β). The potentials are cut off by distances between centers of mass of

each segment, not in atomic basis. The charge neutrality should be preserved in each segment. A monomer unit is normally chosen as the segment for polymers, and a whole molecule for small molecules.

When solvent molecules are not explicitly simulated, the distance dependent dielectric constant[69] $\varepsilon(r)$ may be used instead of ε_0 as

$$V_{\mathrm{C}}^{\mathrm{ddd}}(r_{i_\alpha j_\beta}) = \frac{q_{i_\alpha} q_{j_\beta}}{4\pi\varepsilon(R_{\alpha\beta}) r_{i_\alpha j_\beta}} S(R_{\alpha\beta}) \tag{B.4}$$

to incorporate the screening effect on the Coulomb potential by polar solvent. Distances between pair segments in a unit of Å are used for the relative dielectric constants.[69]

$$\varepsilon(r) = \varepsilon_0 r \tag{B.5}$$

When solvent molecules are explicitly simulated, the distance dependent dielectric constant $\varepsilon(r)$ should not be used; the dielectric constant in vacuum ε_0 is used.

In order to handle the long-range Coulomb forces correctly, we use the Ewald sum,[88] which is a technique for efficiently summing the interaction between an ion and all its periodic images, as described in a next section.

Ewald Sum

The Coulomb potential energy of atom i located at $\mathbf{r}_i$, including that from all the periodic images, can be written as

$$\Phi_i = \frac{1}{2} \sum_{|\mathbf{n}|=0}^{\infty\prime} \sum_j \frac{q_i q_j}{|\mathbf{r}_{ij} + \mathbf{n}|} \tag{B.6}$$

where $\mathbf{r}_{ij} = \mathbf{r}_j - \mathbf{r}_i$ and $\mathbf{n} = (n_1 L_x, n_2 L_y, n_3 L_z)$ with integers $n_i = 0, \pm 1, \pm 2, \ldots$ and cell lengths L_x, L_y, L_z. The prime $\sum'$ indicates that we omit $i = j$ and 1,2-, 1,3-, and 1,4-interaction pairs for $\mathbf{n} = \mathbf{0}$. All the factors of $4\pi\varepsilon_0$ are omitted for simplicity. The 1,4-interaction potential (half the normal Coulomb potential) is calculated separately and is added to Φ_i later.

In the Ewald method,[88] the Coulomb potential energy is calculated by three terms as

$$\Phi_i = \Phi_i^{(1)} + \Phi_i^{(2)} + \Phi_i^{(3)} \tag{B.7}$$

$$\Phi_i^{(1)} = \frac{1}{2} q_i \sum_j q_j \frac{\mathrm{erfc}(\alpha|\mathbf{r}_{ij}|)}{|\mathbf{r}_{ij}|} \tag{B.8}$$

$$\begin{aligned}
\Phi_i^{(2)} &= \frac{4\pi}{V} q_i \sum_j q_j \sum_{\mathbf{k}\neq\mathbf{0}} \left[\exp\left(-\frac{|\mathbf{k}|^2}{4\alpha^2}\right) \frac{1}{|\mathbf{k}|^2} \cos(\mathbf{k}\cdot\mathbf{r}_{ij}) \right] \\
&= \frac{4\pi}{V} q_i \sum_{\mathbf{k}\neq\mathbf{0}} \left\{ \exp\left(-\frac{|\mathbf{k}|^2}{4\alpha^2}\right) \frac{1}{|\mathbf{k}|^2} \right. \\
&\quad \left. \times \left[\cos(\mathbf{k}\cdot\mathbf{r}_i) \sum_j q_j \cos(\mathbf{k}\cdot\mathbf{r}_j) - \sin(\mathbf{k}\cdot\mathbf{r}_i) \sum_j q_j \sin(\mathbf{k}\cdot\mathbf{r}_j) \right] \right\}
\end{aligned} \tag{B.9}$$

$$\Phi_i^{(3)} = -\frac{\alpha}{\sqrt{\pi}} {q_i}^2 - \frac{1}{2} q_i \sum_a q_a \frac{\mathrm{erf}(\alpha|\mathbf{r}_{ia}|)}{|\mathbf{r}_{ia}|} \tag{B.10}$$

In this method, each point charge is surrounded by a charge distribution of equal magnitude and opposite sign, which spreads out radially from the charge. This distribution is conveniently taken to be Gaussian

$$\rho_i(\mathbf{r}) = q_i \left(\frac{\alpha}{\sqrt{\pi}}\right)^3 \exp(-\alpha^2|\mathbf{r}|^2) \tag{B.11}$$

where the arbitrary parameter α determines the width of the distribution. The interaction of the point charge at $\mathbf{r}_i$ with the screened charge distribution is calculated in real space as $\Phi_i^{(1)}$ shown in eq B.8, where $\mathrm{erfc}(x)$ is the complementary error function

$$\mathrm{erfc}(x) = \frac{2}{\sqrt{\pi}} \int_x^\infty \exp(-t^2) dt$$

The constant α is chosen so that the only term which contributes to the sum in real space is that with $\mathbf{n} = \mathbf{0}$. Therefore, this term can be calculated by the normal minimum image convention. A charge distribution of the same sign as the original charge, and the same shape as the distribution $\rho_i(\mathbf{r})$ is

also added. This term, $\Phi_i^{(2)}$ shown in eq B.9, is a sum over reciprocal vector $\mathbf{k} = (k_1, k_2, k_3) = 2\pi\mathbf{h}'$, where

$$\mathbf{h}' = \left(\frac{h_1}{L_x}, \frac{h_2}{L_y}, \frac{h_3}{L_z}\right)$$

with integers $h_i = 0, \pm 1, \pm 2, \ldots$. The term for $\mathbf{k} = (0, 0, 0)$ is excluded from the sum. In practice 100–200 wave vectors are used in the k-space sum. The spurious term in the k-space summation that arises from the interaction of a charge at $\mathbf{r}_i$ with the distributed charge also centered at $\mathbf{r}_i$ must be subtracted from the total. For polyatomic molecules, it is also necessary to subtract the terms that arise from the interaction of the charge at $\mathbf{r}_i$ with the distributed charges centered at all the other sites within the third neighbor of i in the same molecule. This *self-term* is described as $\Phi_i^{(3)}$ shown in eq B.10, where index a denotes atoms within third neighbor of i ($a \neq i$) and $\mathrm{erf}(x)$ is the error function

$$\mathrm{erf}(x) = \frac{2}{\sqrt{\pi}} \int_0^x \exp(-t^2) dt$$

In this study, we used the cubic unit cell. The constant α is set to $5.6/L$ with a cell length L. All the integer components $\mathbf{h} = (h_1, h_2, h_3)$ which satisfy $|\mathbf{h}| \leq 5$ are used for the k-space sum.

The x-component of forces acting on atom i is described as

$$F_{i,x} = F_{i,x}^{(1)} + F_{i,x}^{(2)} + F_{i,x}^{(3)} \tag{B.12}$$

$$F_{i,x}^{(1)} = q_i \sum_j q_j \left[\frac{\mathrm{erfc}(\alpha|\mathbf{r}_{ij}|)}{|\mathbf{r}_{ij}|} + \frac{2\alpha}{\sqrt{\pi}} \exp(-\alpha^2|\mathbf{r}_{ij}|^2)\right] \frac{x_{ij}}{|\mathbf{r}_{ij}|^2} \tag{B.13}$$

$$\begin{aligned} F_{i,x}^{(2)} &= \frac{4\pi}{V} q_i \sum_j q_j \sum_{\mathbf{k}\neq\mathbf{0}} \left[\exp\left(-\frac{|\mathbf{k}|^2}{4\alpha^2}\right) \frac{k_1}{|\mathbf{k}|^2} \sin(\mathbf{k}\cdot\mathbf{r}_{ij})\right] \\ &= \frac{4\pi}{V} q_i \sum_{\mathbf{k}\neq\mathbf{0}} \left\{\exp\left(-\frac{|\mathbf{k}|^2}{4\alpha^2}\right) \frac{k_1}{|\mathbf{k}|^2} \right. \\ &\quad \left. \times \left[\sin(\mathbf{k}\cdot\mathbf{r}_i) \sum_j q_j \cos(\mathbf{k}\cdot\mathbf{r}_j) - \cos(\mathbf{k}\cdot\mathbf{r}_i) \sum_j q_j \sin(\mathbf{k}\cdot\mathbf{r}_j)\right]\right\} \end{aligned} \tag{B.14}$$

$$F_{i,x}^{(3)} = -q_i \sum_a q_a \left[\frac{\mathrm{erf}(\alpha|\mathbf{r}_{ia}|)}{|\mathbf{r}_{ia}|} - \frac{2\alpha}{\sqrt{\pi}} \exp(-\alpha^2|\mathbf{r}_{ij}|^2)\right] \frac{x_{ij}}{|\mathbf{r}_{ij}|^2} \tag{B.15}$$

where $F_{i,x}^{(1)}$, $F_{i,x}^{(2)}$, and $F_{i,x}^{(3)}$ are the contributions from potentials $\Phi_i^{(1)}$, $\Phi_i^{(2)}$, and $\Phi_i^{(3)}$, respectively, and x_{ij} is x-component of vector $\mathbf{r}_{ij}$.

Appendix C

Modified Self-avoiding Random Walk

Consider the chain and number its skeletal atoms from 0 to n. Skeletal bonds are numbered from 1 to n, so that bond vector $\mathbf{l}_i$ connects atoms $i-1$ and i. A part of the chain is shown in Figure C.1.[32] The bond rotation angle ϕ_i is the dihedral angle between the planes of bonds $(\mathbf{l}_{i-1}, \mathbf{l}_i)$ and bonds $(\mathbf{l}_i, \mathbf{l}_{i+1})$. The angle ϕ_i is measured in a right-hand sense relative to trans ($\phi_i = 0$ for trans conformation). The complementary bond angle θ_i is the angle between $\mathbf{l}_i$ and $\mathbf{l}_{i+1}$.

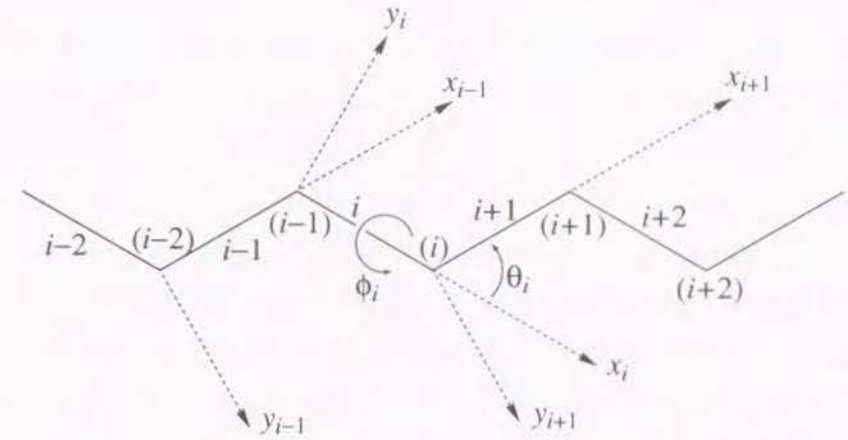

Figure C.1. Orthogonal local reference frame defined for neighbor bonds in a polymer chain. Atom index numbers are shown in parentheses. Bond i connects atoms $(i-1)$ and (i).

As shown in Figure C.1, orthogonal local reference frames (x_i, y_i, z_i) are introduced at skeletal bonds following the conventions of Flory (p 20 of ref 32). The direction of axis x_i is set to be identical to the direction of bond vector $\mathbf{l}_i$. Axis y_i is put on the plane determined by bond $i-1$ and i; the positive

direction is defined so that the projection on axis x_{i-1} has positive value. Axis z_i is defined in the right hand sense. The bond vector $\mathbf{l}_{i_a}^{(i)}$, which is defied for atom i_a in the local reference frame i, is transformed into global (external) reference frame (X_i, Y_i, Z_i) as

$$\mathbf{l}_{i_a}^{(g)} = \mathbf{T}_g \prod_{k=1}^{i-1} \mathbf{T}_k \mathbf{l}_{i_a}^{(i)} \tag{C.1}$$

where

$$\mathbf{T}_i = \begin{pmatrix} \cos\theta_i & \sin\theta_i & 0 \\ \sin\theta_i \cos\phi_i & -\cos\theta_i \cos\phi_i & \sin\phi_i \\ \sin\theta_i \sin\phi_i & -\cos\theta_i \sin\phi_i & -\cos\phi_i \end{pmatrix} \tag{C.2}$$

is the orthogonal transformation matrix from the reference frame of bond $\mathbf{l}_{i+1}$ to that of bond $\mathbf{l}_i$ and

$$\mathbf{T}_g = \begin{pmatrix} \cos\psi_3 \cos\psi_1 - \cos\psi_2 \sin\psi_1 \sin\psi_3 & -\sin\psi_3 \cos\psi_1 - \cos\psi_2 \sin\psi_1 \cos\psi_3 & \sin\psi_2 \sin\psi_1 \\ \cos\psi_3 \sin\psi_1 + \cos\psi_2 \cos\psi_1 \sin\psi_3 & -\sin\psi_3 \sin\psi_1 + \cos\psi_2 \cos\psi_1 \cos\psi_3 & -\sin\psi_2 \cos\psi_1 \\ \sin\psi_3 \sin\psi_2 & \cos\psi_3 \sin\psi_2 & \cos\psi_2 \end{pmatrix} \tag{C.3}$$

is the orthogonal transformation matrix of internal (local reference frame 0) to external (global) coordinates. The angles ψ_1, ψ_2, and ψ_3 are the Euler angles. The position vector of atom i_a is described as

$$\begin{aligned} \mathbf{a}_{i_a}^{(g)} &= \mathbf{a}_{i_p}^{(g)} + \mathbf{l}_{i_a}^{(g)} \\ &= \mathbf{a}_{i_p}^{(g)} + \mathbf{T}_g \prod_{k=1}^{i-1} \mathbf{T}_k \mathbf{l}_{i_a}^{(i)} \end{aligned} \tag{C.4}$$

in the global reference frame, where $\mathbf{a}_{i_p}^{(g)}$ is the position of parent atom i_p in the global reference frame. The parent atom i_p is located at the origin of the local reference frame (x_i, y_i, z_i), being also on x-axis in the local reference frame $(x_{i-1}, y_{i-1}, z_{i-1})$.

In the modified self-avoiding random walk method,[25] a chain is built up site by site with fixed bond lengths l_i and fixed bond angles θ_i and with randomly generated dihedral angles ϕ_i. A head group, which consists of the first three atoms of the chain, is settled in the unit cell at a random position $\mathbf{a}_0^{(g)}$ with random Euler angles (ψ_1, ψ_2, ψ_3). After evaluating the potential energy, the positions are accepted or rejected by the Monte Carlo method similar to the Metropolis scheme. Nonbonded potentials are modeled by the soft core type repulsive potentials[15]

$$\begin{aligned} V_{\rm s}(r) &= V_{\rm max} \left[1 - \left(\frac{r}{r_{\rm cut}} \right)^2 \right]^2 & r < r_{\rm cut} \\ &= 0 & r \geq r_{\rm cut} \end{aligned} \tag{C.5}$$

where $V_{\rm max}$ is a constant.

After the positions of the head group atoms are accepted, dihedral angles for the atoms of the subsequent chain are generated successively. A new position (dihedral angle ϕ) is generated, which is either accepted or rejected by the Monte Carlo method. The 1,4-interaction energy of a main chain is described as

$$V_{\rm s}(\phi) = V(\phi) + V_{\rm RIS}[{\rm state}(\phi)] \tag{C.6}$$

where $V(\phi)$ is described as eq A.3. $V_{\rm RIS}[{\rm state}(\phi)]$ is the first-order interaction energy of the rotational isomeric states (RIS) model,[32] where state(ϕ) denotes the state of conformation, i.e., *trans*, *gauche*$^+$, *gauche*$^-$, etc. No nonbonded 1,4-interaction is included in this term. Positions of side group atoms directly attached to atom $i-1$ are calculated in the local reference frame i. Then the positions of new added atoms are transformed into the global reference frame by eq C.4 using a set of $(\{l_i\}, \{\theta_i\}, \{\phi_i\})$. The nonbonded potential energy is estimated for $\{\mathbf{a}_{i_a}^{(g)}\}$. The new positions are either accepted or rejected.

For a small molecule, only the first step of the method is applied — whole molecule is treated as a head group. The modified self-avoiding random walk method may be applied also for branched polymers. Tree structures of branched polymers are generated by calling the routine recursively.

Appendix D

NPT Ensemble Combined with SHAKE

MD Simulations under the constant NPT ensemble are carried out by using the Nosé–Andersen method.[89, 90] The iterative method of Ferrario and Ryckaert[91] is used to integrate the equations of motion with the Verlet algorithm and the SHAKE algorithm.[92, 93] The time scaling of the Nosé method is performed on an atomic basis. The space scaling of the Andersen method is applied to centers of mass of molecules for rigid molecules and to real coordinates of atoms for flexible molecules.

Rigid Molecules

The equation of motion of atom i_α in a rigid molecule α and those for two extended degrees of freedom, V (volume of a unit cell) and S (time scaling parameter), are expressed as

$$m_{i_\alpha}\ddot{\mathbf{r}}_{i_\alpha} = \mathbf{F}_{i_\alpha} + \mathbf{G}_{i_\alpha} - \frac{\dot{S}}{S}\mathbf{p}_{i_\alpha} + \frac{m_{i_\alpha}}{3V}\left(\ddot{V} - \frac{2\dot{V}^2}{3V}\right)\mathbf{R}_\alpha \tag{D.1}$$

$$W_Q\ddot{V} = W_Q\frac{\dot{S}}{S}\dot{V} + S^2\left[\sum_{\alpha=1}^{N}\left(\frac{{\mathbf{P}_\alpha}^2}{M_\alpha} + \mathbf{F}_\alpha\cdot\mathbf{R}_\alpha\right)\frac{1}{3V} - P_{\text{ext}}\right] \tag{D.2}$$

$$W_s\ddot{S} = W_s\frac{\dot{S}^2}{S} + S\left[\sum_{\alpha=1}^{N}\sum_{i_\alpha=1}^{n_\alpha}\frac{{\mathbf{P}_{i_\alpha}}^2}{m_{i_\alpha}} - gk_{\text{B}}T_{\text{ext}}\right] \tag{D.3}$$

where m_{i_α} and M_α are the masses of atom i_α and molecule α, respectively, $\mathbf{F}_{i_\alpha}$ is the force acting on atom i_α, $\mathbf{G}_{i_\alpha}$ is the constraint force calculated by the SHAKE method, $\mathbf{R}_\alpha$ is the center of mass of molecule α, W_Q and W_s are "masses" of V and S, respectively, n_α is the number of atoms in molecule α, and g is the degree of freedom of the simulated system. P_{ext} and T_{ext} are

the external pressure and temperature, respectively, around which fluctuate the pressure and the temperature of a simulated system. $\mathbf{P}_\alpha$ and $\mathbf{p}_{i_\alpha}$ are the momenta of molecule α and atom i_α, respectively.

$$\mathbf{P}_\alpha = M_\alpha \left(\dot{\mathbf{R}}_\alpha - \mathbf{R}_\alpha \frac{\dot{V}}{3V} \right) \tag{D.4}$$

$$\mathbf{p}_{i_\alpha} = m_{i_\alpha} \left(\dot{\mathbf{r}}_{i_\alpha} - \mathbf{R}_\alpha \frac{\dot{V}}{3V} \right) \tag{D.5}$$

The Hamiltonian

$$H_2 = \sum_{\alpha=1}^{N} \sum_{i_\alpha=1}^{n_\alpha} \frac{{\mathbf{p}_{i_\alpha}}^2}{2m_{i_\alpha}} + U(\{\mathbf{r}_{i_\alpha}\}) + \frac{{P_V}^2}{2W_Q} + P_{\text{ext}} V + \frac{{P_s}^2}{2W_s} + g k_{\text{B}} T_{\text{ext}} \ln S \tag{D.6}$$

is a constant of motion, where $U(\{\mathbf{r}_{i_\alpha}\})$ is the potential energy and

$$P_V = W_Q \frac{\dot{V}}{S} \tag{D.7}$$

$$P_s = W_s \frac{\dot{S}}{S} \tag{D.8}$$

Since velocities are not explicitly used in the Verlet algorithm, the iterative method of Ferrario and Ryckaert[91] is used to integrate the equations of motion, as follows

(1) An initial estimate of velocities is evaluated according to

$$\dot{x}^{(0)}(t) = \frac{3x(t) - 4x(t-\Delta t) + x(t-2\Delta t)}{2\Delta t} + \mathcal{O}(\Delta t^2) \tag{D.9}$$

where Δt is the time step, and initialize an iteration index k to 0.

(2) The accelerations $\ddot{x}^{(k)}(t)$ for kth iteration are calculated by the equations of motion using the predicted velocities. The constraint forces $\mathbf{G}_{i_\alpha}$ are evaluated in this step.

(3) Estimate $x^{(k)}(t+\Delta t)$ using the Verlet algorithm, i.e.

$$x^{(k)}(t+\Delta t) = 2x(t) - x(t-\Delta t) + \ddot{x}^{(k)}(t)\Delta t^2 + \mathcal{O}(\Delta t^4) \tag{D.10}$$

(4) Evaluate a new estimate of velocities according to

$$\dot{x}^{(k+1)}(t) = \frac{x^{(k)}(t+\Delta t) - x(t-\Delta t)}{2\Delta t} + \mathcal{O}(\Delta t^2) \tag{D.11}$$

and increase k by 1 before going back to step (ii) as long as convergence is not reached.

The symbol x denotes $\mathbf{r}_{i_\alpha}$, V, and S. Usually, three iterations are sufficient for convergence.

Flexible Molecules

The equations of motion for the flexible molecules are described as

$$m_{i_\alpha} \ddot{\mathbf{r}}_{i_\alpha} = \mathbf{F}_{i_\alpha} + \mathbf{G}_{i_\alpha} - \frac{\dot{S}}{S} \mathbf{p}_{i_\alpha} + \frac{m_{i_\alpha}}{3V} \left(\ddot{V} - \frac{2\dot{V}^2}{3V} \right) \mathbf{r}_{i_\alpha} \tag{D.12}$$

$$W_Q \ddot{V} = W_Q \frac{\dot{S}}{S} \dot{V} + S^2 \left[\sum_{\alpha=1}^{N} \sum_{i_\alpha=1}^{n_\alpha} \left(\frac{{\mathbf{p}_{i_\alpha}}^2}{m_{i_\alpha}} + \mathbf{F}_{i_\alpha} \cdot \mathbf{r}_{i_\alpha} + \mathbf{G}_{i_\alpha} \cdot \mathbf{r}_{i_\alpha} \right) \frac{1}{3V} - P_{\text{ext}} \right] \tag{D.13}$$

$$W_s \ddot{S} = W_s \frac{\dot{S}^2}{S} + S \left[\sum_{\alpha=1}^{N} \sum_{i_\alpha=1}^{n_\alpha} \frac{{\mathbf{p}_{i_\alpha}}^2}{m_{i_\alpha}} - g k_{\text{B}} T_{\text{ext}} \right] \tag{D.14}$$

The virial $\mathbf{F}_{i_\alpha} \cdot \mathbf{r}_{i_\alpha}$ is calculated by an atomic basis. The equation of motion of V depends on the constraint virial $\mathbf{G}_{i_\alpha} \cdot \mathbf{r}_{i_\alpha}$. The momentum of atom i_α is

$$\mathbf{p}_{i_\alpha} = m_{i_\alpha} \left(\dot{\mathbf{r}}_{i_\alpha} - \mathbf{r}_{i_\alpha} \frac{\dot{V}}{3V} \right) \tag{D.15}$$

instead of eq D.5.

The equations of motion are solved by the Verlet algorithm

$$\mathbf{r}_{i_\alpha}(t+\Delta t) = 2\mathbf{r}_{i_\alpha}(t) - \mathbf{r}_{i_\alpha}(t-\Delta t) + \left(\frac{\mathbf{F}_{i_\alpha}}{m_{i_\alpha}} + \frac{\mathbf{G}_{i_\alpha}}{m_{i_\alpha}} \right) \Delta t^2 + \Delta \mathbf{r}_{i_\alpha} \tag{D.16}$$

where

$$\Delta \mathbf{r}_{i_\alpha} = \left[-\frac{\dot{S}}{S} \frac{\mathbf{p}_{i_\alpha}}{m_{i_\alpha}} + \frac{1}{3V} \left(\ddot{V} - \frac{2\dot{V}^2}{3V} \right) \mathbf{r}_{i_\alpha} \right] \Delta t^2 \tag{D.17}$$

For large molecules, the computer time for the constraint part can be important; an alternative method is used in which the overall time spent to compute the constraint forces contributions can be kept equivalent to the usual standard MD case, as follows.[93]

(1) compute $\{\mathbf{r}''_{i_\alpha}\}$ according to

$$\mathbf{r}''_{i_\alpha}(t+\Delta t) = 2\mathbf{r}_{i_\alpha}(t) - \mathbf{r}_{i_\alpha}(t-\Delta t) + \frac{\mathbf{F}_{i_\alpha}}{m_{i_\alpha}}\Delta t^2 \qquad \text{(D.18)}$$

(2) apply the constraint subroutine to $\{\mathbf{r}''_{i_\alpha}\}$ to produce $\{\tilde{\mathbf{r}}_{i_\alpha}\}$ just as if the last term of eq D.16 were absent. These terms affect the constraints only at order Δt^4.

(3) predict the time derivatives, $\{\dot{\mathbf{r}}^{(0)}_{i_\alpha}\}$, $\dot{V}^{(0)}$, and $\dot{S}^{(0)}$, according to eq D.9 and set index k to 0.

(4) compute $\ddot{V}^{(k)}$ and $\ddot{S}^{(k)}$ using eqs. D.13 and D.14.

(5) estimate the set $\{\mathbf{r}^{(k)}_{i_\alpha}\}$ by applying the constraint force routine to $\tilde{\mathbf{r}}_{i_\alpha} + \Delta\mathbf{r}_{i_\alpha}$.

(6) compute the new estimate of time derivatives $\{\dot{\mathbf{r}}^{(k+1)}_{i_\alpha}\}$, $\dot{V}^{(k+1)}$, and $\dot{S}^{(k+1)}$ using eq D.11.

(7) go back to step 4 after increasing the index k to $k+1$.

The number of iterations necessary to obtain $\{\tilde{\mathbf{r}}_{i_\alpha}\}$ in step 2 is similar to an ordinary MD step. In step 5, however, the number of additional iterations in the constraint force routine is much smaller.

Appendix E

Available Analysis by PAMPS

MD simulations are performed with writing out coordinates and velocities of atoms to disk files at a regular time interval. The analyses listed in Table E.1 are performed using the stored disk files. Numerical results of the analyses are automatically drawn by GNUPLOT.[94] Molecular structures are visualized by X-MOL[95] and RasMol[96] through interface programs.

Table E.1. Available Analyses by PAMPS

Structure	Distribution of bond length, bond and dihedral angles Radial distribution function Radius of gyration Static structure factor
Free volume	Distribution of accessible volume Cluster analysis
Hydrogen-bond	Distribution Energy Lifetime Correlation function of bonded pairs
Dynamics	Mean square displacement (MSD) Diffusion coefficient Orientational relaxation Spectral density

References

[1] Ciccotti, G.; Frenkel, D.; McDonald, I.R., Ed. *Simulation of Liquids and Solids*; North-Holland Elsevier Science Publishers B.V.: Amsterdam, The Netherlands, 1987.

[2] Widom, B. *J. Chem. Phys.* **1963**, *39*, 2808–2812.

[3] Panagiotopoulos, A. Z. *Mol. Simul.* **1992**, *9*, 1–23.

[4] Theodorou, D. N.; Suter, U. W. *Macromolecules* **1985**, *18*, 1467–1478.

[5] Theodorou, D. N.; Suter, U. W. *Macromolecules* **1986**, *19*, 139–154.

[6] Mansfield, K. F.; Theodorou, D. N. *Macromolecules* **1990**, *23*, 4430.

[7] Mansfield, K. F.; Theodorou, D. N. *Macromolecules* **1991**, *24*, 6283–6294.

[8] Hutnik, M.; Argon, A. S.; Suter, U. W. *Macromolecules* **1991**, *24*, 5956–5961.

[9] Hutnik, M.; Getile, F. T.; Ludovice, P. J.; Suter, U. W.; Argon, A. S. *Macromolecules* **1991**, *24*, 5962–5969.

[10] Hutnik, M.; Argon, A. S.; Suter, U. W. *Macromolecules* **1991**, *24*, 5970–5979.

[11] Fan, C. F.; Hsu, S. L. *Macromolecules* **1991**, *24*, 6244–6249.

[12] Fan, C. F.; Hsu, S. L. *Macromolecules* **1992**, *25*, 266–270.

[13] Takeuchi, H.; Okazaki, K. *J. Chem. Phys.* **1990**, *92*, 5643–5652.

[14] Takeuchi, H. *J. Chem. Phys.* **1990**, *93*, 2062–2067.

[15] Sok, R. M.; Berendsen, H. J. C.; van Gunsteren, W. F. *J. Chem. Phys.* **1992**, *96*, 4699–4704.

[16] Müller-Plathe, F. *J. Chem. Phys.* **1992**, *96*, 3200–3205.

[17] Müller-Plathe, F.; Rogers, S. C.; van Gunsteren, W. F. *Macromolecules* **1992**, *25*, 6722–6724.

[18] Müller-Plathe, F.; Rogers, S. C.; van Gunsteren, W. F. *Chem. Phys. Lett.* **1992**, *199*, 237–243.

[19] Müller-Plathe, F.; Rogers, S. C.; van Gunsteren, W. F. *J. Chem. Phys.* **1993**, *98*, 9895–9904.

[20] Pant, P. V. K.; Boyd, R. H. *Macromolecules* **1992**, *25*, 494–495.

[21] Pant, P. V. K.; Boyd, R. H. *Macromolecules* **1993**, *26*, 679–686.

[22] Huang, R. Y. M., Ed. *Pervaporation Membrane Separation Processes*; Elsevier Science Publishers B.V.: Amsterdam, The Netherlands, 1991.

[23] Ohmine, I.; Tanaka, H. *Chem. Rev.* **1993**, *93*, 2545–2566.

[24] Bellissent-Funel, M.-C.; Dore, J. C., Ed. *Hydrogen Bond Networks*; Kluwer Academic Publishers: Dordrecht, The Netherlands, 1994.

[25] Clarke, J. H. R.; Brown, D. *Mol. Simul.* **1989**, *3*, 27–47.

[26] Verlet, L. *Phys. Rev.* **1967**, *159*, 98–103.

[27] Allen, M. P.; Tildesley, D. J. *Computer Simulation of Liquids*; Oxford University Press: Oxford, U.K., 1987; pp 146–152.

[28] Shing, K. S.; Gubbins, K. E. *Mol. Phys.* **1982** *46*, 1109–1128.

[29] Gubbins, K. E. *Mol. Simul.* **1989** *2*, 223–252.

[30] Deitrick, G. L.; Scriven, L. E.; Davis, H. T. *J. Chem. Phys.* **1989**, *90*, 2370–2385.

[31] de Pablo, J. J.; Laso, M.; Suter, U. W. *J. Chem. Phys.* **1992**, *96*, 6157–6162.

[32] Flory, P. J. *Statistical Mechanics of Chain Molecules*; Interscience: New York, 1969.

[33] Shah, V. M.; Stern, S. A.; Ludovice, P. J. *Macromolecules* **1989**, *22*, 4660–4662.

[34] Arizzi, S.; Mott, P. H.; Suter, U. W. *J. Polym. Sci., Polym. Phys. Ed.* **1992**, *30*, 415–426.

[35] Greenfield, M. L.; Theodorou, D. N. *Macromolecules* **1993**, *26*, 5461–5472.

[36] Misra, S.; Mattice, W. L. *Macromolecules* **1993**, *26*, 7274–7282.

[37] Eisenberg, D.; Kauzmann, W. *The Structure and Properties of Water*; Oxford University Press: London, U.K., 1969.

[38] Zoller, P. *J. Appl. Polym. Sci.* **1979**, *23*, 1051.

[39] Flory, P. J.; Crescenzi, V.; Mark, J. E. *J. Am. Chem. Soc.* **1964**, *86*, 146.

[40] Bahar, I.; Zuniga, I.; Dodge, R.; Mattice, W. L. *Macromolecules* **1991**, *24*, 2986.

[41] Bahar, I.; Zuniga, I.; Dodge, R.; Mattice, W. L. *Macromolecules* **1991**, *24*, 2993.

[42] Palmer, B. J.; Garrett, B. C. *J. Chem. Phys.* **1993**, *98*, 4047.

[43] Pratt, L. R.; Pohorille, A. *Proc. Natl. Acad. Sci. U.S.A.* **1992**, *89*, 2995.

[44] Loyd, D. R.; Meluch, T. B. *ACS Symp. Ser.* **1985**, *269*, 47.

[45] Gusev, A. A.; Arizzi, S.; Suter, U. W.; Moll, D. J. *J. Chem. Phys.* **1993**, *99*, 2221.

[46] Gusev, A. A.; Suter, U. W. *J. Chem. Phys.* **1993**, *99*, 2228.

[47] Okamoto, K.; Nishioka, S.; Tsuru, S.; Sasaki, S.; Tanaka, K.; Kita, H. *Kobunshi Ronbunshu* **1988**, *45*, 993.

[48] Stern, S. A.; Shah, V. M.; Hardy B. J. *J. Polym. Sci., Polym. Phys. Ed.* **1987**, *25*, 1263.

[49] Wang, J. H. *J. Am. Chem. Soc.* **1951**, *73*, 510.

[50] Rathbun, R. E.; Babb, A. L. *J. Phys. Chem.* **1961**, *65*, 1072.

[51] Müller-Plathe, F. *Macromolecules* **1991**, *24*, 6475.

[52] Cracknell, R. F.; Nicholson, D.; Parsonage, N. G.; Evans, H. *Mol. Phys.* **1990**, *71*, 931.

[53] Laso, M.; de Pablo, J. J.; Suter, U. W. *J. Chem. Phys.* **1992**, *97*, 2817.

[54] Kumar, S. K.; Szleifer, I.; Panagiotopoulos, A. Z. *Phys. Rev. Lett.* **1991**, *66*, 2935.

[55] Sheng, Y. J.; Panagiotopoulos, A. Z.; Kumar, S. K.; Szleifer, I. *Macromolecules* **1994**, *27*, 400.

[56] Kumar, S. K. *Macromolecules* **1994**, *27*, 260.

[57] Allen, M. P.; Tildesley, D. J. *Computer Simulation of Liquids*; Oxford University Press: Oxford, U.K., 1987; pp 64–65.

[58] Sarkisov, G. H.; Dashevsky, V. G.; Malenkov G. G. *Mol. Phys.* **1974**, *27*, 1249.

[59] Mulder, M. H. V.; Smolders, C. A. *J. Membrane Sci.* **1984**, *17*, 289.

[60] Tamai, Y.; Tanaka, H.; Nakanishi, K. *Fluid Phase Equil.*, **1995**, *104*, 363.

[61] Terada, T.; Maeda, Y.; Kitano H. *J. Phys. Chem.* **1993**, *97*, 3619–3622.

[62] Maeda, Y.; Tsukida, N.; Kitano, H.; Terada, T.; Yamanaka, J. *J. Phys. Chem.* **1993**, *97*, 13903–13906.

[63] Ohta, H.; Ando, I.; Fujishige, S.; Kubota, K. *J. Polym. Sci., Polym. Phys. Ed.* **1991**, *29*, 963–968.

[64] Luzar, A.; Chandler, D. *J. Chem. Phys.* **1993**, *98*, 8160–8173.

[65] Kitao, A.; Hirata, F.; Gō, N. *Chem. Phys.* **1991**, *158*, 447–472.

[66] Kitao, A.; Hirata, F.; Gō, N. *J. Phys. Chem.* **1993**, *97*, 10223–10230.

[67] Knapp, E. W.; Muegge, I. *J. Phys. Chem.* **1993**, *97*, 11339–11343.

[68] Komiyama, J.; Satoh, M.; Zhang, W. Z.; Nodera, A.; Kusano, T.; Ogata, K.; Takahashi, S. *Polym. J.* **1991**, *23*, 379.

[69] Weiner, S. J.; Kollman, P. A.; Case, D. A.; Singh, U. C.; Ghio, C.; Alagona, G.; Profeta, S.; Weiner, P. *J. Am. Chem. Soc.* **1984**, *106*, 765–784.

[70] Weiner, S. J.; Kollman, P. A.; Nguyen, D. T.; Case, D. A. *J. Comput. Chem.* **1984**, *7*, 230–252.

[71] Brooks, B. R.; Bruccoleri, R. E.; Olafson, B. D.; States, D. J.; Swaminathan, S.; Karplus, M. *J. Comput. Chem.* **1983**, *4*, 187–217.

[72] Van Gunsteren, W. F.; Mark, A. E. *Eur. J. Biochem.* **1992**, *204*, 947–961.

[73] Mayo, S. L.; Olafson, B. D.; Goddard III, W. A. *J. Phys. Chem.* **1990**, *94*, 8897–8909.

[74] Rappé, A. K.; Casewit, C. J.; Colwel, K. S.; Goddard III, W. A.; Skiff, W. M. *J. Am. Chem. Soc.* **1992**, *114*, 10024–10053.

[75] Jorgensen, W. L.; Chandrasekhar, J.; Madura, J. D.; Impey, R. W.; Klein, M. L. *J. Chem. Phys.* **1983**, *79*, 926–935.

[76] Jorgensen, W. L. *J. Am. Chem. Soc.* **1981**, *103*, 335, 341, 345.

[77] Jorgensen, W. L.; Madura, J. D.; Swenson, C. J. *J. Am. Chem. Soc.* **1984**, *106*, 6638–6646.

[78] Jorgensen, W. L.; Swenson, C. J. *J. Am. Chem. Soc.* **1985**, *107*, 569–578.

[79] Jorgensen, W. L. *J. Phys. Chem.* **1986**, *90*, 1276–1284.

[80] Jorgensen, W. L. *J. Phys. Chem.* **1986**, *90*, 6379–6388.

[81] Jorgensen, W. L.; Mustafa, I. *J. Am. Chem. Soc.* **1981**, *103*, 3976–3985.

[82] Briggs, J. M.; Matsui, T.; Jorgensen, W. L. *J. Comput. Chem.* **1990**, *11*, 958–971.

[83] Briggs, J. M.; Nguye, T. B.; Jorgensen, W. L. *J. Phys. Chem.* **1991**, *95*, 3315–3322.

[84] Jorgensen, W. L.; Tirado-Rives, J. *J. Am. Chem. Soc.* **1988**, *110*, 1657–1666.

[85] Berendsen, H. J. C.; Grigera, J. R.; Straatsma, T. P. *J. Phys. Chem.* **1987**, *91*, 6269–6271.

[86] Fischer, J.; Lago, S. *J. Chem. Phys.* **1983**, *78*, 5750–5758.

[87] Rahman, A. *Phys. Rev.* **1964**, *136*, A405–A411.

[88] Allen, M. P.; Tildesley, D. J. *Computer Simulation of Liquids*; Oxford University Press: Oxford, U.K., 1987; pp 156–162.

[89] Nosé, S. *J. Chem. Phys.* **1984**, *81*, 511–519.

[90] Andersen, H. C. *J. Chem. Phys.* **1980**, *72*, 2384–2393.

[91] Ferrario, M.; Ryckaert, J. P. *Mol. Phys.* **1985**, *54*, 587–603.

[92] Ryckaert, J. P.; Ciccotti, G.; Berendsen, H. J. C. *J. Comput. Phys.* **1977**, *23*, 327–341.

[93] Ciccotti, G.; Ryckaert, J. P. *Coputer Physics Reports 4*; North-Holland Elsevier Science Publishers B.V.: Amsterdam, The Netherlands, 1987; pp 345–392.

[94] GNUPLOT is a software copyrighted by Thomas Williams and Colin Kelley.

[95] X-MOL is a software copyrighted by Research Equipment, Inc. dba Minnesota Supercomputer Center, Inc.

[96] RasMol is a software copyrighted by Roger Sayle.

List of Publications

Chapter 2

1. "Molecular Simulation of Permeation of Small Penetrants through Membranes. 1. Diffusion coefficients."
   Y. Tamai, H. Tanaka, K. Nakanishi, *Macromolecules*, **27**, 4498–4508 (1994).

Chapter 3

1. "Molecular Simulation of Permeation of Small Penetrants through Membranes. 1. Diffusion coefficients."
   Y. Tamai, H. Tanaka, K. Nakanishi, *Macromolecules*, **27**, 4498–4508 (1994).

Chapter 4

2. "Molecular Simulation of Permeation of Small Penetrants through Membranes. 2. Solubilities."
   Y. Tamai, H. Tanaka, K. Nakanishi, *Macromolecules*, **28**, 2544–2554 (1995).

3. "Molecular Design of Polymer Membranes using Molecular Simulation Technique."
   Y. Tamai, H. Tanaka, K. Nakanishi, *Fluid Phase Equilibria*, **104**, 363–374 (1995).

Chapter 5

4. "Molecular Dynamics Study of Water in Hydrogels."
   Y. Tamai, H. Tanaka, K. Nakanishi, *Molecular Simulation*, in press.

5. "Molecular Dynamics Study of Polymer–Water Interaction in Hydrogels."
   Y. Tamai, H. Tanaka, K. Nakanishi, *Macromolecules*, submitted.

Chapter 6

5. "Molecular Dynamics Study of Polymer–Water Interaction in Hydrogels."
   Y. Tamai, H. Tanaka, K. Nakanishi, *Macromolecules*, submitted.

Other publications

1. "Determination by ^{1}H and ^{13}C NMR of Stereochemical Compositions of Oligo- and Poly(methyl methacrylate)s."
   T. Konishi, Y. Tamai, M. Fujii, Y. Einaga, H. Yamakawa, *Polym. J.* **21**, 329–340 (1989).

2. "Mean-Square Radius of Gyration of Oligo- and Poly(methyl methacrylate)s in Dilute Solutions."
   Y. Tamai, T. Konishi, Y. Einaga, Y. Fujii, H. Yamakawa, *Macromolecules*, **23**, 4067–4075 (1990).

3. "Intrinsic Viscosity of Oligo- and Poly(methyl methacrylate)s."
   Y. Fujii, Y. Tamai, T. Konishi, H. Yamakawa, *Macromolecules*, **24**, 1608–1614 (1991).

Acknowledgments

The present thesis is a summary of the author's studies from 1992 to 1995 at Department of Polymer Chemistry (and Industrial Chemistry), Faculty of Engineering, Kyoto University. The author would like to express his greatest gratitude to Professor Koichiro Nakanishi and Professor Masahide Yamamoto for their valuable advice and continuous encouragement. The author deeply owes his accomplishment of the studies to the stimulating discussion and suggestions by Dr. Hideki Tanaka. The author also wishes to thank Associate Professor Tsuyoshi Nakajima, Dr. Osamu Kitao, and other members in Professor Nakanishi's Laboratory for helpful discussion and continuous encouragement. The author is grateful to Professor Hiromi Yamakawa for helpful suggestion and education at the master course of Department of Polymer Chemistry, Kyoto University.

Acknowledgment is also made for partial support by Tosoh Corporation. The author thanks Dr. Minoru Rokudai, Dr. Hiromi Yanase, and other members in the corporation for helpful discussion, various suggestions, and continuous encouragement.

The author thanks the Supercomputer Laboratory, Institute for Chemical Research, Kyoto University and Computer Center, Institute for Molecular Science for providing generous amounts of computer time.

Finally, he express his special gratitude to his wife Keiko and also to his parents Masami and Yoshiko Tamai for their continuous encouragement.

Yoshinori Tamai

Kyoto, winter 1995